3D GRID STRUCTURES FOR REALISTIC RADIATIVE TRANSFER SIMULATIONS OF DUSTY GALAXIES

Waad Saftly

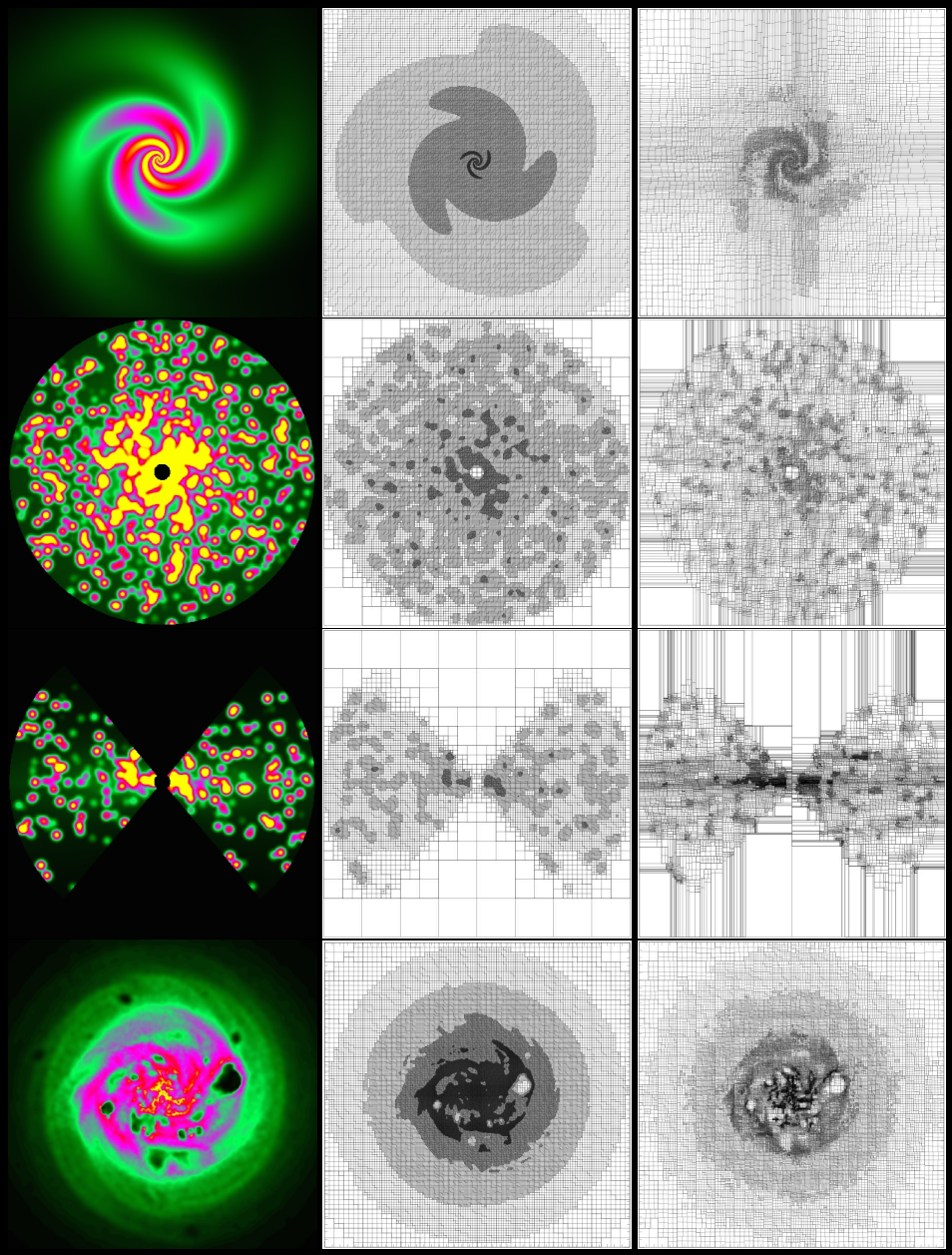

UNIVERSITEIT GENT

UNIVERSITEIT GENT

Faculty of Sciences
Department of Physics and Astronomy

3D grid structures for realistic radiative transfer simulations of dusty galaxies

Waad Saftly

A thesis submitted for the degree of Doctor of Science: Astronomy
Supervisor: Prof. Dr. Maarten Baes
Academic year 2014–2015

Supervisor:

Prof. Dr. Maarten Baes
Department of Physics and Astronomy, UGent

Members of the reading committee:

Prof. Dr. Karl Gordon
Space Telescope Science Institute, Baltimore

Prof. Dr. Tom Van Doorsselaere
Center for Mathematical Plasma Astrophysics, KU Leuven

Dr. Emmanuel Xilouris
National Observatory of Athens

Other members of the examination committee:

Prof. Dr. Dirk Ryckbosch (chair)
Department of Physics and Astronomy, UGent

Prof. Dr. Herwig Dejonghe
Department of Physics and Astronomy, UGent

Dr. Ilse De Looze
Department of Physics and Astronomy, UGent

Prof. Dr. Sven De Rijcke
Department of Physics and Astronomy, UGent

Prof. Dr. Veerle Fack
Department of Applied Mathematics, Computer Science and Statistics, UGent

I dedicate this thesis to my family
for their constant support and unconditional love.
I love you with all my heart.

Contents

Acknowledgements

Foremost, I would like to express my sincere gratitude to my supervisor Prof. Dr. Maarten Baes for his great support, warm encouragement, patience, and his excellent guidance. He gave me the opportunity to experience research in astronomy, a new and exotic field for me. I am grateful for all the conferences and workshops I could attend during my PhD, which increased my knowledge and experience. Special thanks to my SKIRT colleagues Peter Camps and Gert De Geyter, for their constructive help in the various phases of this PhD endeavour. I would also like to thank Sebastiaan Vandewoude for his first implementation of the octree bookkeeping algorithm in SKIRT, Awat Rahimi, Florent Renaud, and Javiera Guedes for sharing their hydrodynamical galaxy simulation data with us, and Aleksandra Sokolowska for providing help and support on handling the Eris simulation data. Also thanks to Gerbrand Nootens for his valuable help after computer problems, and to Inge Van der Vennet who helped me through the administrative jungle.

I am very grateful to my home university, the Al-Baath University in Homs, and the Ministry of High Education in Syria for the research grant that gave me the opportunity to come to Belgium and start a new career. Without this grant, this PhD thesis would not have been possible. Furthermore, I want to thank my internal supervisor in Syria, Dr. Khaled Al-Abdalla, for his help and support when I was in Syria. I also gratefully acknowledge the funding from the Flemish Fund for Scientific Research for the last months.

From the personal side, I really would like to express my thanks to Maarten, who provided me a lot of care and encouragement. He is the most enthusiastic, lively and smartest advisor I have ever known. Also thanks to his wife Begga for the relaxing talks we had in every time we met, she is a very kind and unforgettable person. Many thanks to my office mates Steven, Gianfranco, and Flor for the nice conversations and comfortable atmosphere. Furthermore, I would like to thank all the friends and colleagues in the Physics and Astronomy department of Ghent University and beyond for the nice evenings out, the birthdays, the delicious Belgian desserts, and the many special events.

Finally, I would like to take the opportunity to thank my family, who supported me not only now, but throughout my academic career and my entire life. Thanks to my father and mother for their comfortable talks; I really appreciate their patience for not seeing me for four years. Thanks to my sister Zinab and my two brothers, Mohammad and Meelad, for their relaxing, funny and nice conversations that made me forget my stressful moments, and for all the motivation they gave me with every phone call. Due to the situation in Syria, the past four years have not always been easy, neither for them nor for me, and I hope the future will be brighter soon.

1 Introduction

1.1.1 The importance of interstellar dust

Galaxies are generally considered as the building blocks of the Universe, and contain billions of stars. Figure 1.1 shows the Hubble classification diagram, the classical scheme to subdivide galaxies in different classes. The galaxies on the left-hand side are so-called early-type galaxies, and they are subdivided as elliptical galaxies and lenticular galaxies. The main difference between both classes is that lenticular galaxies contain a disc (without spiral arms), whereas elliptical galaxies essentially consist of a smooth spheroidal distribution of stars. In general, early-type galaxies contain relatively old stellar populations and have little to no ongoing star formation. The galaxies on the right-hand side of the diagram are the so-called late-type galaxies, and they are subdivided in two parallel branches, depending on whether they have a central bar or not. Morphologically, spiral galaxies consist of a flat disk, where new stars are actively being formed in a spiral structure, and a central spheroidal component of older stars known as the bulge. Depending on their detailed morphology, bulges are often subdivided as classical bulges (somewhat similar to an elliptical galaxy) or pseudo-bulges (more similar to a disc structure).

Galaxies are more than just a collection of stars only: the space between the stars is not empty, but contains a varied multi-component mixture of atoms, molecules, ions and solid particles. This multi-phase mixture is known as the interstellar medium (ISM). Most of the interstellar medium is in the gaseous phase and only a minor fraction consists of small solid particles, known as interstellar dust. The dust-to-gas mass ratio in galaxies varies between about 10^{-3} to 10^{-2}, although some more extreme values are possible (Rémy-Ruyer et al. 2014). The dust-to-stellar mass ratio covers a larger range and varies with Hubble type: for early-type galaxies typical values are 10^{-6} to 10^{-4}, whereas for late-type spirals it rises up to 10^{-2} (Cortese et al. 2012).

Cosmic dust was initially considered as a nuisance to astronomers, as it blocks the light emitted by objects they want to observe. Nowadays, cosmic dust is considered as an interesting and dynamic ingredient in the interstellar medium. It plays a very important role in various astrophysical processes in the Universe.

A prime example of the importance of cosmic dust is its role in the process of star formation. Dust grains catalyse the formation of molecular hydrogen which is the primary material from which new stars are formed. In the diffuse interstellar medium, the probability that two hydrogen atoms combine to form a H_2 molecule is rather low. Surface processes on the surface of dust grains are much more efficient; not only for

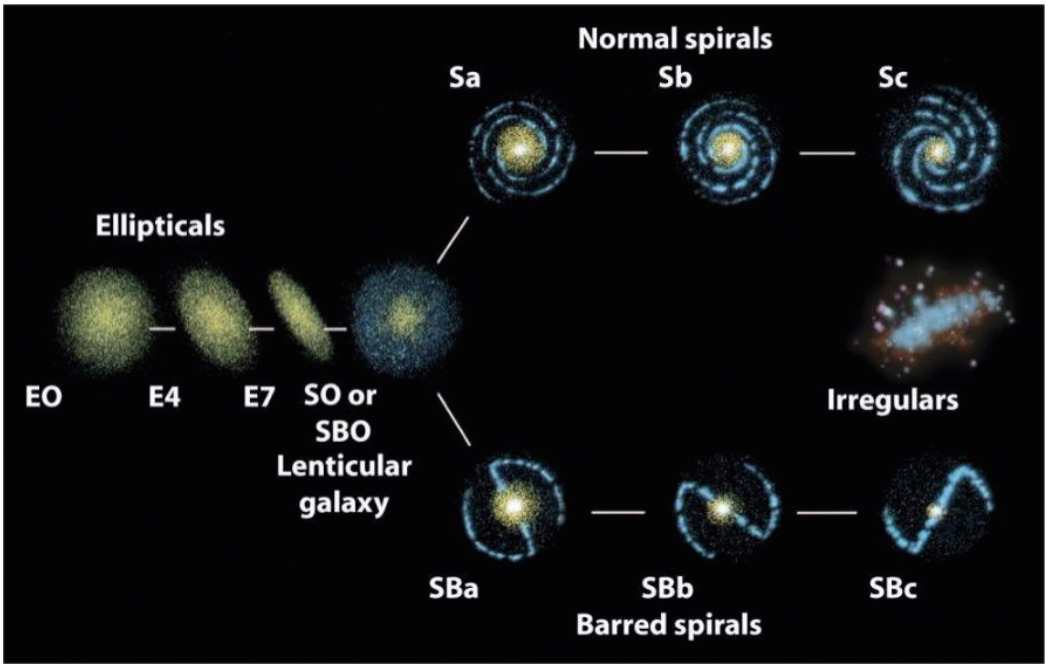

Figure 1.1: An illustration of Hubble's galaxy classification diagram. On the left we have early-type galaxies (elliptical and lenticular galaxies), on the right the two branches of late-type galaxies (normal and barred spiral galaxies). Galaxies that do not fit this scheme are classified as irregular galaxies. © Robin Shelton, University of Georgia.

the formation of H_2, but for other molecules as well (Hollenbach and Salpeter 1971; Gerner 2014; Garrod et al. 2008). Moreover, dust grains in molecular clouds shield the molecules from energetic radiation, which helps them to cool down and condense. It hence helps to create the suitable conditions for the clouds to collapse under their own gravity and start star formation. As young stars remain embedded in their birth clouds for several Myr, thermal emission by dust grains can be used to trace star formation in galaxies (Kennicutt et al. 2009; Peeters et al. 2004; Calzetti 2008; Hao et al. 2011; Li et al. 2010).

Perhaps even more fundamental is the role of dust grains in the formation of planetary systems, including our own Solar System. When molecular clouds collapse to form a protostar, the material around the protostar forms a circumstellar or protoplanetary disc. In this disc, dust grains and molecules collide and stick together to eventually form kilometre-sized bodies, called planetesimals. Hundreds of these planetesimals are forming at the same time, and after millions of years, countless encounters between these planetesimals have cleared out much of the disk's debris and have built up much larger systems: planets (e.g. Blum et al. 2000; Dominik et al. 2007; Bouwman et al. 2008).

In this thesis, we will focus on the role of dust in processing radiation. One of the most obvious characteristic of interstellar dust is that it is extremely effective in attenuat-

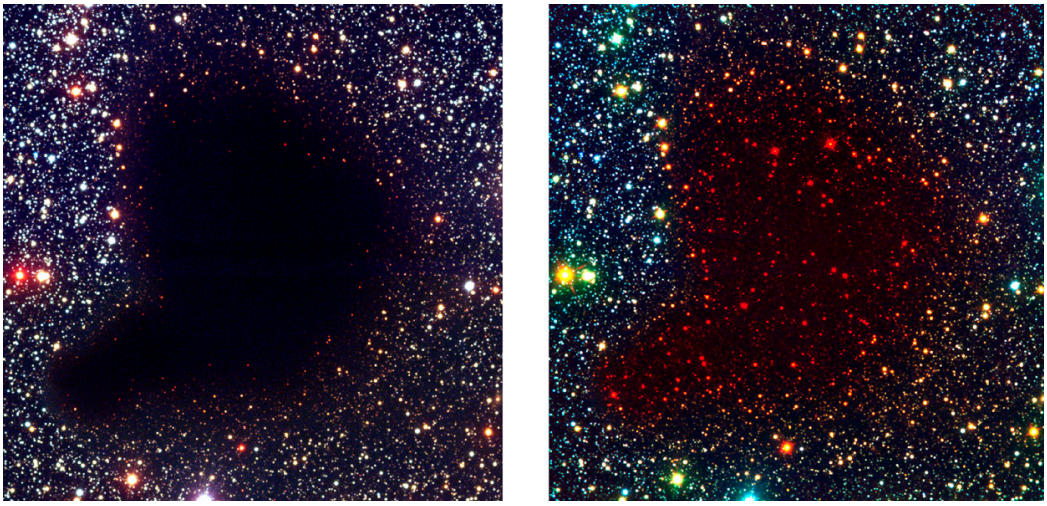

Figure 1.2: A composite image of optical and near-infrared images of the molecular cloud Barnard 68. In the optical image (left panel), stars behind the cloud are hidden due to the effects of attenuation by dust. In the near-infrared image (right panel), the efficiency of dust attenuation is strongly reduced and the stars appear again. © European Southern Observatory.

ing stellar light. The attenuation is strongest at UV and blue optical wavelengths and gradually decreases with increasing wavelengths. In the near-infrared K-band, dust extinction is 10 times less strong than in the optical B-band. Figure 1.2 shows a striking example of the attenuating effects of interstellar dust. The left panel shows an optical image of Barnard 68, a dark cloud in our Milky Way. The dust in this cloud blocks all the light of the stars behind it. The stars reappear in the right-hand panel, which shows a near-infrared image of the same region. Similarly, clear signatures of dust attenuation can be noted on galaxy-wide scales (Figure 1.3).

It is estimated that about 50% of all the radiation emitted by stars in the Universe is absorbed by interstellar dust (Lagache et al. 2005). This means that dust can significantly bias our view on systems like star forming regions, active galactic nuclei or galaxies as a whole. If we want to correctly interpret the observed images of such systems, and convert them to intrinsic characteristics, we need to take into account the obscuring effects of cosmic dust. On the other hand, the energy absorbed at UV and optical wavelength is converted to internal heat, and subsequently re-emitted as thermal radiation by dust at infrared wavelengths. In fact, in the wavelength regime between about 5 and 1000 μm, thermal emission by dust is by far the largest contributor. The combination of information in the UV/optical regime, where attenuation by dust is important, and information in the infrared regime, where emission by dust is the dominant emission process, gives the strongest constraints on the amount, spatial distribution and nature of cosmic dust.

The only way to incorporate the effects of emission, absorption, scattering and thermal

Figure 1.3: Optical images of the three galaxies with clear signatures of dust attenuation. NGC 891 (left panel) is a spiral galaxy seen edge-on, and the dust attenuation is clearly visible as a dust lane. The Sombrero Galaxy M104 (middle panel) is an early-type spiral galaxy characterised by a huge stellar bulge and a series of concentric dust rings. Finally, NGC 7049 (right panel) is a lenticular galaxy with a prominent rope-like dust ring that stands out against the bright background of starlight behind it. © Hubble Space Telescope.

re-emission in a correct way is by solving the continuum radiative transfer equation, in a realistic geometrical framework and taking into account all relevant physical processes.

1.1.2 The dust radiative transfer equation

In an empty space, radiation emitted at a given location of the Universe could in principle travel unhindered to our telescope if it is emitted in the correct direction. In a space filled with matter, such as the interstellar medium in galaxies, radiation is affected by different processes, such as absorption, re-emission, and scattering. These interactions between radiation and matter are described mathematically by the radiative transfer equation. The fundamental quantity that describes the radiation field is called the specific intensity; more specifically, $I(\boldsymbol{x}, \boldsymbol{k}, \lambda, t)$ denotes the intensity of the radiation field with wavelength λ at the location $\boldsymbol{x}$ and the time t, propagating into the direction $\boldsymbol{k}$. The radiative transfer equation describes how this quantity changes when it travels a distance ds into the direction $\boldsymbol{k}$. The general form of the time-dependent radiative transfer equation is (Chandrasekhar 1960)

$$\left[\frac{1}{c}\frac{\partial}{\partial t} + \frac{\partial}{\partial s}\right] I(\boldsymbol{x}, \boldsymbol{k}, \lambda, t) = -\kappa(\boldsymbol{x}, \lambda, t)\, \rho(\boldsymbol{x}, t)\, I(\boldsymbol{x}, \boldsymbol{k}, \lambda, t) + j(\boldsymbol{x}, \boldsymbol{k}, \lambda, t). \tag{1.1}$$

In this equation, $j(\boldsymbol{x}, \boldsymbol{k}, \lambda, t)$ is the so-called emissivity term, which accounts for the radiation processes that add to the intensity of the radiation field (radiation of wavelength λ, added to the radiation field at the time t, at the position $\boldsymbol{x}$ and into the direc-

tion $\boldsymbol{k}$). The first term on the right-hand side in the radiative transfer equation accounts for the sinks in the radiation process, i.e. it takes into account the physical processes that remove energy from the radiation field. In this term, $\rho(\boldsymbol{x}, t)$ is the mass density of matter, and $\kappa(\boldsymbol{x}, \lambda, t)$ is the so-called opacity coefficient.

The complexity of the radiative transfer equation depends on the nature of the source and sinks terms, which depend on the specific physical processes that are taken into account. In this thesis, we will focus on dust radiative transfer, i.e., the transfer of continuum radiation through a dusty interstellar medium. Moreover, we will only consider time-independent radiative transfer, which is usually appropriate in most applications of dust radiative transfer[1]. In galaxies, for example, the time scale at which the light travels through the system is much shorter than the time scale at which the system itself evolves. The assumption of time independence immediately simplifies the transfer equation to

$$\frac{\mathrm{d}I}{\mathrm{d}s}(\boldsymbol{x}, \boldsymbol{k}, \lambda) = -\kappa(\boldsymbol{x}, \lambda)\, \rho(\boldsymbol{x})\, I(\boldsymbol{x}, \boldsymbol{k}, \lambda) + j(\boldsymbol{x}, \boldsymbol{k}, \lambda). \tag{1.2}$$

Now it still remains to determine the specific forms of the sink and source terms. The most physical processes to consider in dust radiative transfer are stellar emission, absorption by dust, scattering off dust grains, and thermal re-emission by dust of the absorbed energy. With these physical processes taken into account, and assuming that the physical properties of the dust grains do not change from location to location, the dust radiative transfer equation becomes (Steinacker et al. 2013)

$$\begin{aligned}\frac{\mathrm{d}I}{\mathrm{d}s}(\boldsymbol{x}, \boldsymbol{k}, \lambda) = &-\kappa^{\mathrm{abs}}(\lambda)\, \rho(\boldsymbol{x})\, I(\boldsymbol{x}, \boldsymbol{k}, \lambda) - \kappa^{\mathrm{sca}}(\lambda)\, \rho(\boldsymbol{x})\, I(\boldsymbol{x}, \boldsymbol{k}, \lambda) \\ &+ j^*(\boldsymbol{x}, \lambda) + \kappa^{\mathrm{sca}}(\lambda)\, \rho(\boldsymbol{x}) \int_{4\pi} I(\boldsymbol{x}, \boldsymbol{k}', \lambda)\, \Phi(\boldsymbol{k}, \boldsymbol{k}', \lambda)\, \mathrm{d}\Omega' + j^{\mathrm{d}}\Big(J(\boldsymbol{x}, \lambda)\Big). \end{aligned} \tag{1.3}$$

The first two terms of the right-hand side of this equation represent the sinks terms. The first term is the loss of photons due to absorption, i.e., the process by which the radiative energy is converted to internal energy of the dust grain. The second term is the loss due to scattering. Scattering does not convert the radiation to internal energy, but just changes the propagation direction of the radiation. The absorption and scattering coefficients $\kappa^{\mathrm{abs}}(\lambda)$ and $\kappa^{\mathrm{sca}}(\lambda)$ can in principle be calculated or measured exactly if the chemical composition, sizes and shapes of the dust grains are known.

The last three terms are the source terms, and they account for the addition of energy from emission sources to the radiation field. The first of these three is the primary source term, i.e. the emission j^* that arises from primary sources. The primary sources

[1] For an exception, see e.g., Harries (2011).

are typically stars, but it can also be an active galactic nucleus or line emission from gas. The primary emissivity is assumed to be isotropic, but this condition is not always satisfied and can easily be accommodated in the solution methods for the radiative transfer equation (Niccolini et al. 2003; Stalevski et al. 2012).

The fourth term on the right-hand side of equation (1.3) is the source term due to scattering. As we discussed before, the physical process of scattering removes energy from the radiation field and scatters it into another direction. This means that scattering results in both a sink and a source term. The scattering source term consists of the joint contribution of the radiative energy scattered from the original propagation direction $\boldsymbol{k}'$ into the new direction $\boldsymbol{k}$. The function $\Phi(\boldsymbol{k}, \boldsymbol{k}', \lambda)$ in this term is the scattering phase function, which represents the probability that a photon that is scattered from a direction $\boldsymbol{k}'$ has $\boldsymbol{k}$ as its new propagation direction. It is usually a function only of the cosine of the scattering angle, $\cos\Theta = \boldsymbol{k} \cdot \boldsymbol{k}'$. The most widely used phase function that describes anisotropic coherent scattering is the Henyey-Greenstein phase function,

$$\Phi_\lambda(\cos\Theta) = \frac{1}{4\pi} \frac{1 - g_\lambda^2}{(1 + g_\lambda^2 - 2g_\lambda \cos\Theta)^{3/2}}, \tag{1.4}$$

where the parameter g_λ is the so-called anisotropy parameter,

$$g_\lambda = \int \Phi_\lambda(\cos\Theta) \cos\Theta \, \mathrm{d}\Omega. \tag{1.5}$$

The asymmetry parameter g_λ can have values between -1 and 1; special cases are $g_\lambda = 0$ (isotropic scattering), $g_\lambda = 1$ (completely forward scattering), and $g_\lambda = -1$ (pure backward scattering). In the dusty ISM, the anisotropy parameters is generally positive at optical wavelengths, indicating that scattering is more efficient in the forward direction. Figure 1.4 shows the Henyey-Greenstein function for different values of g_λ.

Finally, the last term in equation (1.3) represents the thermal re-emission by dust grains. The thermal emissivity typically depends in a complex and nonlinear way on the mean intensity of the radiation field,

$$J(\boldsymbol{x}, \lambda) = \frac{1}{4\pi} \int_{4\pi} I(\boldsymbol{x}, \boldsymbol{k}, \lambda) \, \mathrm{d}\Omega. \tag{1.6}$$

For a hypothetical simple dust mixture consisting of dust grains of a single composition, size and shape, the emissivity can be written as a modified blackbody,

$$j^{\mathrm{d}}(\boldsymbol{x}, \lambda) = \kappa^{\mathrm{abs}}(\lambda) \, \rho(\boldsymbol{x}) \, B\Big(T_{\mathrm{eq}}(\boldsymbol{x}), \lambda\Big) \tag{1.7}$$

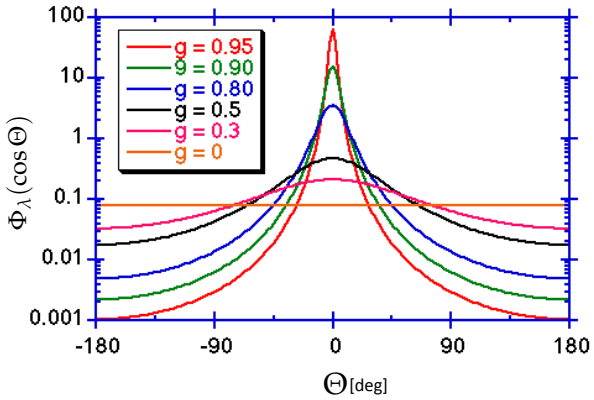

Figure 1.4: The Henyey-Greenstein scattering phase function as a function of the scattering angle Θ for different values of the asymmetry parameter g_λ. © Steven L. Jacques, Oregon Medical Laser Center.

with $B(T, \lambda)$ the Planck function, and $T_{\rm eq}(\boldsymbol{x})$ is the equilibrium temperature of the dust grains at position $\boldsymbol{x}$, defined implicitly through the energy balance equation

$$\int_0^\infty \kappa^{\rm abs}(\lambda)\, J(\boldsymbol{x}, \lambda)\, {\rm d}\lambda = \int_0^\infty \kappa^{\rm abs}(\lambda)\, B\Big(T_{\rm eq}(\boldsymbol{x}), \lambda\Big)\, {\rm d}\lambda \tag{1.8}$$

The use of local thermal equilibrium (LTE) is only justified for large dust grains, which will approximately reach a single equilibrium temperature. In a real dust mixture, we can find different types of dust grains with different sizes and different chemical compositions. Particularly important is the case when the dust medium contains very small dust grains like polycyclic aromatic hydrocarbons (PAHs). The temperature of these small dust grains increases instantaneously when they absorb a single stellar photon and will reach values much higher than the nominal equilibrium temperature. After the absorption event, they will gradually cool down. Therefore they are better described by a temperature distribution function rather than a simple equilibrium temperature. The calculation of NLTE dust emission is much more difficult and computationally more expensive. Several methods and numerical codes have been developed to calculate the NLTE heating of dust grains (Guhathakurta and Draine 1989; Draine and Li 2001; Compiègne et al. 2011).

1.1.3 Dust radiative transfer on galaxy-wide scales

Cosmic dust is found throughout the Universe, from the Solar System (Gustafson 1994; Küppers et al. 2005; Hoppe et al. 2010) to the most pristine galaxies in the high-redshift Universe (Dwek et al. 2007; Cox et al. 2011). As a result, 3D dust radiative transfer has been applied to model a large variety of objects and structures. The most advanced

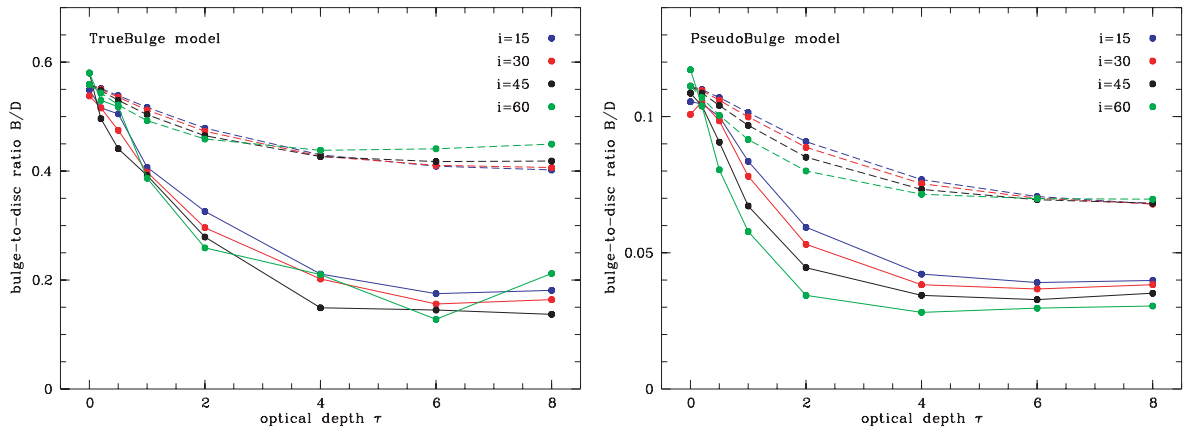

Figure 1.5: Dependence of the bulge-to-disc ratio on the V-band optical depth. The left panel represents models with a real bulge, whereas the right panel corresponds to models with a so-called pseudo-bulge. The solid lines in both panels represent the apparent bulge-to-disc ratio as derived from a bulge/disc decomposition of the dust-affected images. The dashed lines represent the actual bulge-to-disc ratio. Figure taken from Gadotti et al. (2010)

applications of 3D dust radiative transfer include molecular clouds (Steinacker et al. 2005; Ysard et al. 2012), circumstellar discs (Min et al. 2009; Dullemond and Monnier 2010; Whitney et al. 2013), active galactic nuclei (Schartmann et al. 2008, 2014; Stalevski et al. 2012), and galaxies as a whole (Bianchi 2008; De Looze et al. 2014).

In this thesis, we will focus on the application of 3D dust radiative transfer on galaxy-wide scales, a field that has experienced a significant boost over the past few years. The dust radiative transfer applications can be subdivided in three broad categories.

The first application of dust radiative transfer on galaxy-wide scales aims at systematically investigating the effects of dust on the observed properties of galaxies using toy models. Through the effects of absorption, scattering and thermal emission, dust influences the observed, apparent photometric parameters of galaxies (apparent scale-lengths, surface brightnesses, luminosities, axial ratios, etc.) and makes it a challenge to recover the unaffected parameters. Therefore, 3D radiative transfer calculations are important to understand the complex interplay between starlight and dust grains in galaxies. Many investigations were done to study the effects of dust attenuation on the observed structural properties of stellar bulges and discs (Byun et al. 1994; Misiriotis et al. 2000, 2001; Tuffs et al. 2004; Pierini et al. 2004; Gadotti et al. 2010; Pastrav et al. 2013a,b). The general results of these studies is that dust can significantly affect both the scale-length and the surface brightness of the stellar bulges and discs.

An example of one such study is the work by Gadotti et al. (2010). They used radiative transfer simulations to create mock images of dusty galaxies, and subsequently applied 2D bulge/disc decomposition techniques upon this set of models. Rather surprisingly,

the effects of dust on the structural parameters of bulges and discs obtained from 2D bulge/disc decomposition cannot be simply evaluated by putting together the effects of dust on the properties of bulges and discs treated separately. Bulge parameters were found to be more affected than disc parameters, and, combined, they lead to a strong underestimation of the bulge-to-disc ratio up to a factor of two in the V band, even at relatively low galaxy inclinations and dust opacities (Figure 1.5).

In a similar way, the effects of dust on the observed stellar and gas kinematics of galaxies have been investigated (Baes and Dejonghe 2000, 2001a, 2002; Matthews and Wood 2001; Baes et al. 2003). The effects of absorption and scattering on the mean velocity and the velocity dispersion are generally modest. However, in certain configurations, the observed kinematics of elliptical galaxies can be affected significantly, in the way that the presence of a dark matter halo is mimicked.

A second major application of 3D dust radiative transfer on galaxy-wide scale is the so-called post-processing of simulated galaxies. In the last decade there has been a major improvement in the realism of hydrodynamical simulations of galaxy formation and evolution. In particular, only recently, we have started to see realistic spiral galaxies formed self-consistently in a cosmological context (Scannapieco et al. 2012; Bournaud et al. 2007, 2009; Governato et al. 2009; Agertz et al. 2011; Guedes et al. 2011; Wada et al. 2011; Stinson et al. 2013; Marinacci et al. 2014; Inoue and Saitoh 2014; Murante et al. 2015). The results of these hydrodynamical simulations, based on either grid-based techniques or using smoothed particle hydrodynamics, typically result in complex 3D geometrical distributions for gas, stars and dark matter. The goal of such simulations is to reproduce galaxies that have properties similar to observed galaxies. In order to compare the simulated galaxies to the real observed Universe, the effects of dust attenuation need to be taken into account. Due to the complex geometry of these simulations, 3D dust radiative transfer codes play a crucial role in this comparison process (Jonsson 2006; Jonsson et al. 2010; Hayward et al. 2011, 2012, 2013, 2014; Domínguez-Tenreiro et al. 2014; Schaye et al. 2015; Natale et al. 2015).

Finally, 3D radiative transfer can be applied to model the distribution of stars and dust in individual observed galaxies, a process also called inverse radiative transfer. It is essentially a complex optimisation problem: first we define a radiative transfer model with a number of free parameters, and subsequently we search the parameter space using an optimisation algorithm to find the parameter values that minimise the differences between the model and the observations (usually images and/or spectral energy distributions). The main challenge is that every point in the parameter space requires a complete radiative transfer simulation and a comparison between the simulated images and the actual data. Because the attenuation effects are so clearly shown in edge-on spiral galaxies, they have been the primary target for inverse radia-

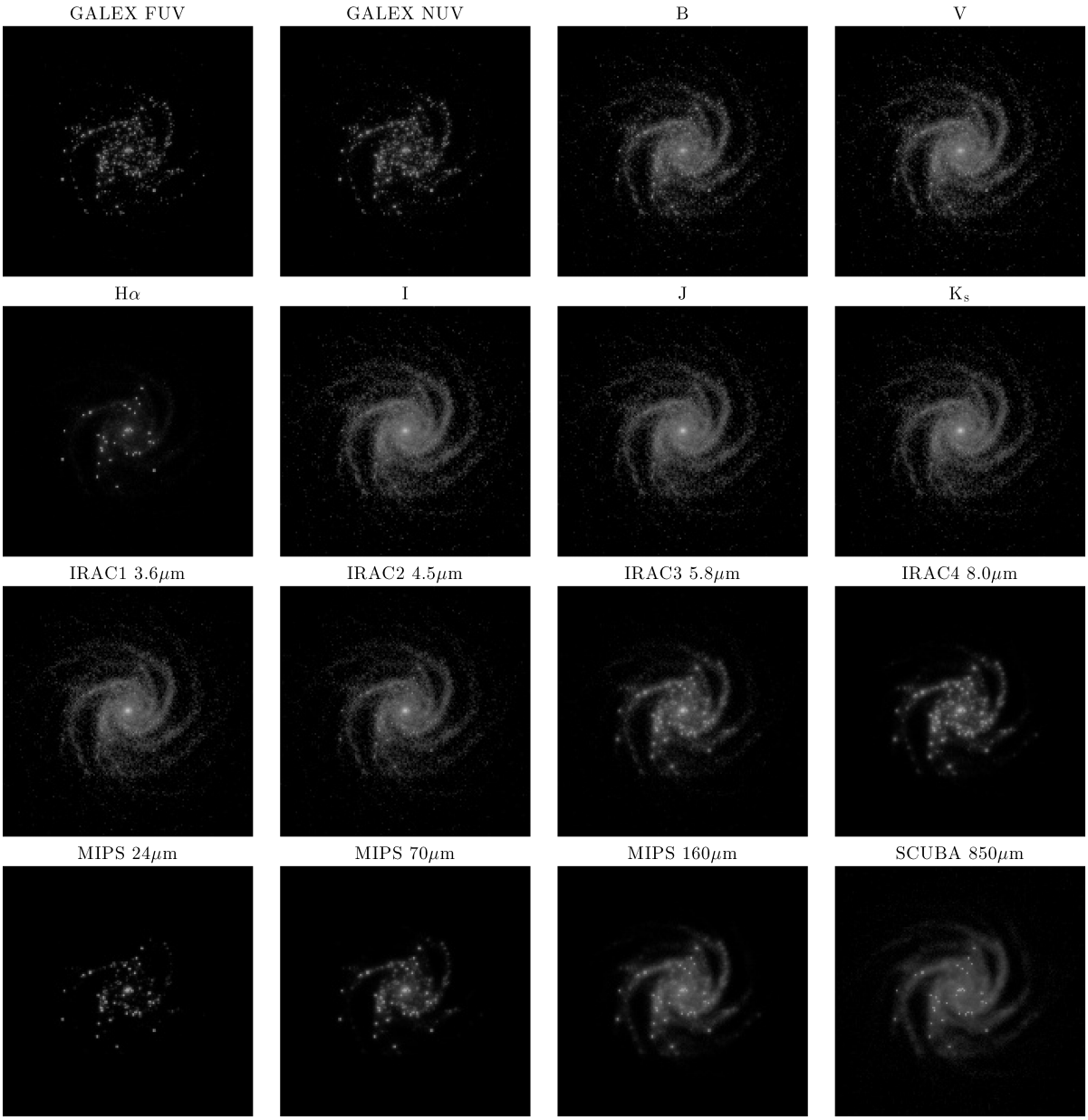

Figure 1.6: A series of mock images created by post-processing a snapshot from a hydrodynamical simulation of an Sbc type spiral galaxy with the 3D dust radiative transfer code SUNRISE. The multi-wavelength properties of this and similar post-processed simulated galaxies agree well with the average multi-wavelength properties of nearby galaxies from the SINGS survey. Figure taken from Jonsson et al. (2010).

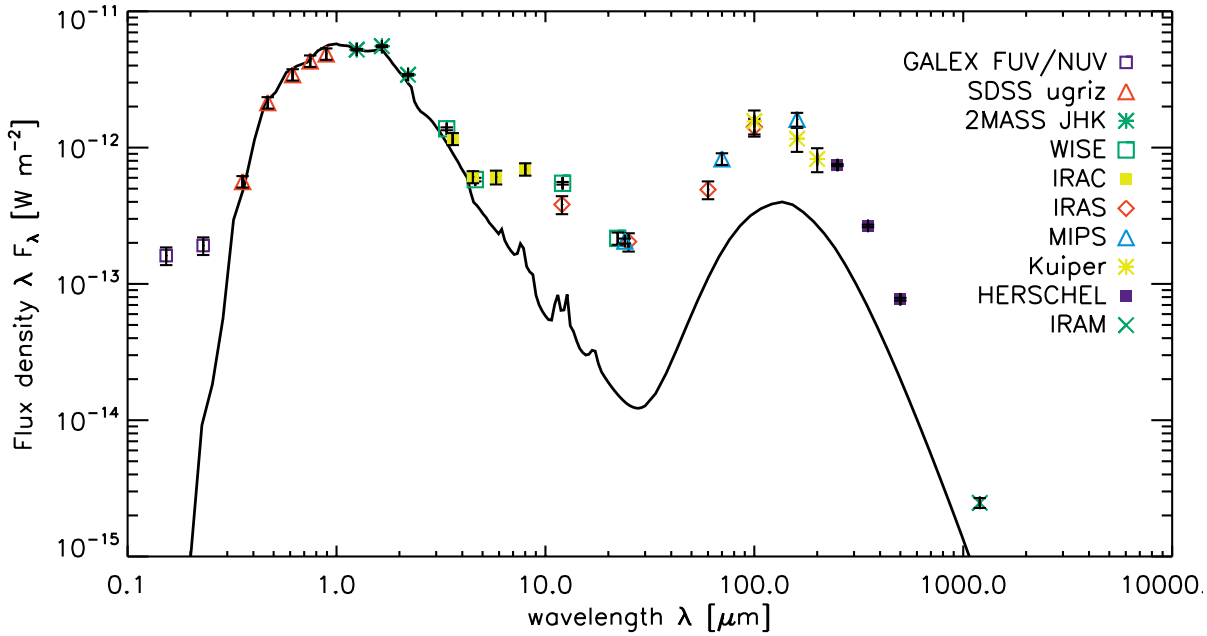

Figure 1.7: The dust energy balance problem in the edge-on spiral galaxy NGC 4565. The solid line represents the predicted SED from a radiative transfer model that can successfully explain the observed images at optical and NIR wavelengths. The model clearly fails to reproduce the observed fluxes at FIR/submm wavelengths (coloured points). Figure taken from de Looze et al. (2012).

tive transfer modelling. The stellar and dust distribution of about two dozen edge-on spiral galaxies have been determined in this way (e.g., Xilouris et al. 1997, 1999; Alton et al. 2004; Bianchi 2007; Baes et al. 2010; MacLachlan et al. 2011; Schechtman-Rook et al. 2012; De Looze et al. 2012; de Looze et al. 2012; De Geyter et al. 2013, 2014).

A fascinating result in this context is the so-called dust energy balance problem. When the distribution and characteristics of the stars and the dust in an edge-on galaxy have been determined through inverse radiative transfer fitting to optical/NIR images, one can calculate exactly how much energy is absorbed at every wavelength and at every location in the galaxy. Subsequently one can predict the corresponding thermal emission in the far-infrared and submm domain, and compare the resulting fluxes and images to the actual observations at these wavelengths. Several studies that have compared the FIR/submm emission of the radiative transfer models that successfully explain the optical extinction in edge-on spiral galaxies generally underestimate the observed FIR/submm fluxes by a factor of about three (Popescu et al. 2000; Misiriotis et al. 2001; Alton et al. 2004; Dasyra et al. 2005; Baes et al. 2010; de Looze et al. 2012; De Looze et al. 2012). Figure 1.7 shows a clear example of this dust energy balance problem in the edge-on spiral galaxy NGC 4565: the difference between the modelled SED (solid black line), and the observed fluxes (coloured points) at FIR/submm wave-

lengths is obvious.

Several scenarios have been proposed to explain this discrepancy. A first explanation is that the far-infrared dust emissivity, derived from dust models fine-tuned to the diffuse dust emission in the Milky Way, is actually underestimated by a factor two to three (Alton et al. 2000, 2004; Dasyra et al. 2005). Another suggested explanation is that a sizeable fraction of the FIR/submm emission arises from additional dust that has a negligible extinction on the bulk of the starlight (e.g., Popescu et al. 2000; Bianchi 2008; Baes et al. 2010; De Looze et al. 2012). A major problem distinguishing between these scenarios is that the number of edge-on galaxies for which such detailed studies have been done so far is limited, and that most studies were done using different assumptions, models and codes. Also from the theoretical point of view, there has been little progress, partly due to the fact that only recently, we have seen the emergence of realistic hydrodynamical simulations of spiral galaxies.

1.2.1 Solving the dust radiative transfer equation

The radiative transfer equation (1.3) is a complex partial integro-differential equation that is impossible to solve using standard solution methods. It is a nonlinear and non-local problem in no less than six independent dimensions.

One way to deal with this complexity is to simplify the problem by just considering highly symmetric configurations. In particular, many different solution methods have been developed for the radiative transfer problem in spherical and plane-parallel geometry (e.g., Henyey 1937; Chandrasekhar 1960; Flannery et al. 1980; Bruzual et al. 1988). Another attempt to circumvent the complexity is to use an approximation for the scattering term that is responsible for the integro-differential character. Also here different scenarios have been proposed, ranging from simply neglecting scattering to ad-hoc recipes (Code 1973; Natta and Panagia 1984). However, these recipes are unable to capture the complex and sometimes counterintuitive effects that can only be obtained by a proper inclusion of scattering (Baes and Dejonghe 2001c).

Fortunately, since radiative transfer is a process that is so common in all fields of astrophysics (and many other sciences), different specialised techniques have been developed. Each one of these methods has its advantages and disadvantages, which we attempt to summarise here.

The finite-difference method. This method applies the traditional recipes that are commonly used for sets of partial differential equations. The space in each dimension is discretised to a finite grid, differentials are converted to differences and integrals are converted to sums, all on the grid points. The result is that the RTE is converted to a system of linear equations. In one-dimensional radiative transfer problems, this method is simple and fast (Milkey et al. 1975; Bruzual et al. 1988; Baes and Dejonghe 2001b). Moving to two or three spatial dimensions, the method quickly becomes very intricate, and the linear equations extremely difficult to solve even with powerful solvers. There have been a few modest efforts to build 3D dust radiative transfer codes based on this principle (Stenholm et al. 1991; Steinacker et al. 2002).

The moment method. The basis idea of the moment method is to expand the specific intensity as a series of spherical harmonics. This technique is one of the most popular and fastest techniques to solve the radiative transfer equation in plane-parallel or spherical symmetry (Flannery et al. 1980; Roberge 1983; di Bartolomeo et al. 1995; Baes and Dejonghe 2001b). It has several advantages in terms of solu-

tion accuracy and storage requirements, but can exhibit nonphysical oscillations. As far as we are aware, there are no 3D dust radiative transfer codes based on the moment method.

Ray-tracing. Ray-tracing is a very popular technique in the computer graphics community, where it is the standard technique for 3D rendering purposes. In the field of radiative transfer, ray-tracing is the common name for a range of techniques that follow the change in specific intensity along a number of predetermined straight lines (rays) through the computational domain. Depending on whether information is propagated through the entire domain or just to the next cells, one makes the distinction between long and short characteristics. Ray-tracing solvers have the advantage that the numerical error can be controlled precisely. A drawback of the technique is that complexity increases substantially when moving from 1D and 2D to 3D. This complexity lies in the placement of the rays, and the memory requirements that can be substantial. Today, there are a few pure ray-tracing dust radiative transfer codes available that can handle general 3D geometries (Steinacker et al. 2006; Natale et al. 2014).

The Monte Carlo method. The Monte Carlo method is a probabilistic method that simulates the process of radiative transfer rather than actually solving the radiative transfer equation. In its modern form, one could consider Monte Carlo radiative transfer as a special (and advanced) kind of ray-tracing (Steinacker et al. 2013). It will be discussed in more detail in Section 1.2.2.

1.2.2 The Monte Carlo approach

Monte Carlo is a general computational technique that is used widely in many different fields, including numerical mathematics, physical sciences, finance, and medicine. It is a stochastic technique that heavily builds on random numbers drawn from the appropriate distribution functions. It is by far the most widely adopted method for 3D dust radiative transfer: in the recent review by Steinacker et al. (2013), 27 of the 30 dust radiative transfer codes listed were Monte Carlo codes.

In Monte Carlo radiative transfer, the radiation field is treated as a flow of a finite number of photon packages. The path of every single photon package is followed throughout the dusty medium, which is partitioned in a large number of small cells. The characteristics of each photon package, such as its luminosity, propagation direction, and last interaction site, are updated when it undergoes various events such as emission, absorption and scattering. These events are determined by random numbers generated from appropriate probability distributions. In the most simple applications of Monte Carlo radiative transfer, the lifecycle of a photon package ends when it leaves

the dusty system. After all photon packages have left the system, a number of observable diagnostics are constructed by classifying the photon packages that left the system according to their characteristics. It is not necessary to go into all the details of the Monte Carlo method for the sake of this Thesis. Interested readers can find the Monte Carlo method for radiative transfer described in detail in many papers (e.g., Witt 1977; Bianchi et al. 1996; Niccolini et al. 2003; Whitney 2011; Steinacker et al. 2013).

From a computational point of view, the most important part of a Monte Carlo simulation is the calculation of the paths of every individual photon package through the dusty medium. A typical Monte Carlo simulation follows millions of individual photon packages, and for each of them several paths need to be calculated (every time a photon package is emitted or scattered, a new path needs to be calculated). The calculation of these paths is typically done on a grid on which the dusty medium is discretised. Each of the cells in this grid is typically characterised by a constant dust density, radiation field, etc. Their size sets the effective resolution of the simulation.

The Monte Carlo approach has a number of advantages compared to the other listed techniques that explain its popularity. Probably the most important one is that this technique is quite easy to implement and that it is intrinsically 3D in nature. Contrary to virtually all other dust radiative transfer techniques, there is no big leap to take when going from 1D to 3D simulations. A second advantage is the flexibility of the method: physical processes like polarisation (Code and Whitney 1995; Goosmann and Gaskell 2007) or kinematical information (Matthews and Wood 2001; Baes and Dejonghe 2002; Baes et al. 2003) are relatively easily incorporated in Monte Carlo codes. In this context it is interesting to note that similar Monte Carlo techniques are applied to other transport problems, such as neutrino transport (Abdikamalov et al. 2012), UV ionizing radiation transport (Ciardi et al. 2001; Wood et al. 2004) and Lyα radiation transport (Verhamme et al. 2006; Tasitsiomi 2006; Laursen et al. 2009). Finally, the method is also fairly economic in memory consumption, compared to, for example, ray-tracing or finite difference techniques.

The most important disadvantage of the Monte Carlo method is the presence of Poisson noise and the corresponding slow convergence (the Poisson noise goes as $N^{-1/2}$ with N the number of photon packages). The presence of Poisson noise is inherently linked to the use of random numbers. The simplest way to overcome this problem is to increase the number of photon packages in the simulation, but this is often not a viable solution.

An alternative solution is to include a number of optimisation or acceleration techniques that can make the Monte Carlo method more efficient. The basis of all acceleration methods is to assign a weight to each photon package, or equivalently, to vary

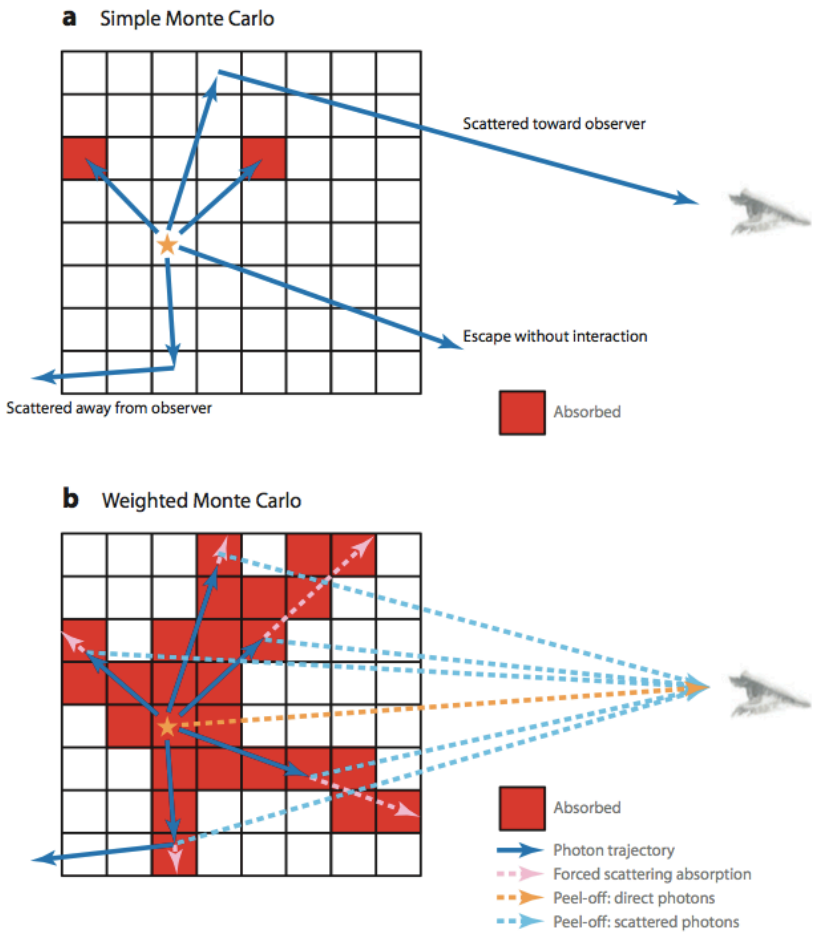

Figure 1.8: A graphical illustration of simple and weighted Monte Carlo simulations. This example includes five photon packages resulting in one scattered photon reaching the observer and two absorption events for simple Monte Carlo radiative transfer. This same set of five photon packages produces five scattered photons toward the observer and 28 absorption events for a modified Monte Carlo routine where forced scattering, continuous absorption and peel-off are incorporated. The improvement in computational efficiency of weighted Monte Carlo is seen clearly. Figure taken from Steinacker et al. (2013).

the luminosity of each package during its journey through the dusty system. Several acceleration methods use the idea of biasing, a powerful Poisson noise suppressing technique (it is known as importance sampling in Monte Carlo numerical integration). Many acceleration techniques have been described in the literature, some of them well established and validated, others still experimental (see Figure 1.8). In the first category we can place techniques as biased emission (Yusef-Zadeh et al. 1984; Juvela 2005), forced scattering (Cashwell and Everett 1959; Mattila 1970; Witt 1977), peel-off (Yusef-Zadeh et al. 1984) and continuous absorption (Lucy 1999; Niccolini et al. 2003). Among the more experimental techniques are smart detectors (Baes 2008), polychromatism (Juvela 2005; Jonsson 2006) and continuous scattering (Baes and Camps 2015).

Figure 1.8 sketches the difference between the basic Monte Carlo routine, and the weighted Monte Carlo method that uses forced scattering, continuous absorption and peel-off (standard techniques currently used in virtually all 3D Monte Carlo dust radiative transfer codes). In the weighted Monte Carlo framework, the life cycle of a monochromatic photon package can be considered as a loop of every time the same steps:

1. First, the initial position is generated randomly from the stellar emissivity distribution function and its propagation direction is randomly generated from the unit sphere. The initial luminosity of the photon package is simply the total luminosity of system at this wavelength divided by the number of photon packages in the simulation.

2. Immediately after the emission, peel-off photon packages are created, launched towards the instruments (one for every instrument), and recorded at the correct pixel in each instrument's focal plain. The luminosity of each peel-off photon depends on the total optical depth along the path towards the observer, which has to be calculated by adding the individual contribution of each cell crossed.

3. Subsequently, the photon package travels through the dust grid along a straight path, defined completely by the initial position and the propagation direction. The total optical depth along the path is calculated in a similar way as for the peel-off photon packages.

4. The next step consists of splitting the luminosity of the photon package into $N + 2$ parts, where N is the number of dust cells along its path. One part escapes from the system, N parts are absorbed (one part in each dust cell along the path), and the remaining part is scattered (this is the photon package that actually contributes the loop). The contribution of each of these fractions is calculated based on the distribution of the dust along the path (for details, see Baes et al. 2011; Steinacker et al. 2013).

5. The final step is the simulation of the scattering event, or more concretely the determination of the position of and the propagation direction after the scattering. The former is determined by generating a random optical depth from a truncated exponential probability distribution, the latter by generating a random scattering angle from the scattering phase function.

With this new luminosity, position, and propagation direction, the loop can be started again (starting at step number 2). This cycle is repeated until the photon packages has lost virtually all of its initial luminosity (typical values are 99.99%).

The general routine sketched above is obviously only a simple guide line that is not

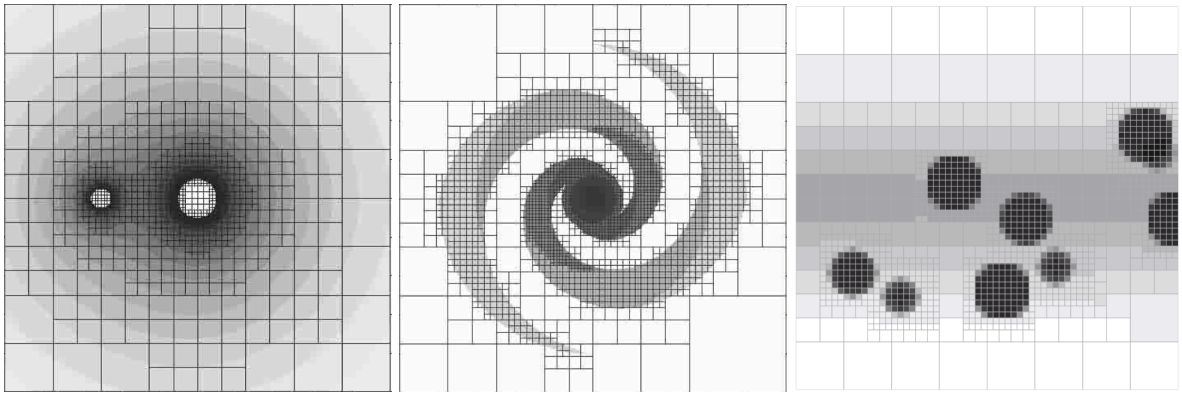

Figure 1.9: Illustration of the use of hierarchical octrees in dust radiative transfer. The left-hand panel shows a model of a binary star system surrounded by a common enveloppe (Kurosawa and Hillier 2001), the middle panel presents a two-armed pseudo spiral galaxy (Kurosawa and Hillier 2001), and the right-hand panel shows a clumpy interstellar dust medium (Bianchi 2008). In all cases, the octrees are constructed such that the grid cell size decreases for high density regions. For the sake of simplicity, the figures show 2D cuts through the 3D grids.

followed exactly by all Monte Carlo codes. Different codes obviously use slightly different algorithms that can results in subtle but possibly crucial differences, depending on the application. For more information we refer to Whitney (2011) and Steinacker et al. (2013), and the references therein.

1.2.3 Advanced grids in Monte Carlo radiative transfer

A crucial aspect of 3D Monte Carlo radiative transfer simulations that we have not yet highlighted is the choice of the dust grid. On the one hand, it is useful to maximise the number of cells, in order to obtain the highest resolution possible. On the other hand, the memory requirements of the simulation scale roughly linearly with the number of grid cells, which puts a limit to the number of cells. Perhaps even more restrictive is that the run time of a Monte Carlo simulation depends critically on the number of dust cells. This is due to two different reasons. First, the most processor-intensive part of a Monte Carlo simulation is the calculation of the path of each photon package through the dust grid, i.e. the calculation of each cell that the photon package crosses and the physical distance (or optical depth) covered in each individual cell. With more cells, the average number of dust cells crossed increases, which increases the total simulation run time. Secondly, Monte Carlo simulations, especially those including thermal dust re-emission, are typically terminated when the radiation field (or the dust temperature) in each cell has converged according to a preset criterion. With more dust cells, the probability that a photon package crosses a given cell is strongly diminished, which implies that more photon packages are needed to achieve the desired accuracy.

The simplest grids that one can use in a 3D Monte Carlo radiative transfer code are

uniform cartesian grids, in which each dust cell is a similarly sized little cuboid. The obvious drawback of such a grid structure is that, for a given number of cells, the effective resolution that can be obtained is limited. Such grid structures are hence not very efficient to simulate systems with a large dust density gradient or a large dynamic range of densities. Ideally, the size of the grid cells should be linked to the dust mass, optical depth or temperature of the dusty medium: the cells should be small where the dust density is high or the radiation field shows a large gradient, and they can be bigger where the dust density is low and the radiation field does not change significantly.

The most obvious grid structures that can cover a large dynamic range are hierarchical grids, or more general hierarchical grid-in-grid structures. In this large family of hierarchical grids, octrees are the most popular variant. They are widely used in all areas of science and engineering, especially in computer graphics and 3D game engines (Jackins and Tanimoto 1980; Bentley 1975; MacDonald and Booth 1990; Havran 2000). In computational astrophysics, they are popular in N-body and hydrodynamics codes (Barnes and Hut 1986; Hernquist 1987; Hernquist and Katz 1989; Teyssier 2002; Springel 2005).

Octree and similar grid structures have recently been implemented in several Monte Carlo dust radiative transfer codes (e.g., Kurosawa and Hillier 2001; Wolf 2003; Harries et al. 2004; Jonsson 2006; Bianchi 2008; Niccolini and Alcolea 2006; Robitaille 2011; Heymann and Siebenmorgen 2012; Lunttila and Juvela 2012), and UV ionisation and Lyα transfer codes (e.g., Tasitsiomi 2006; Laursen et al. 2009). Figure 1.9 shows a number of examples. A detailed analysis of their properties in a radiative transfer context, however, has not been done. In particular, there are many different options for hierarchical grid construction and traversal, and to the best of our knowledge, it has never been investigated in depth which options are the most favourable.

1.3 Goals and outline of this thesis

The overall goals of this thesis are to develop a methodology for the use of advanced hierarchical grid structures in Monte Carlo radiative transfer codes, implement such grids in the 3D dust Monte Carlo code SKIRT, critically investigate the best methods concerning grid construction and traversal, and apply these advanced grids on simulated galaxies to investigate the nature of the dust energy balance problem.

In Chapter 2, we introduce the SKIRT code that we will use for our modelling. SKIRT is a publicly available 3D dust radiative transfer code, based on the Monte Carlo method (Baes et al. 2011; Camps and Baes 2015). The code is developed by the UGent group. We briefly present the main characteristics and structure of the code, and then focus on the existing dust grid structures in the code.

In Chapter 3, we discuss the implementation of two different advanced dust grid structures in SKIRT. Looking at the literature in the field of computational geometry and the 3D computer graphics, there is a wealth of choices to partition 3D spaces. The most common structures are hierarchical tree grids that partition space by recursively subdividing it into subvolumes, including BSP (Binary Space Partitioning) trees, octrees, *k*-d trees, s-octrees, etc. We implement the two most obvious choices, namely octree and *k*-d tree grids, in SKIRT. For both kinds of grids, we consider two different flavours for the grid cell subdivision. Using a suite of three different test models with 3D geometries that represent realistic cases of astronomical systems, and different quality metrics that characterise the power of the grids, we compare the characteristics of these different grid structures in the frame of Monte Carlo radiative transfer simulations.

Chapter 4 is devoted to grid traversal. The most time-consuming part of Monte Carlo simulations is the grid traversal, i.e., calculation of the path of the photon packages through the dusty medium. It essentially comes down to calculating, for each path, the ordered list of dust cells that the path intersects, and the physical distance covered in each individual cell. In simple cartesian grids, grid traversal is a fairly straightforward operation, but this is less so for hierarchically structured grids. A simple top-down method is the most simple algorithm, but not necessarily the fastest. In the computational geometry literature, different algorithms have been proposed for accelerating grid traversal (Glassner 1984; Havran 1999, 2000). Inspired by these methods, we implement three different ways to traverse octree and *k*-d tree grids. Based on the same test models as in the previous Chapter, we compare their performance in the context of Monte Carlo radiative transfer.

In Chapter 5, we investigate a third aspect of hierarchical grids in Monte Carlo radiative transfer, namely the optimal criteria that control the subdivision of the cells

during the construction. An optimal grid for radiative transfer simulations would be based on the changes of the radiation field – the grid cells should be small where the radiation field changes quickly, and can be larger where the intensity varies more gradually. Unfortunately, this can not be done at the start of a simulation, as the radiation field is exactly what we try to compute with a radiative transfer simulation. In principle, one could consider an iterative process where the radiative transfer simulation is repeated several times, and the grid is refined based on the result of the previous iteration. However, this is a very time-consuming process. As an alternative, we can also attempt to create suitable grids based on intelligent grid subdivision criteria that we can determine before the start of the simulation. In this Chapter, we consider and implement different subdivision stopping criteria for hierarchical grids, and compare them in terms of accuracy and speed. In addition, we implement a stopping criterion that can resolve the sharp edges in some models where the gradient in the dust density is very strong.

In Chapter 6, we apply the advanced grids discussed before to run Monte Carlo radiative transfer on realistic simulations of spiral galaxies to investigate the dust energy balance problem. We study two Milky Way-like galaxies produced by high-resolution hydrodynamical simulations with very complex geometries. We simulate them with SKIRT to create mock optical edge-on images of these galaxies, and we then fit these images using the fitting code FitSKIRT (De Geyter et al. 2013, 2014). We repeat the same study on two basic toy models (a smooth exponential disc with a spiral perturbation and a smooth exponential disc with random clumps) by creating edge-on mock images with SKIRT and fitting them using the same techniques. We compare the fitting results of the hydrodynamical models and the basic models, and interpret the results in light of the dust energy balance problem.

Finally, in Chapter 7 we summarise the results obtained in this thesis, and we present an outlook to the future with suggestions to extend the analysis presented in this thesis (both in English and in Dutch).

2 The SKIRT radiative transfer code

This Chapter gives a general overview of the SKIRT code, which is the result of the collaborative work of the UGent SKIRT group. My main contribution to the development of SKIRT is the implementation of the hierarchical grid structures discussed in the following Chapters, but I have also made minor contributions to various other aspects of the code. Part of the material presented in this Chapter is published in Baes et al. (2011) and Camps et al. (2013).

2.1.1 Introduction

SKIRT is a state-of-the-art 3D dust radiative transfer code, based on the Monte Carlo technique. The name SKIRT is an acronym for Stellar Kinematics Including Radiative Transfer, which reflects the original motivation for its creation: study the effects of dust absorption and scattering on the observed kinematics of galaxies. The first version of SKIRT was presented by Baes et al. (2003). Since then, the SKIRT code has continuously been extended and improved; updated versions are presented by Baes et al. (2011) and Camps and Baes (2015). At this moment, SKIRT is a versatile code that can be used for various purposes. It is primarily focused on radiative transfer simulations on galaxy-wide scales (Gadotti et al. 2010; Baes et al. 2010; De Looze et al. 2014; Schaye et al. 2015), but has also been applied to model other environments, including circumstellar discs (Baes et al. 2007), active galactic nuclei (Stalevski et al. 2012), molecular clouds (Hendrix et al. 2015), binary star systems (Deschamps et al. 2015), and galaxies (Schaye et al. 2015; De Geyter et al. 2014; De Looze et al. 2014).

In this section we will present the general characteristics of the SKIRT code from different perspectives, and give a short introduction about the inverse radiative transfer code FitSKIRT.

2.1.2 General characteristics

SKIRT can operate in two modes: *oligochromatic* and *panchromatic* mode. Oligochromatic radiative transfer simulations perform a simulation at a single or a modest number of individual wavelengths. Absorption and multiple anisotropic scattering by dust grains is taken into account, but thermal dust emission is not. These simulations are useful when we want to study the extinction by dust at UV, optical and near-infrared wavelengths. Alternatively, panchromatic radiative transfer simulations cover a full set of wavelengths ranging from UV to FIR/submm wavelengths, and thermal dust emission is computed in a self-consistent way. SKIRT handles different dust mixtures and calculates the temperature distribution of all different grain species separately, taking into account the stochastic heating of small grains and PAH molecules. The dust emission spectrum can be calculated for each dust cell individually, or a library approach can be used to increase the efficiency (Baes et al. 2011).

From an algorithmic point of view, SKIRT makes use of the large effort that has been done by the Monte Carlo radiative transfer community to fight the burden of Poisson noise. It includes implementations of the most common Monte Carlo optimisation

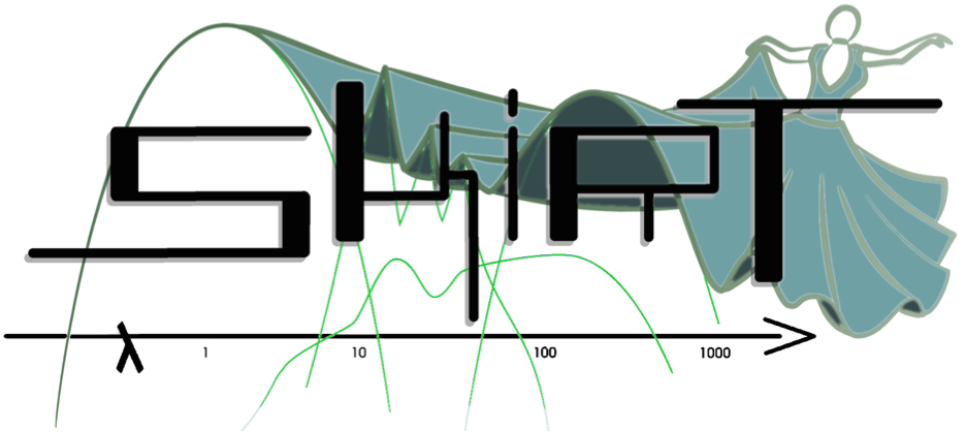

Figure 2.1: The SKIRT logo

techniques, such as peel-off at emission and scattering events, continuous absorption, and forced scattering. A number of experimental optimisation techniques are available as an option.

From the technical point of view, SKIRT is completely written in object-oriented style in C++, and uses some of the capabilities of the Qt cross-platform application framework where needed. There are no dependencies on other libraries. Special care has been devoted to the overall architecture of the code. Inspired by standard software design principles and patterns, the latest version of SKIRT has a modular implementation that can be easily maintained and expanded (Camps and Baes 2015).

SKIRT is parallelised using MPI and QThreads. Multithreading in SKIRT is designed according to the master-slave model (one process hands out pieces of work to the other processes), whereas the MPI parallelisation uses a peer-to-peer model (the processes work independently, without getting instructions from other processes). SKIRT has been run successfully on both large shared-memory machines and high-performance clusters.

From the point of view of usability, considerable efforts have been made to make the code as user-friendly and accessible as possible. It is fully documented: every single class is documented[1], an installation guide, user guide and developer guide are available, and extensive additional information is available on a number of selected topics. The code is publicly available on GitHub[2].

SKIRT offers a large number of built-in options to configure the different aspects of the radiative transfer simulation, including spatial and spectral distributions, dust grain characteristics, simulated detection systems, in addition to various mechanisms for

[1] SKIRT documentation: http://www.skirt.ugent.be
[2] SKIRT code repository: https://github.ugent.be/skirt/skirt

```
<?xml version='1.0' encoding='UTF-8'?>
<!--SKIRT radiative transfer simulations - © 2012-2014 Astronomical Observatory, Ghent University-->
<skirt-simulation-hierarchy type="MonteCarloSimulation" format="6.1" producer="Python Toolkit for SKIRT (SkiFile class)" time="2014-08-
06T11:12:16">
 <OligoMonteCarloSimulation packages="5e7">
  <random type="Random">
   <Random seed="4357"/>
  </random>
  <units type="Units">
   <ExtragalacticUnits/>
  </units>
  <instrumentSystem type="InstrumentSystem">
   <InstrumentSystem>
    <instruments type="Instrument">
     <FullInstrument instrumentName="i0" distance="5 Mpc" inclination="0 deg" azimuth="0 deg" positionAngle="0 deg"
      pixelsX="1024" extentX="35000 pc" pixelsY="1024" extentY="35000 pc" scatteringLevels="0"/>
    </instruments>
   </InstrumentSystem>
  </instrumentSystem>
  <wavelengthGrid type="OligoWavelengthGrid">
   <OligoWavelengthGrid wavelengths="0.3573 micron, 0.471819 micron, 0.62 micron, 0.7522 micron, 0.89222 micron"/>
  </wavelengthGrid>
  <stellarSystem type="StellarSystem">
   <StellarSystem>
    <components type="StellarComp">
     <OligoStellarComp luminosities="1e9 , 1.1e9 , 1.85e9 , 2.59e9 , 3.38e9 ">
      <geometry type="Geometry">
       <SpheroidalGeometry flattening="0.56">
        <geometry type="SpheGeometry">
         <SersicGeometry index="2.61" radius="2310 pc"/>
        </geometry>
       </SpheroidalGeometry>
      </geometry>
     </OligoStellarComp>
     <OligoStellarComp luminosities="1.5e9 , 1.59e9 , 2.27e9 , 3.05e9 , 3.97e9 ">
      <geometry type="Geometry">
       <ExpDiskSpiralArmsGeometry radialScale="4230 pc" axialScale="510 pc" radialTrunc="0 pc" axialTrunc="0 pc"
       arms="2" pitch="20 deg" phase="0 deg" perturbWeight="0.3"/>
      </geometry>
     </OligoStellarComp>
    </components>
   </StellarSystem>
  </stellarSystem>
  <dustSystem type="OligoDustSystem">
   <OligoDustSystem sampleCount="100" writeConvergence="true" writeDensity="true" writeQuality="false"
   writeCellProperties="false" writeCellsCrossed="false">
    <dustDistribution type="DustDistribution">
     <CompDustDistribution>
      <components type="DustComp">
       <DustComp>
        <geometry type="Geometry">
         <ExpDiskSpiralArmsGeometry radialScale="6030 pc" axialScale="230 pc" radialTrunc="35000 pc"
         axialTrunc="0 pc" arms="2" pitch="20 deg" phase="0 deg" perturbWeight="0.4"/>
        </geometry>
        <mix type="DustMix">
         <DraineLiDustMix writeMix="true" writeMeanMix="true"/>
        </mix>
        <normalization type="DustCompNormalization">
         <DustMassDustCompNormalization dustMass="3.02e7 Msun"/>
        </normalization>
       </DustComp>
      </components>
     </CompDustDistribution>
    </dustDistribution>
    <dustGridStructure type="DustGridStructure">
     <BinTreeDustGridStructure writeGrid="true" extentX="35000 pc" extentY="35000 pc" extentZ="5000 pc"
     minLevel="5" maxLevel="40" searchMethod="Neighbor" sampleCount="100"
     maxOpticalDepth="0" maxMassFraction="1e-6" maxDensDispFraction="0" directionMethod="Alternating"/>
    </dustGridStructure>
   </OligoDustSystem>
  </dustSystem>
 </OligoMonteCarloSimulation>
</skirt-simulation-hierarchy>
```

Figure 2.2: The structure of a `ski` file (a SKIRT parameter input file) configured during the query and answer session to create a simulation of a spiral galaxy.

importing snapshots generated by hydrodynamical simulations. Complex simulations can be set up without any coding at all: the configuration for a particular simulation is defined at runtime with a user-friendly command-line interface, or with a graphical in-

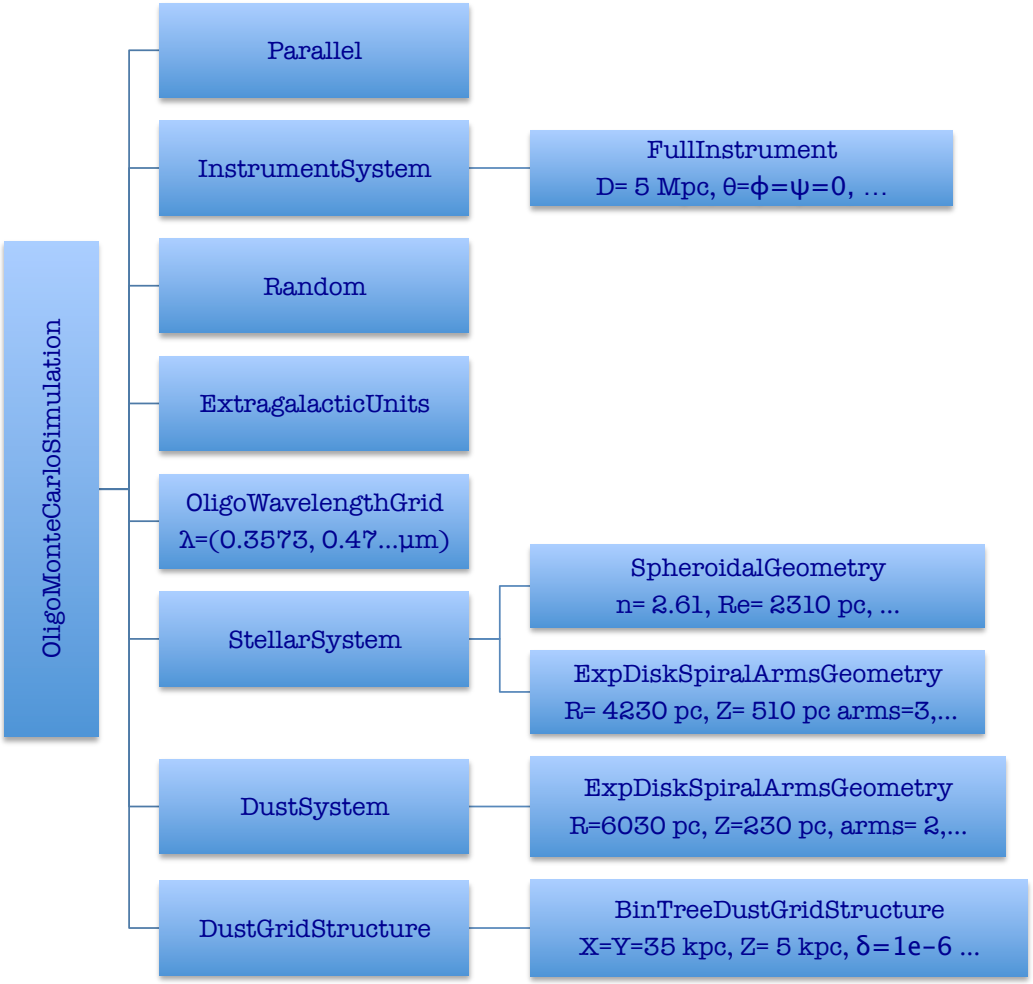

Figure 2.3: The run-time object hierarchy that corresponds to the model constructed based on `ski` file shown in Figure 2.2. Every rectangle represents a simulation item with the name and values of its properties. Each simulation item instance and each property in this hierarchy maps directly to an XML element or attribute in the `ski` file with the same name.

terface called the SKIRT MakeUp. Both of these user interfaces take the user through all possible options in the code, narrowing down the possibilities based on earlier choices. When this task is finished, all the options and values chosen by the user are saved into a `ski` file, an XML-based document. The `ski` file mimics the run-time object hierarchy with the same names for simulation items and attributes. Figure 2.2 shows the `ski` file of a spiral galaxy simulation where the run-time hierarchy for this simulation is represented in Figure 2.3. SKIRT relies on the Qt introspection features to automatically construct a user interface from the C++ class declarations in the code (Camps and Baes 2015).

2.1.3 Inverse radiative transfer with FitSKIRT

In its standard mode, the user provides the characteristics of a model setup, and SKIRT calculates the observable properties of the model (images, SEDs, spectra...), as well as a number of intrinsic properties of the radiation field (radiation field strengths, dust temperatures...). Beside this standard mode, SKIRT contains an important extension called FitSKIRT. This code is designed to recover the 3D distribution and spectral properties of dust and stars in dusty galaxies by directly fitting radiative transfer models to optical and near-infrared images. FitSKIRT combines SKIRT with the power of the genetic algorithms-based optimisation library GAlib (Wall 1996) to perform the actual fitting. The first version of FitSKIRT, presented by De Geyter et al. (2013), was a monochromatic code, i.e. the FitSKIRT tool fitted a radiative transfer model to a single image. The most recent version of FitSKIRT is oligochromatic, i.e. it can read an arbitrary number of images in different bands and simultaneously fit a radiative transfer model to them based on an arbitrary combination of stellar and dust components (De Geyter et al. 2014). Oligochromatic fitting is less sensitive to degeneracies between the different model parameters than monochromatic fitting procedures, i.e. the model parameters that describe the stellar and dust distributions can be determined with more accuracy.

2.2.1 The `DustGridStructure` class

The `DustGridStructure` class in SKIRT is the abstract class that represents all kinds of dust grids that can be used during a radiative transfer simulation. Dust grid structures are essentially just a collection of non-overlapping dust cells, which together partition a given configuration space. Each position in the computational domain belongs to a single dust cell, which has a number of characteristics that describe the physical properties of the dust at the location of the cell. At the moment, it is assumed that the physical properties, such as density, opacity, or radiation field strength, are uniform within each cell, although this is not absolutely necessary in Monte Carlo radiative transfer (see e.g., Baes et al. 2003; Niccolini et al. 2003).

In each simulation where dust is present, exactly one dust grid structure, i.e. one concrete derived class from the `DustGridStructure` inheritance hierarchy, must be cho-

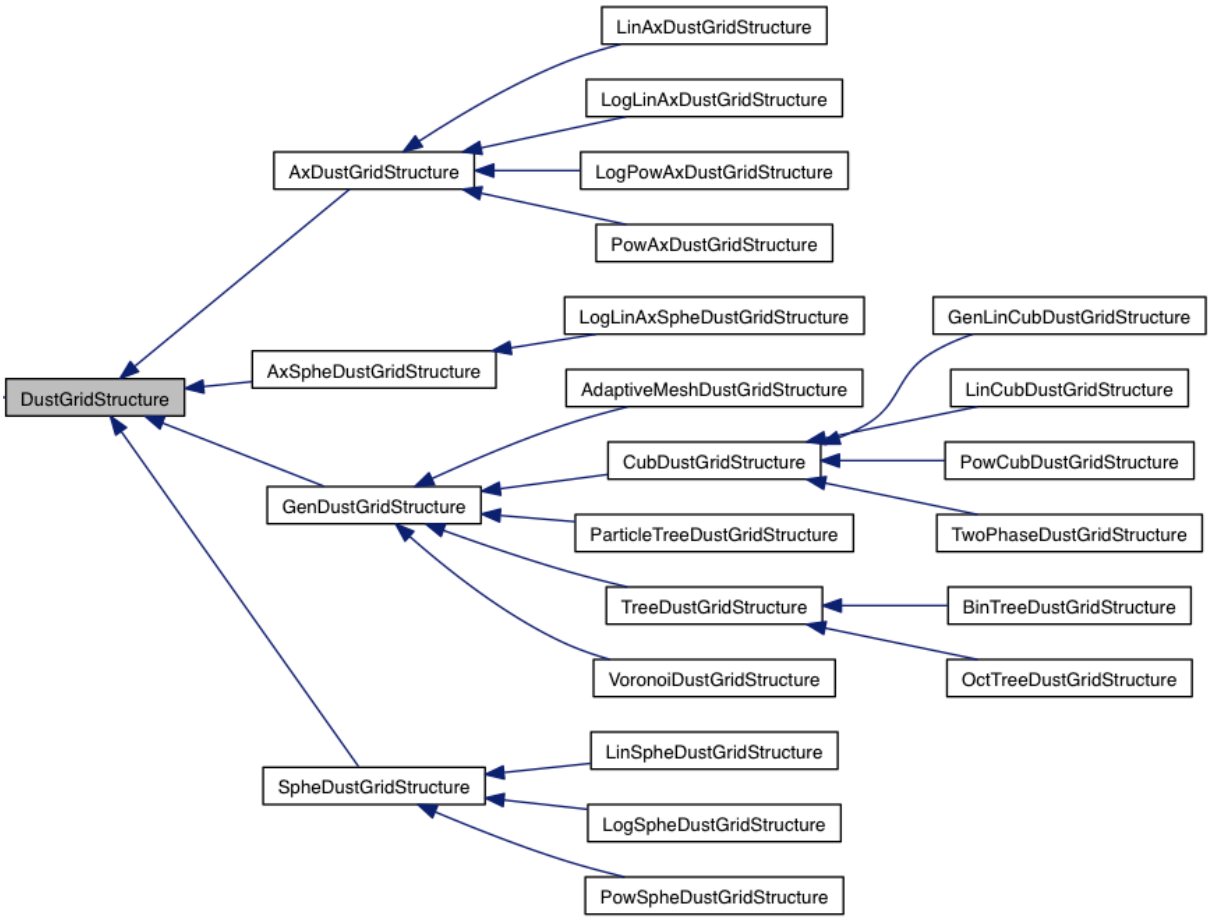

Figure 2.4: The inheritance diagram of the abstract `DustGridStrucure` class.

sen. Figure 2.4 shows the inheritance diagram of the `DustGridStructure` class. The `DustGridStructure` class has different subclasses that represent groups of grid structures with different degrees of symmetry. For example, the `SpheDustGridStructure` subclass represents all grids with a spherical symmetry, i.e. grids where the elementary cells are concentric spherical shells. It is an abstract class on its own, and has various subclasses that correspond to specific distributions of shells. When we want to create a new dust grid structure in the code, a new class with a specific name should be created and it should be tied into the `DustGridStructure` class hierarchy.

The declaration of the abstract `DustGridStructure` class looks as follows:

```
class DustGridStructure : public SimulationItem
{
protected:
    DustGridStructure();
    void setupSelfBefore();
    void setupSelfAfter();
public:
    virtual int dimension() const = 0;
    int Ncells() const;
    virtual double xmax() const = 0;
    virtual double ymax() const = 0;
    virtual double zmax() const = 0;
    virtual double weight(int m) const {return 1.0;}
    virtual double volume(int m) const = 0;
    virtual int whichcell(Position bfx) const = 0;
    virtual Position centralPositionInCell(int m) const = 0;
    virtual Position randomPositionInCell(int m) const = 0;
    virtual void path(DustGridPath* dgp) const = 0;
protected:
    int _Ncells;
};
```

This class declaration immediately shows the functionality that needs to be provided by all the dust grid classes that inherit from this abstract class.

- Each concrete dust grid class should provide a number of elementary functions that indicate the basis characteristics of the geometry. The `dimension()` function returns the dimension of the grid (equal to 3 for a general 3D geometry), and obviously `xmax()`, `ymax()` and `zmax()` return the extent of the grid.

- Each dust grid structure in SKIRT is essentially an array of cells, each characterised by a cell number m ranging from 0 to $N_{\text{cells}} - 1$. The function `volume(int m)` should return the volume of the dust cell with cell number m, and the function `weight(int m)` returns the weight of that cell. Note that the latter function is not an abstract function, and that it standardly returns one for all dust cells. It is only for special kinds of dust grids that this member function is overwritten and that this weight comes into play.
- The `whichcell(Position bfx)` function should return the cell number of the cell that contains a given position $\boldsymbol{x}$. Similarly, `centralPositionInCell(int m)` and `randomPositionInCell(int m)` should return the central and a random position within the dust cell with cell number m, respectively.
- The `path(DustGridPath* dgp)` function is responsible for the actual grid traversal. For a given starting position $\boldsymbol{x}$ and a propagation direction $\boldsymbol{k}$, it should calculate an ordered list of all the cells that are crossed by the path defined by $\boldsymbol{x}$ and $\boldsymbol{k}$. It should also return the physical path length Δs covered within each cell, and the cumulative path length s covered along the entire path up to the end point of each crossed cell. Given additional information about the dust properties in each cell (at a particular wavelength), this information can then be used to calculate optical depth information for the path. All of this information is stored in a structure of the `DustGridPath` type.

When a new type of dust grid structure is considered, a customised implementation of each of these functions must be provided, together with the specific construction algorithms that actually construct the grid. The latter is done using the constructor and the `setupSelfBefore()` and `setupSelfAfter()` functions – for more information on this method of construction, see Camps and Baes (2015). Which functions are the most complex in terms of implementation depends on the specific type of dust grid that is being considered, but it is usually `whichcell(Position bfx)` and `path(DustGridPath* dgp)`.

2.2.2 A 3D cartesian grid as an example

As an example of a grid structure in SKIRT, we consider a relatively simple case, namely a 3D cartesian grid (the `CubDustGridStructure` class in SKIRT). The configuration space considered is the cuboidal volume defined by $-x_{\text{max}} < x < x_{\text{max}}$, $-y_{\text{max}} < y < y_{\text{max}}$, and $-z_{\text{max}} < z < z_{\text{max}}$. Along the x-axis, we define a set of N_x grid points $\{x_i\}$, with

$$-x_{\text{max}} = x_0 < x_1 < \ldots < x_{N_x-1} < x_{N_x} = x_{\text{max}} \tag{2.1}$$

and we define similar sets $\{y_j\}$ and $\{z_k\}$ along the two other axes. The distribution of the grid points is arbitrary. The most simple option is to use an equidistant grid along each of the axes, but other options are also possible (and available in SKIRT). A grid cell is simply a little cuboid defined as

$$x_i < x < x_{i+1}, \tag{2.2}$$

$$y_j < y < y_{j+1}, \tag{2.3}$$

$$z_k < z < z_{k+1}. \tag{2.4}$$

The actual grid structure consists of these $N_{\text{cells}} = N_x N_y N_z$ cuboidal cells that together partition the configuration space. Each cell has a unique cell number

$$m = k + j\,N_z + i\,N_z N_y \tag{2.5}$$

This equation expresses the one-to-one relation between cell number m and the triplet (i, j, k) of indices corresponding to the individual axes.

If we want to introduce the `CubDustGridStructure` class in SKIRT, we have to implement each of the virtual member functions of the abstract `DustGridStructure` class. Most of these are almost trivial to implement: in particular, the volume, the central position and a random position in the cell with given cell number m is easily found. In this case, also the `whichcell(Position bfx)` function is easily implemented: we only need to find the grid points along each of the axes that bracket the cartesian coordinates of the position, and return the corresponding cell number. This bracketing is done using a simple bisection algorithm (Press et al. 1992).

The only complex function is the `path(DustGridPath* dgp)` function that does the actual grid traversal. First, we determine in which grid cell the path starts, and in which direction the path is directed. Assume that the starting position $\boldsymbol{x} = (x, y, z)$ is located in the cell $m \equiv (i, j, k)$ and that the direction $\boldsymbol{k} = (k_x, k_y, k_z)$ is such that $k_x > 0$, $k_y > 0$ and $k_z > 0$, i.e. the path moves "forward" in the x, y and z directions. The calculation of the path now consists of a loop where a number of simple steps are repeated.

1. The first step is the determination of the path length from the current position to the intersection with the different walls that the path might cross. The walls are planes aligned with the principle planes of the cartesian coordinate system, i.e. $x = x_{\text{E}}$, $y = y_{\text{E}}$ or $z = z_{\text{E}}$. In our present case (Figure 2.5), with a path that moves forward relative to the three principle axes, we have $x_{\text{E}} = x_{i+1}$, $y_{\text{E}} = y_{j+1}$ and

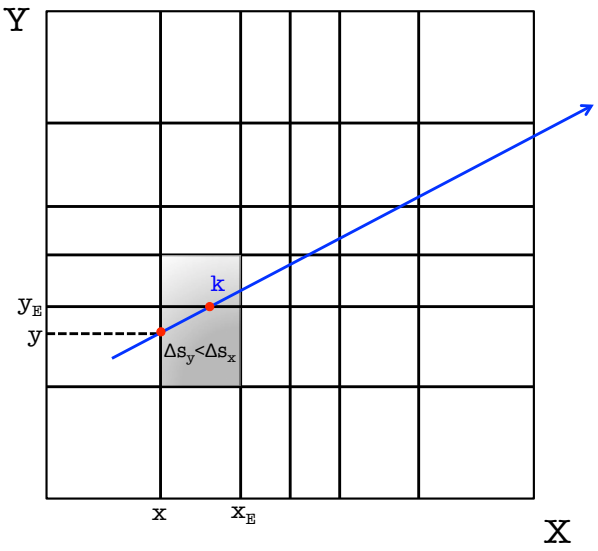

Figure 2.5: 2D illustration of path through a cartesian grid. The grey cells are the current and next cell. From the current position in the cell, the two intersection points with the walls are calculated, and depending on which wall is hit first, the next cell is determined. In this case, $\Delta s_y < \Delta s_x$, so the path leaves the cell from the top wall.

$z_E = z_{k+1}$, respectively. The wall that will be crossed first is found using

$$\Delta s = \min\left(\frac{x_E - x}{k_x}, \frac{y_E - y}{k_y}, \frac{z_E - z}{k_z}\right) \tag{2.6}$$

2. Once the correct exit wall is found, we advance the current position of the path to the intersection with the exit wall. Assume, for example, that the wall $y = y_E$ is hit first, then we move the current position to

$$\boldsymbol{x} = (x + k_x \Delta s, y_E, z + k_z \Delta s) \tag{2.7}$$

3. We store the information on the cell that we have just crossed. More precisely, we append the cell number m, the distance Δs covered in this cell, and the cumulative covered distance s to the `DustGridPath` object that gradually grows as we traverse through the grid.

4. Finally, we prepare for the traversal of the next grid cell. Since we crossed the wall corresponding to the y direction, the next cell that we have to cross is the one characterised by the triplet $(i, j+1, k)$. Also the list of the next walls that might be hit next is updated (in our case, x_E and z_E remain the same, and y_E is set to y_{j+2}.

This loop is repeated until the path crosses the outer boundary of the configuration

space. The `DustGridPath` then contains all the information on the path.

This algorithm is relatively straightforward, since the next dust cell along the path is always automatically obtained by just increasing or decreasing one of the three cell indices. Finding the next cell along the path can be more difficult when we choose other types of grids like hierarchical or unstructured grids.

2.2.3 Other grids in SKIRT

SKIRT is equipped with a variety of dust grid structures, as can be seen in Figure 2.4. The reason why so many are implemented, and why more are added in the frame of this thesis, is that the choice of the grid is crucial for the efficiency of the radiative transfer simulations. If we had an infinite amount of computational time and memory, all simulations could be run with 3D cartesian grids as presented in the previous subsection. However, this would not be the optimal choice for many cases.

- When the distribution of sources and sinks has a certain symmetry, such as spherical or axial symmetry, it is usually advantageous to exploit this symmetry and use corresponding 1D or 2D grids rather than general 3D grids. This is particularly important when speed is crucial, e.g. in inverse radiative transfer modelling with FitSKIRT.
- Cartesian grids with a fixed distribution of the grid points often do not have the required dynamic range to resolve the structures that physically need to be resolved. In this case it is better to use more advanced 3D grids that automatically adapt their resolution where needed. The implementation and characterisation of such grids in SKIRT is one of the goals of this thesis.
- As discussed in Section 1.1.3, radiative transfer simulations are often used to post-process snapshots from hydrodynamic simulations. The radiative transfer simulations are best performed on the same grid as used for the hydrodynamic simulations; doing otherwise would unavoidably introduce resampling inaccuracies and additional overhead. Many hydrodynamics simulations are performed on adaptively refined grids (Fryxell et al. 2000; Bryan et al. 2014), and also simulations on unstructured Voronoi grids are gaining popularity (Springel 2010; Duffell and MacFadyen 2011). It therefore makes sense to implement grid structures in SKIRT to post-process the output from hydrodynamic simulations.

In the remainder of this subsection, we will briefly present a few of the grid structures currently available in SKIRT. We do not aim to present a complete overview, or to provide all the details; the goal is just to give a taste of the complexities that are encountered when different grid structures are considered.

The SpheDustGridStructure class is a subclass of the general DustGridStructure class, and represents one-dimensional, spherically symmetric dust grid structures. The configuration space is a large sphere, and each cell is a spherical shell. This grid is completely defined by the distribution of grid points in the radial direction (different radial grid point distributions are implemented as different concrete subclasses of the abstract SpheDustGridStructure class). Most of the functionality that is required, such as the identification of the cell number corresponding to a given position or the generation of a random position in a given dust cell, are straightforward to implement. Not surprisingly, the grid traversal function is the most complex one. Since there is only a one-dimensional grid, the calculation of the next cell is straightforward. The biggest difference with the 3D cartesian grid is that the propagation can be both inward and outward in radius along a single path; some bookkeeping is required to take that into account.

SKIRT also contains two types of dust grids specifically adapted to 2D axisymmetric systems. Both of them consist of a 2D grid in the meridional plane that is subsequently rotated around the symmetry axis. Each grid cell is hence a torus. The difference between the two families is the coordinate system used: the AxDustGridStructure uses cylindrical coordinates, whereas the AxSpheDustGridStructure uses spherical coordinates. Again, most of the functionality is fairly trivial to implement; the only complex function is the one that performs the actual grid traversal. The algorithm used for the grid traversal combines elements of the one for the 1D spherical grid (propagation can be inward and outward in radius along a single path) and the one for the 3D cartesian grid (testing is required to find out which cell wall is crossed first).

A peculiar grid structure is the so-called two-phase dust grid structure, implemented in the TwoPhaseDustGridStructure class. The underlying grid structure is a uniform 3D cartesian grid, in which all cells are cuboids with exactly the same dimension. The peculiar characteristic of this grid is that an additional weight factor is attached to each dust cell (it is currently the only grid structure that overwrites the default behaviour of the weight(int m) function). These weight factors are determined during setup using the method described by Witt and Gordon (1996). According to this algorithm, each individual cell in the grid is assigned randomly to either a high- or a low-density state. When a smooth dust density distribution is discretised on this grid, the grid structure can take into account this additional weight factor to simulate a two-phase distribution, with a low-density and a high-density medium. One of the free parameters is the filling factor, which determines the statistical frequency of the cells in the high-density state. For filling factor values larger than 0.25, clumps start to form an interconnected sponge-like structure, with low-density medium filling the voids. Examples of the use of this two-phase dust grid are the model for the edge-on spiral galaxy UGC 4754 by

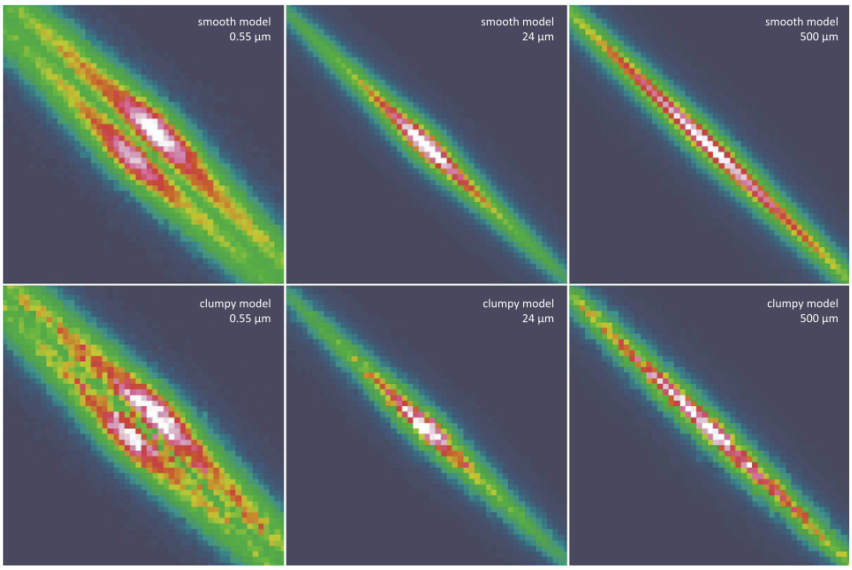

Figure 2.6: Simulated SKIRT images corresponding to smooth (top row) and clumpy (bottom row) 3D models for the edge-on spiral galaxy UGC 4754 by Baes et al. (2011). For the smooth model, a 3D cartesian grid structure with $401 \times 401 \times 61$ grid cells was used. For the clumpy model, a two-phase dust grid structure with exactly the same underlying cartesian grid was adopted.

Baes et al. (2011) (see figure 2.6) and the clumpy AGN torus models of Stalevski et al. (2012).

A completely different type of dust grid structure is the `VoronoiDustGridStructure` class. It represents three-dimensional dust grid structures based on a Voronoi tessellation. The class offers several options for determining the locations of the particles generating the Voronoi tessellation. A specified number of particles can be distributed randomly over the domain, either uniformly or with the same overall density distribution as the dust (Figure 2.7, left panel). Alternatively, the locations can be copied from the particles in an SPH dust distribution. This class uses the 3D Voronoi generation code Voro++ (Rycroft 2009). Not surprisingly, some of the member functions are more complex than they are for the regular grids presented before. In particular, the identification of the dust cell that contains a given position is not a trivial function. Due to the nature of Voronoi grids, this is essentially a nearest neighbour search. Rather than looping over all possible sites, SKIRT implements an approach using cuboidal blocks, as explained in detail in Camps et al. (2013). This task could be optimised even further using more advanced techniques based on space partitioning structures such as k-d trees or R-trees. Also the generation of random positions from a given cell is less trivial, for which we use a rejection technique with the cuboidal volume as the reference distribution. Finally, the algorithm for grid traversal is surprisingly elegant (Figure 2.7, right panel), as long as the neighbour list of each cell is known – fortunately, this infor-

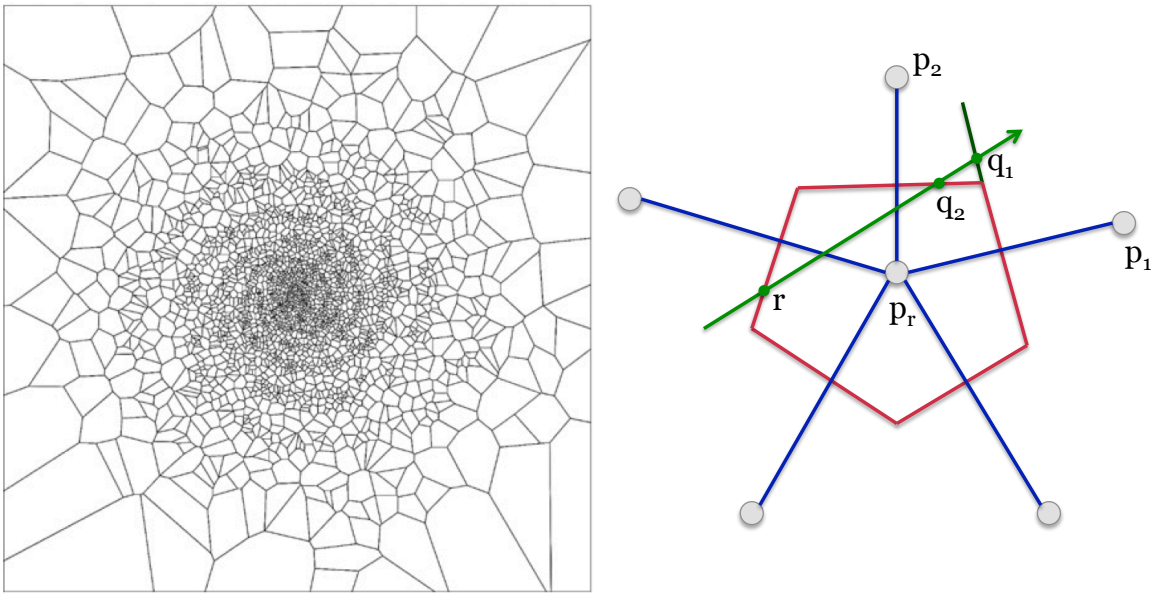

Figure 2.7: Left: a planar cut through an unstructured Voronoi dust grid where the generating sites are placed randomly following the dust density distribution of a logarithmic spiral galaxy model. Note that a planar cut through a 3D Voronoi tessellation is usually not a 2D Voronoi tessellation. Figure taken from Camps and Baes (2015). Right: a 2D illustration of a path through a Voronoi dust cell. The Voronoi cell is shown as the red polygon, the blue lines are the connections between the site of the cell that is being traversed and the sites of the neighbouring cells. The grid traversal algorithm first calculates the intersection between the path and the walls that are crossed; in this 2D case, two walls are found (for the other wall, the intersection is not in the forward direction). The current position is then moved to the first intersection point encountered (position $\boldsymbol{q}_1$) and the same step is repeated.

mation is provided by the Voro++ library. For more information on the use of Voronoi grids in Monte Carlo radiative transfer, we refer to Camps et al. (2013).

3 Octree and k-d tree grid structures in SKIRT

The material presented in this Chapter is original work; it is published in a condensed form in Saftly et al. (2013) and Saftly et al. (2014).

3.1 Introduction

As advocated in Section 1.2.3, uniform cartesian grids are not the most efficient types of grids to use in a Monte Carlo radiative transfer simulation, in particularly not for 3D systems with a large dust density gradient or a large dynamic range of densities. Ideally, the size of the grid cells should be linked to the dust mass, optical depth or temperature of the dusty medium: the cells should be small where the dust density is high or the radiation field shows a large gradient, and they can be bigger where the dust density is low and the radiation field does not change significantly. In order to run simulations with a large dynamic range, grids that can adapt their effective resolution locally are required.

There is a entire zoo of possible space partitioning structures that could be considered that satisfy this criterion. Probably the most popular type is the hierarchical octree grid, which is widely used in computational astrophysics, and which is also implemented in several Monte Carlo radiative transfer codes (e.g., Kurosawa and Hillier 2001; Harries et al. 2004; Jonsson 2006; Niccolini and Alcolea 2006; Bianchi 2008). But octrees are not the only option: a wide variety of similar hierarchical structures can be considered, and each of them has its own strengths and weaknesses. These space partitioning structures are studied more extensively in the field of computational geometry and computer graphics than in astrophysics. For example, Havran (2000) did an extensive comparison of heuristic ray-shooting algorithms based on many different space partitioning structures. He included, amongst others, binary split partitioning or BSP trees (a partitioning in which each cell in recursively subdivided by a plane), *k*-d trees (a special case of the general BSP trees in which the splitting planes are aligned to the model space axes), octrees (a partitioning in which each cell is subdivided in eight subcells), bounding volume hierarchies (a bottom-up tree in which each "object" is confined in a bounded volume, which are recursively combined to larger units), and various kinds of cartesian grids with uniform and nonuniform grid point division. He found that the ray-shooting algorithm based on the *k*-d tree is the winning candidate among all tested algorithms. This suggests that also in the frame of Monte Carlo radiative transfer, it might be useful to look beyond the classical octree.

In this Chapter we introduce two different kinds of hierarchical grid structures (octrees and *k*-d trees), and implement them in the SKIRT Monte Carlo radiative transfer code. From the entire zoo of possible space partitioning structures, these grids were chosen because of their simplicity and their popularity in the various fields of numerical astrophysics. For each type of grid, we introduce two flavours, based on the way how the cells are subdivided during the construction phase (*regular* and *barycentric*). The gen-

eral goal of this Chapter is to compare the characteristics of these four types of grids (octree and k-d tree grids, with regular and barycentric) subdivisions in the frame of Monte Carlo radiative transfer simulations. In order to do so, we consider three different test models with 3D geometries that represent realistic cases, and we introduce different quality metrics to characterise the power of the grids.

This Chapter is organised as follows. We present the test models and the quality metrics in Section 3.2. In Section 3.3 we explain how the octree and k-d tree grid structures are constructed and implemented in SKIRT, including a discussion on the different subdivision options. We compare the characteristics of the different grids in Section 3.4, and formulate our conclusions in Section 3.5.

3.2.1 Test models

In order to test the different hierarchical grids we will present in the next section, we have considered three different challenging test models. They were chosen to accommodate a variety of possible geometries that can be encountered in realistic 3D Monte Carlo radiative transfer simulations.

The first model we considered is an idealised model for a spiral galaxy with a three-armed logarithmic spiral structure. This model is completely analytical and is inspired by the models used by Misiriotis et al. (2000) and Schechtman-Rook et al. (2012). Stars in the model galaxy are distributed in two components: a double-exponential disk with a spiral arm perturbation, and a flattened Sérsic bulge. The dust is distributed only in a double-exponential disc, also with a spiral perturbation. For the parameters of the stellar and dust distribution, we used typical values applicable for spiral galaxies (Kregel et al. 2002; Hunt et al. 2004; Cortese et al. 2012); for other parameters, we were specifically inspired by the results obtained from radiative transfer fits to nearby edge-on spiral galaxies (Xilouris et al. 1999; Bianchi 2007; Baes et al. 2010; MacLachlan et al. 2011). Most relevant for the present discussion are the properties of the dust distribution: we used values of 4 kpc and 200 pc for the radial and vertical scale lengths of the disk, and a total dust mass of $10^7\ M_\odot$. 50% of the total dust mass is concentrated in the spiral arms, the remainder is spread smoothly over the entire disc. The spiral arms have a pitch angle of 25 deg. An illustration of the dust density in the central plane of the galaxy is shown on the top left panel of Figure 3.1.

Our second test model is a model for the central region of an active galactic nucleus (AGN). The model consists of a central, isotropic source surrounded by an optically thick dust torus. A large variety of models for such tori have been proposed, ranging from smooth, axisymmetric models (Pier and Krolik 1992; Granato and Danese 1994; Efstathiou and Rowan-Robinson 1995; Schartmann et al. 2005; Fritz et al. 2006) to completely clumpy structures (Nenkova et al. 2002, 2008; Hönig et al. 2006; Hönig and Kishimoto 2010). The model that we adopt here is similar to the AGN torus models presented by Stalevski et al. (2012), in the sense that it consists of a number of compact and optically thick clumps embedded in a smooth inter-clump medium. Contrary to the approach adopted by Stalevski et al. (2012), where the two-phase clumpy medium was generated in a statistical way by applying a clumpiness algorithm (Boissé 1990; Witt and Gordon 1996; Wolf et al. 1998), we now consider a torus model consisting of a smooth distribution of dust to which we add a discrete number of individual clumps (as in Bianchi 2008). The smooth model has an opening angle of 100 deg, an inner ra-

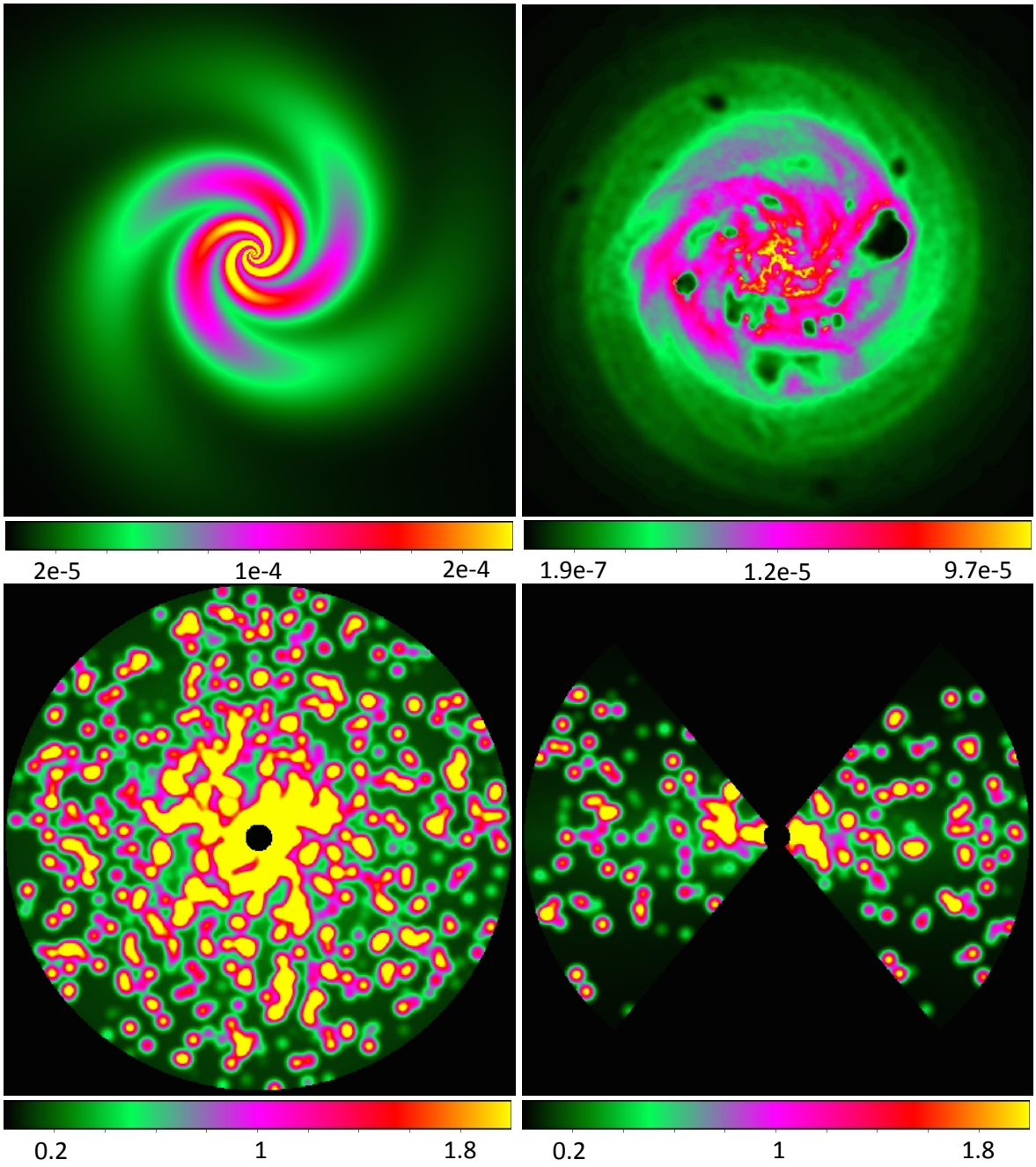

Figure 3.1: Illustration of the geometry of the three test models. The top panels shows a cut through the density in the xy plane of the logarithmic spiral galaxy and the SPH galaxy model (field-of-view of 40 kpc on a side). The bottom panels show the density in the xy and xz planes for the torus model (field-of-view of 30 pc on a side). In all panels, the dust density is given in $M_\odot$ pc^{-3}.

dius of 0.7 pc, an outer radius of 15 pc and a density that falls off as r^{-1} in the radial direction and as $e^{-2\cos\theta}$ in the polar direction. To this smooth dust distribution we add 40,000 individual spherical clumps with a 1 pc diameter and a constant mass density. The contrast between the clump and inter-clump medium is such that 80% of the total

dust mass, set to $4 \times 10^3\ M_\odot$, is distributed in the different clumps, and the remaining mass over the inter-clump medium. An illustration of the dust density in the xy and xz planes of the model is shown in the bottom panels of Figure 3.1.

The last test model we use is a completely numerical spiral galaxy model created by means of a hydrodynamic simulation. The galaxy model we consider is the 1 Gyr snapshot of model run number 6 from Rahimi and Kawata (2012), which represents an M33-sized late-type spiral galaxy. It was run using the N-body/SPH code GCD+ (Kawata et al. 2013) in a fixed dark matter halo, and includes self-gravity, hydrodynamics, radiative cooling, star formation, supernova feedback, metal enrichment and metal diffusion. The model run is characterised by a star formation efficiency of 0.05, an energy output of 10^{51} erg per supernova and stellar wind energy loss of 10^{37} erg per massive star. These relatively large values for the feedback parameters create a turbulent and chaotic interstellar medium, with large holes and bubbles. At the moment of the snapshot, the galaxy has a star formation rate of about 0.2 $M_\odot\ \mathrm{yr}^{-1}$.

The snapshot is characterised by 410,372 stellar particles and 189,628 gas particles. For the calculation of the dust mass density distribution, we follow the approach of Jonsson et al. (2010) and assume that, at every position in the galaxy, a fixed fraction of the metal content is locked in dust grains. To obtain the dust density at a given position, we interpolate the metal density over the SPH gas particles, using the standard cubic spline kernel (Monaghan 1992; Springel 2005), and use a metal depletion in the dust grains of 40% (Dwek 1998). The resulting dust mass density in the equatorial plane of the galaxy can be seen in the top right panel of Figure 3.1. The holes and bubbles caused by the feedback from supernovae and stellar winds are clearly visible.

3.2.2 Grid quality measures

In order to compare the "goodness" of the different grids for radiative transfer purposes, we have to define grid quality metrics. Unfortunately it is not trivial, if not at all impossible, to define unique characteristics of a "good" grid. In broad terms, a good grid should satisfy a number of characteristics.

A first important metric is the total number of cells N_{cells}. For a given dust mass resolution, the ideal grid has as few cells as possible: the memory consumption scales directly with N_{cells} and also the simulation run time is expected to increase with an increasing number of cells. In simulations where not the shooting of photons through the grid, but the calculation of the temperature distribution or the dust emissivity in each cell is computationally the most expensive operation, the simulation run time scales directly with N_{cells}. In many radiative transfer simulations, however, e.g. in pure scattering problems, the grid traversal is computationally the most expensive operation. This

grid traversal is roughly proportional to $\langle N_{\text{cross}} \rangle$, the average number of cells crossed along a single path, so this is also an important metric to take into account. As will be shown later in this Chapter, the two metrics N_{cells} and $\langle N_{\text{cross}} \rangle$ are not always directly related.

The combination of N_{cells} and $\langle N_{\text{cross}} \rangle$ doesn't tell the entire story: even if two grids have the same number of cells and/or the same average number of cells crossed along a path, one can still be considered better than the other, because it has a cleverer placement of the cells and hence a more accurate discretisation of the dust density field. Therefore, we have also considered two grid quality metrics that measure the accuracy of the discretisation.

First, we have evaluated the difference between the true density $\rho_{\text{t}}(\boldsymbol{x})$ and the grid density $\rho_{\text{g}}(\boldsymbol{x})$ in a large number of positions $\boldsymbol{x}$, uniformly sampled from the dust grid volume. Here, $\rho_{\text{t}}(\boldsymbol{x})$ is the value of the density from the input dust density field, and $\rho_{\text{g}}(\boldsymbol{x})$ is the value of the uniform density in the grid cell that contains the position $\boldsymbol{x}$. Subsequently, we calculate the standard deviation, $\Delta\rho$, of the distribution of $\rho_{\text{t}} - \rho_{\text{g}}$ values and use it as a metric to measure the accuracy of the discretisation of the grid. Note that there is no absolute value for this metric that can decide whether a grid is a "good" grid: for each model we can have a different value for this number, depending on the complexity of the geometry and the total mass and distribution of the dust. But it is a useful metric to compare two different grids corresponding to the same model: the grid with the lower value of $\Delta\rho$ is more accurate than the other.

As a final quality metric we use a similar standard deviation, but now corresponding to the optical depth. The rationale behind this metric is that the dust density is not the ultimate quantity for which we need the discretisation. In the end, the goal of any radiative transfer problem is to solve for the intensity of the radiation field, and our grid should be optimised so that the refinements follow the changes in this quantity (Steinacker et al. 2013). But this is extremely challenging, as we do not know the radiation field a priori. One quantity that might follow the distribution of the radiation field intensity more closely than the density is the optical depth. We choose a large number of random straight paths through the grid volume, with start and end points distributed uniformly across the dust grid volume. For each path we evaluate the difference between the theoretical optical depth τ_{t} (calculated by numerically integrating the true density along the path) and the grid optical depth τ_{g} (calculated on the grid). Subsequently, we calculate the standard deviation $\Delta\tau$ for the distribution of $\tau_{\text{t}} - \tau_{\text{g}}$. Again, the values of $\Delta\tau$ can differ widely between different models, but it is a useful metric to compare the quality of two grids that correspond to the same model.

3.3.1 Octree grids

An octree is a spatial data structure that recursively partitions a region of space into eight octants (subnodes). Starting from the root node which encompasses the whole system, nodes are recursively subdivided into smaller nodes, which enables the user to automatically increase the spatial resolution where this is necessary. The subdivision continues until some stopping criterion is satisfied (an extensive discussion of stopping criteria can be found in Chapter 5).

We have implemented an octree dust grid structure in the SKIRT code based on a dust mass threshold, in the sense that each dust cell (i.e. each leaf node in the tree) can contain at most a fraction δ_{max} of the total dust mass in the system. The construction of the octree grid is similar as described in Kurosawa and Hillier (2001) and very straightforward: we start from a root node that encloses the entire dusty medium and we add this node to a list of nodes (the root node having number 0). The construction algorithm then loops over this list of nodes and tests whether each node should be subdivided. This implies that we estimate the total dust mass in the node. This is accomplished by generating N_{ran} random positions $\boldsymbol{x}_i$ within the node volume (typically of the order 100) and estimating the dust mass fraction in the node

$$\delta = \frac{V \sum_{i=1}^{N_{\text{ran}}} \rho_i}{M\, N_{\text{ran}}} \tag{3.1}$$

where V is the volume of the node, M is the total mass in the system and $\rho_i = \rho(\boldsymbol{x}_i)$ is the dust density at the position $\boldsymbol{x}_i$. If $\delta < \delta_{\text{max}}$ the subdivision stops and this node is a leaf node and hence an actual dust cell. On the other hand, if $\delta > \delta_{\text{max}}$, we partition the node into eight subnodes and append them at the end of the node list. In either case, we subsequently move to the next node in the node list and repeat the same test. This loop is repeated until the entire list of nodes is finished.

Internally in SKIRT, an octree grid structure essentially consists of this list of nodes, and an additional vector that contains the node IDs of all leaves. This is the final list of dust cells (only the leaf nodes are actual dust cells).

So far, we have not provided any prescription on how a node with $\delta > \delta_{\text{max}}$ should be subdivided. Standard octree algorithms subdivide each node by taking the centre of the node as the subdivision point, such that all eight subnodes of a node have the same size (and in general, all nodes corresponding to the same level of subdivision have exactly the same size). We denote this method as *regular* subdivision (figure 3.2,

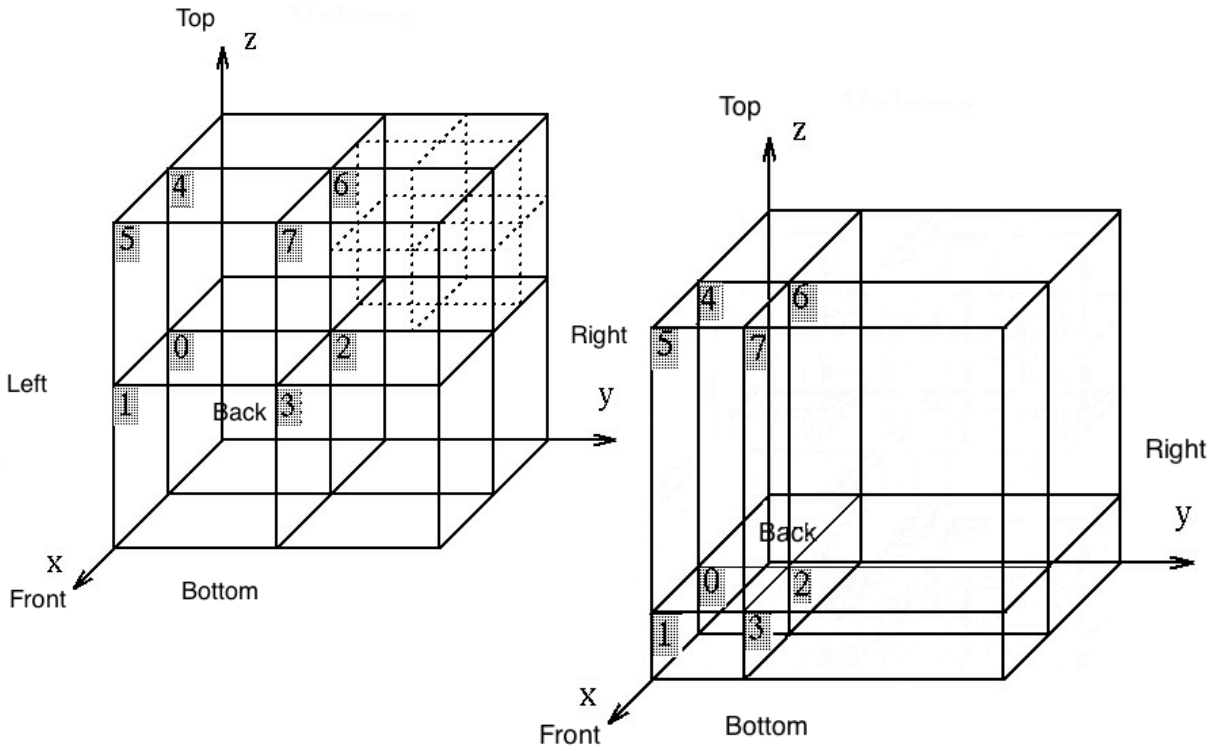

Figure 3.2: An illustration of the regular subdivision (left) and the barycentric subdivision (right) of a node in an octree grid structure. The numbers indicate the localisation of the children within their parent node.

left panel).

One might wonder whether this is the ideal case. The reason why we use octree structures in Monte Carlo radiative transfer is to adapt the size of the dust cells to the local dust mass density; ideally, the mass is distributed more or less evenly among the different dust cells. In a node with a large density gradient, applying a regular subdivision is not necessarily an ideal recipe to achieve this goal. Indeed, assume that most of the mass in a certain node is concentrated towards one of the corners and that the rest of the node has a rather low density. When such a node is subdivided with the geometrical centre as the division point, the corner node will receive virtually all the mass, and will have to be subdivided several times more. An alternative could be to choose the division point of the node such that the mass distribution is roughly equally divided over the eight subnodes. This can be achieved by choosing the barycentre rather than the geometrical centre of the node as the subdivision point. With a *barycentric* subdivision, one would expect that one can zoom in faster on high density regions (figure 3.2, right panel).

One thing to consider is the additional cost that comes with a barycentric octree. A first additional cost is the memory penalty: we have to store the individual dimensions of

every node, rather than just the subdivision level in the case of regular subdivision. This memory penalty is negligible in comparison to the total memory consumption. A second additional cost is the calculation of the barycentre during the octree construction. Fortunately, as we have already determined N_{ran} random points in each node to test for the subdivision criterion, we can easily calculate the barycentre as

$$\boldsymbol{x}_{\text{bary}} = \frac{\sum_{i=1}^{N_{\text{ran}}} \rho_i \, \boldsymbol{x}_i}{\sum_{i=1}^{N_{\text{ran}}} \rho_i}. \tag{3.2}$$

The cost of computing the barycentre is hence negligible compared to the complete simulation run time.

Figure 3.3 illustrates the application of the regular and barycentric octree grid structure for the three different test models.

3.3.2 *k*-d trees

Octrees are widely used in astrophysical codes to hierarchically partition a volume, and it is therefore no wonder that they are also the most popular hierarchical space partitioning structure in radiative transfer codes (e.g., Kurosawa and Hillier 2001; Jonsson 2006; Bianchi 2008; Niccolini and Alcolea 2006). Still it is worth investigating whether octrees are the most suitable hierarchical space for partitioning structures for radiative transfer. In other words, is the systematic subdivision into eight subnodes the best option, despite the straightforward implementation? The subdivision into eight subnodes every time can result in many cells with a mass content that is substantially below the threshold. All of these almost empty cells have to be determined and traversed, which could imply substantial memory and runtime overheads. This problem might be alleviated by using *k*-d trees instead of octrees.

A *k*-d tree is a hierarchical space-partitioning data structure, originally introduced by Bentley (1975). It is a special case of the class of binary space partitioning (BSP) trees, which all partition space by recursively splitting each node in just two subnodes (or children) by means of a hyperplane (a simple plane in 3D space). BSP trees were developed in the late 1970s in the 3D computer graphics community to rapidly access spatial information about objects in a scene for rendering purposes (Fuchs et al. 1979, 1980b), and are now routinely applied in computer-aided geometric design and 3D video games, amongst others. The characteristic property of *k*-d trees is that each node-splitting plane (or hyperplane in the general multidimensional case) is aligned with the axes of the initial cuboidal starting node (the root node). The difference between the octree and a *k*-d tree is that the octree divides a node into eight subnodes using three splitting planes, whereas the *k*-d tree only uses one splitting plane, for more illustra-

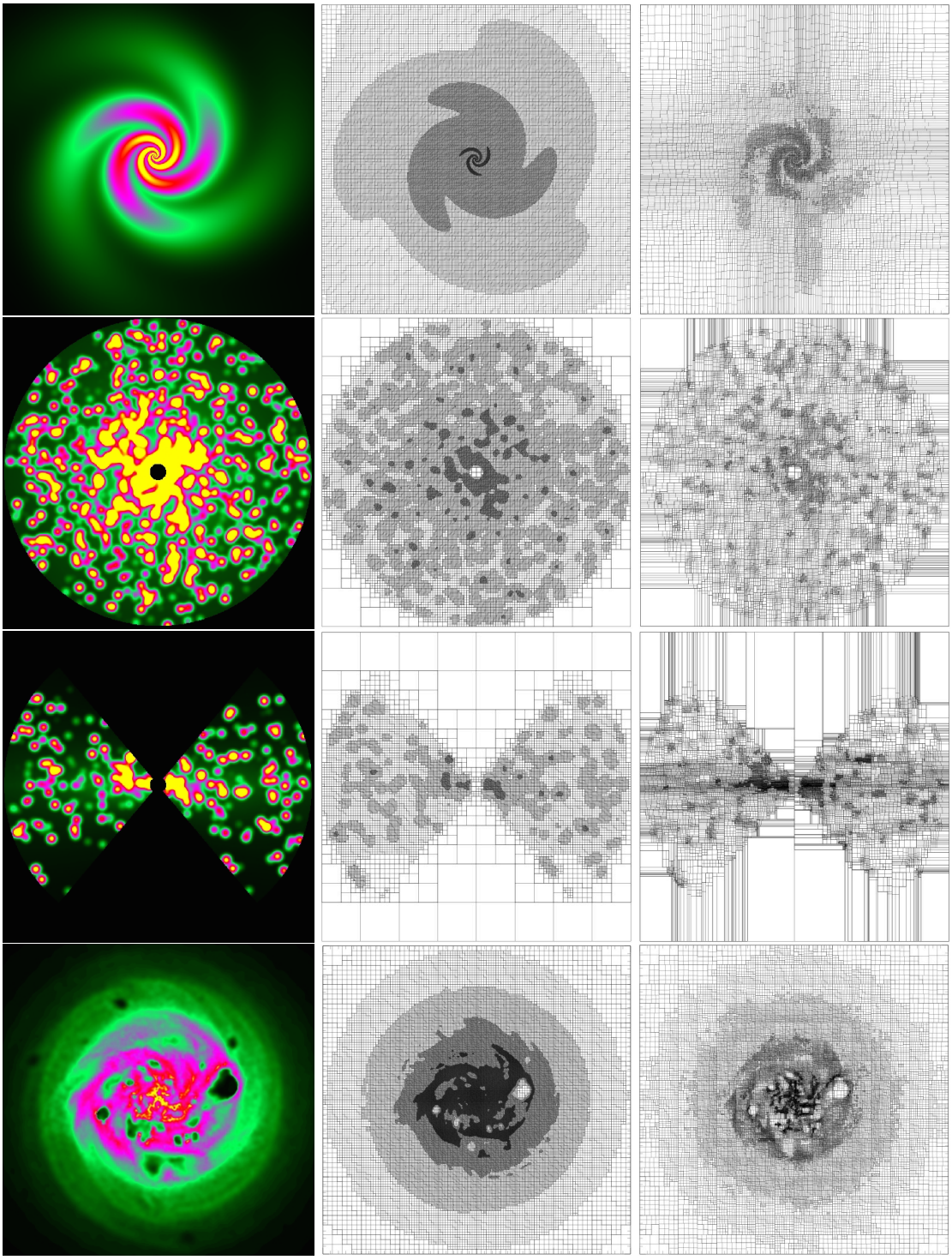

Figure 3.3: Illustration of the use of regular and barycentric octree grid structures for the three test models (see Figure 3.1). On each row, the left column represents a cut through the dust density, and the central and right columns are cuts through the octree grids corresponding to the same planes, and correspond to the regular and barycentric subdivision recipes, respectively. The different shades of grey in the middle and right columns illustrate the density of the cells: darker grey means higher density.

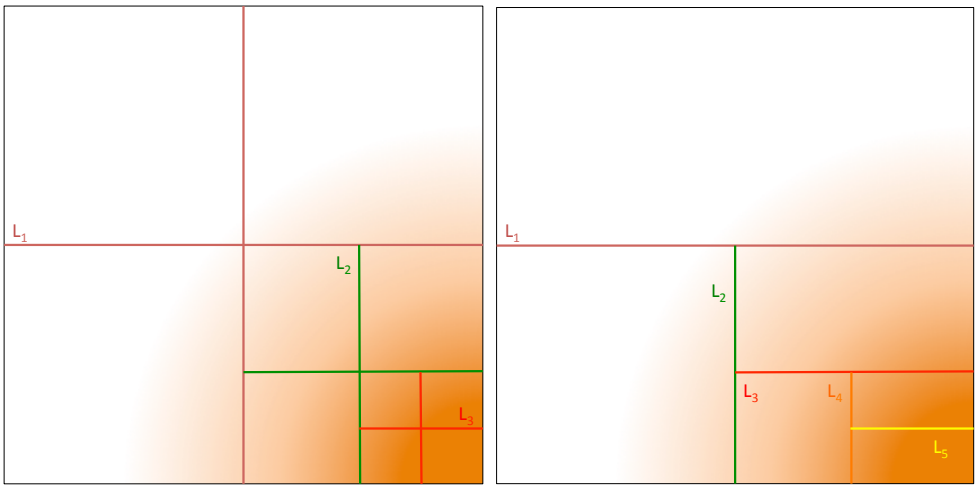

Figure 3.4: 2D Illustration of an octree (left) and *k*-d tree (right). The gradient in the colour indicated the gradient in the density (from strong density in orange to low density in white). L_i indicates the levels of subdivision. We see that the subdivision criterion is satisfied with only 6 cells in the *k*d-tree while it needs 10 cells in the octree.

tion see Figure 3.4. So each octree can in principle be represented as a *k*-d tree in which one level of subdivision in the former is equivalent to three levels of subdivision in the latter. Conversely, not all *k*-d trees can be represented by octrees. Nowadays, *k*-d trees are the most popular space partitioning structure in computer graphics applications (e.g. MacDonald and Booth 1990; Havran 2000; Reshetov et al. 2005; Wald and Havran 2006; Shevtsov et al. 2007; Zhou et al. 2008). To the best of our knowledge, *k*-d trees have not been used in the context of astrophysical radiative transfer simulations.

We have implemented a *k*-d tree dust grid structure in SKIRT. The construction algorithm for the *k*-d tree is completely analogous to the technique we used for the construction of the octree grid structure, as explained in section 3.3.1. The tree is represented as a list of nodes that starts with the cuboidal root node. The construction of the tree consists of a single loop over all nodes in the list. For every node in the list, we test whether it is to be subdivided in two sub-nodes by comparing the ratio δ between dust mass in the node (calculated using a Monte Carlo integration) and the total dust mass in the system to a preset threshold value δ_{max}. If $\delta > \delta_{\text{max}}$, the node is subdivided and the two subnodes are appended to the list. The construction phase ends when the last node of the list is reached, and the actual dust grid consists of all leaf nodes in the list, i.e. all nodes that are not further subdivided.

In the construction of an octree, the subdivision point of each node can in principle be chosen freely, and in Section 3.3.1 we investigated two possible options for this (regular and barycentric subdivision). In a *k*-d tree, there is more freedom, as both the orientation and the location of the splitting plane can be chosen.

Concerning the orientation of the splitting plane, the canonical method of constructing k-d trees uses a cyclic approach, where one cycles through the axes as one moves down the tree. In our 3D case that means that the root node would have a splitting plane perpendicular to the x-axis, its children one perpendicular to the y-axis, its grandchildren one perpendicular to the z-axis, its great-grandchildren one perpendicular to the x-axis, and so on. Another option would be to select the orientation of the splitting plane perpendicular to the axis which has the strongest density gradient in the cell.

Concerning the location of the splitting plane, there are also different options possible. The most obvious option is to use the geometric centre of the node, which results in two subnodes of the equal volume. Another option could be to split the cell such that the two subnodes have equal mass. This option is similar to the barycentric subdivision in octree grids explored by in section 3.3.1, but, contrary to octrees, it is possible to achieve exact equal-mass splitting for k-d trees. A third option is to choose the splitting location such that the two subnodes have equal mean density. This method has shown to give good results in computer graphics ray-shooting simulations (Wald and Havran 2006).

In this section, we compare the qualities of the different grids, using the three test models and the quality metrics introduced in Section 3.2. We start by comparing regular and barycentric octree grids, and subsequently compare octrees and *k*-d trees.

3.4.1 Regular versus barycentric subdivision

Intuitively, one would expect that the barycentric subdivision is more efficient in following the mass distribution. When a node is subdivided with the barycentre as the subdivision point, the mass of the parent node is redistributed more or less equally among the eight child subnodes. This means that the subdivision needs to be repeated less often in the barycentric case compared to the regular case. This is confirmed in Column 4 of Table 3.1, which shows that the average level of a cell in the barycentric grids is about 7.6, whereas it is about 8.6 for the regular grids. It is also graphically illustrated in Figure 3.5, which shows the number of dust cells (i.e. leaf nodes) in each model for each level. In general, the regular grids need higher levels of subdivision compared to the barycentric grids.

Surprisingly at first sight, this does not systematically lead to a smaller total number of cells in the barycentric grids compared to the equivalent regular octree grids (Column 3 of Table 3.1). For the spiral galaxy model, the smoothest of the three test geometries, the barycentric grid contains some 3% fewer cells than the regular grid. For the AGN torus and the SPH galaxy models, with their strong density gradients, the barycentric grids contains more cells than the regular grids, with differences of 11% and 2% respectively.

To understand this, consider a subnode with $\delta = 10\,\delta_{\max}$ and a strong density gradient within the cell. In the barycentric octree, this cell will be subdivided and each of the subnodes will contain approximately $\delta \approx 1.25\,\delta_{\max}$, which means they will all be

Table 3.1: Cells statistics of the different models and grids.

		Number of cells	Average level of each cell
Spiral galaxy	regular	3252264	8.37
	barycentric	3150295	7.45
AGN torus	regular	3050573	7.99
	barycentric	3383906	7.56
SPH galaxy	regular	3315075	9.48
	barycentric	3373280	7.82

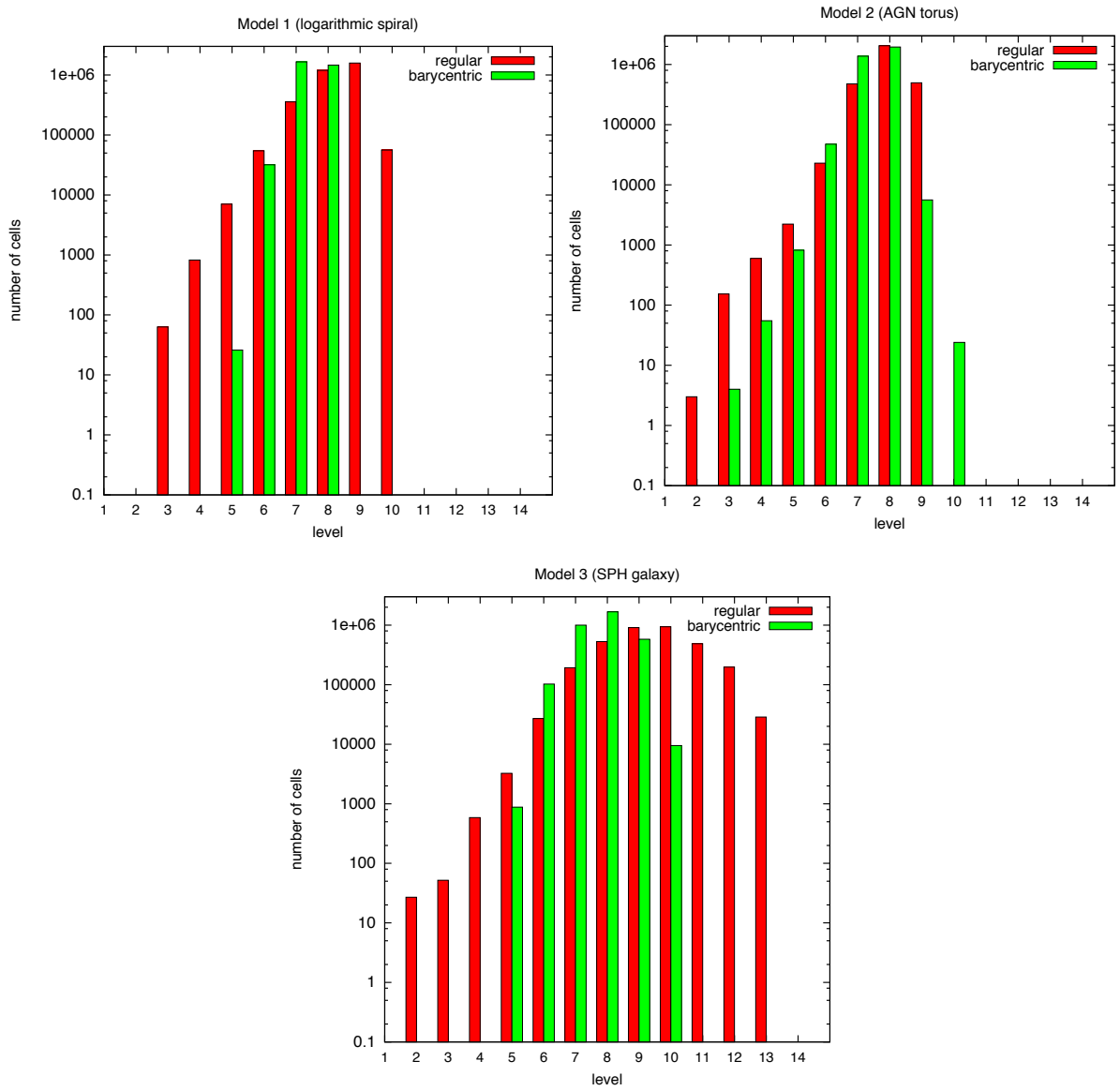

Figure 3.5: Histograms of the total number of cells of each subdivision level for the different models: logarithmic spiral (top left panel), AGN torus (top right panel), and SPH galaxy (bottom panel). The red and green histograms correspond to regular and barycentric octree grids respectively. The average level of the barycentric grid is consistently lower than the average level of the corresponding regular grid. Note the logarithmic scaling of the histograms.

subdivided again, resulting in 64 cells in total. In a regular grid, it is possible that one subnode contains most of the mass and the remaining seven subnodes do not need to be subdivided again. Most probably, several (but not all) of the children of this subnode will have to be subdivided again. This could lead to a set of leaf cells with, on average, a deeper level of subdivision, but the total number of cells could be either smaller or larger, subtly depending on the distribution of the density within the cell.

The previous statistics were obtained by using only one value of $\delta_{\max}$. In Figure 3.6 we

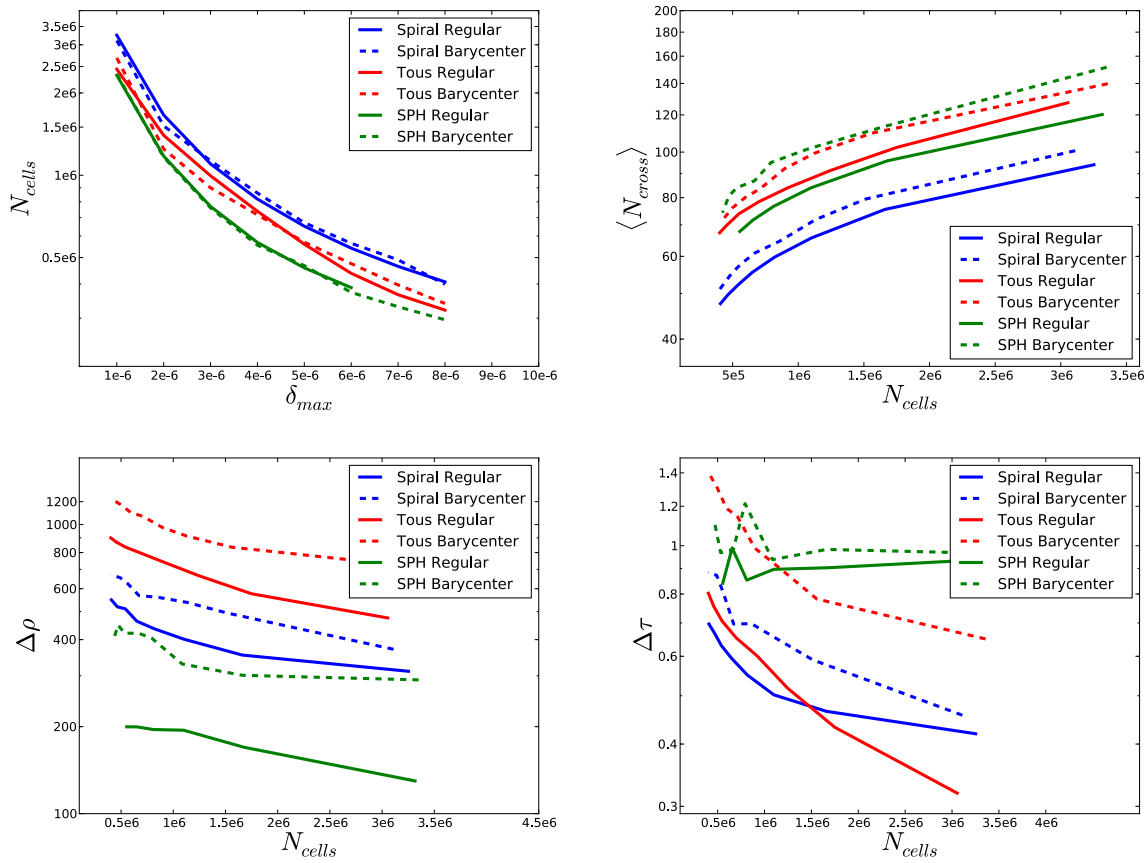

Figure 3.6: Comparison of the grid quality metrics for regular and barycentric octrees of our three test cases (solid lines correspond to regular grids, dashed lines correpond to barycentric grids, and the different colours correspond to the three different test models). The top left panel shows N_{cells}, the total number of cells in the grid, as a function of the threshold mass fraction δ_{max}. The other panels show the average number of cells crossed per path $\langle N_{\text{cross}} \rangle$, the density quality metric $\Delta\rho$, and the optical depth quality metric $\Delta\tau$ as a function of N_{cells}.

repeat the test for a larger sample of δ_{max} values. We check the quality measures of the different subdivision methods (regular versus barycentric) for our three test models to see which one is generating a smaller total number of cells, a smaller number of cells crossed, and lower values of $\Delta\rho$ and $\Delta\tau$.

The top left panel of Figure 3.6 shows N_{cells}, the total number of cells in the grid, as a function of the threshold mass fraction δ_{max}. We can see that for a fixed value of δ_{max}, regular and barycentric grids have more or less the same number of cells irrespective of the chosen model.

In the top right panel of Figure 3.6 we show the average number of cells crossed per path $\langle N_{\text{cross}} \rangle$ as a function of N_{cells}. The regular octree performs impressively better than the barycentric octree for the three test models. It requires fewer cells to be crossed on an average path compared to the barycentric octree. Averaged over the

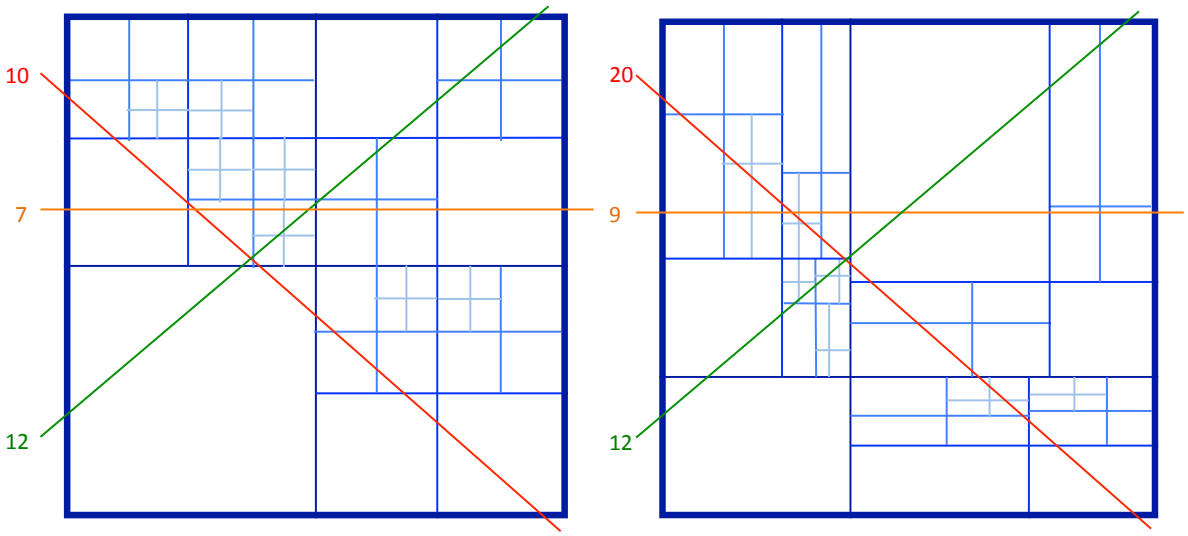

Figure 3.7: 2D illustration of a regular (left) and barycentric quadtree (right). Both have 55 cells and use 4 subdivision levels (shown in different shades of blue). Three random straight paths are drawn (red, orange and green) in each quadtree. It turns out that these paths cross more or equal cells in the barycentric grid than in the regular grid.

three different test models, the mean difference is some 14.3% fewer cells (11% for the spiral galaxy model, 12% for the torus model and 20% for the SPH galaxy model). This makes regular octree grids significantly faster than the barycentric ones in terms of shooting photons. In order to understand this result, we show in Figure 3.7 two quadtrees (regular grid and barycentric grid) which have the same level of subdivision and the same number of cells. We draw three random straight paths in each quadtree. It turns out that the paths cross more or equal cells in the barycentric grid than in the regular grid. The reason for the difference in $\langle N_{\text{cross}} \rangle$ is thus purely geometric.

The smaller values of the average number of cells crossed per path is not the only benefit of the regular grids compared to the barycentric grids. In the bottom panels of Figure 3.6 we compare the discretisation quality metrics $\Delta\rho$ and $\Delta\tau$ for both grids as a function of N_{cells}. For a fixed number of cells, the regular grids typically correspond to lower values of the density quality metric $\Delta\rho$ compared to the barycentric grids, ranging from 25% for the spiral galaxy model to 75% for the SPH galaxy model. Similarly, for a given N_{cells}, regular grids are substantially more accurate in the optical depth quality metric $\Delta\tau$, with differences between both grids ranging from 12% for the SPH galaxy model to 45% for the torus model. The general conclusion is that the regular trees outperform the barycentric trees in all grid quality measures.

As a final remark, we note that these tests presented correspond to the octree grids, but very similar results apply for the k-d tree grid as well. Based on extensive testing of the different options mentioned in Section 3.3.2, we found that the standard combination of cyclic orientation and equal-volume split (which we refer to as regular k-d

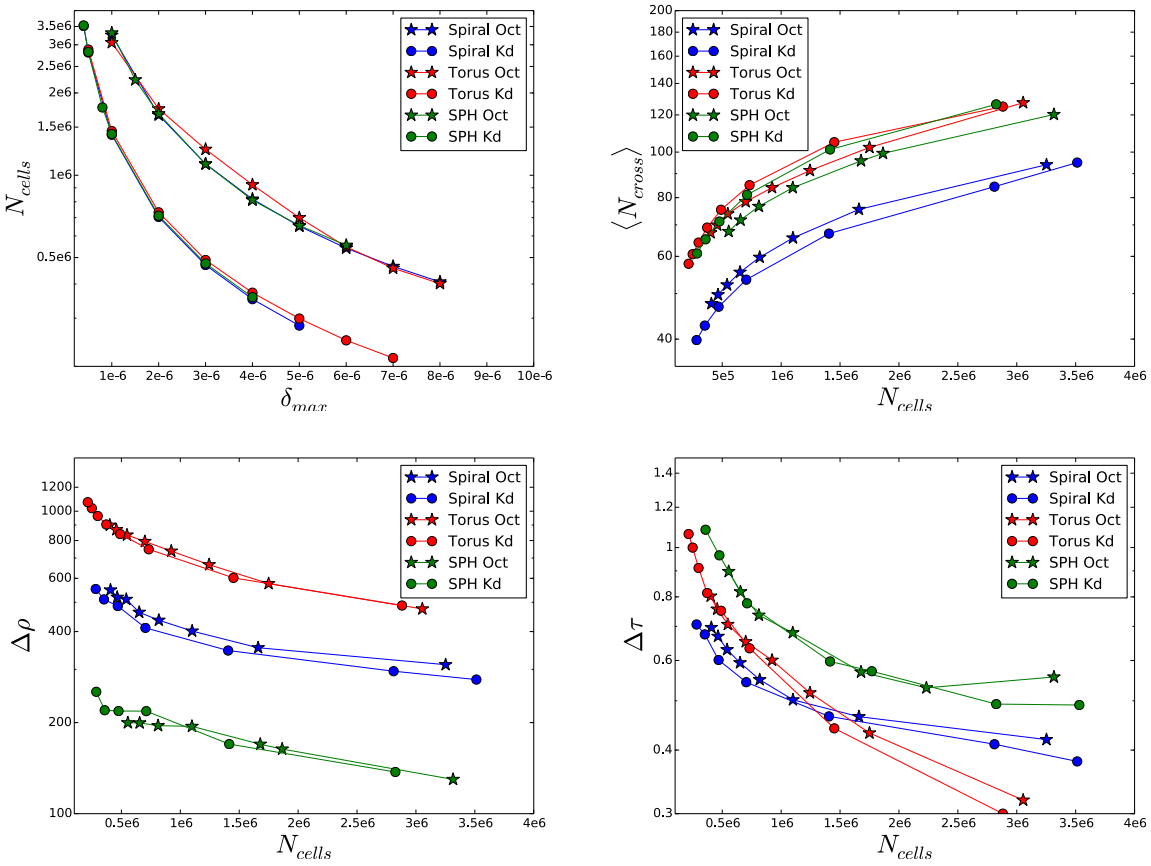

Figure 3.8: Comparison of the grid quality metrics for octree and *k*-d-tree based grids of our three test cases (stars correspond to octree grids, dots to *k*-d tree grids, and the different colours correspond to the three different test models). The top left panel shows N_{cells}, the total number of cells in the grid, as a function of the threshold mass fraction δ_{max}. For a given threshold value, octree grids require up to more than double the number of cells compared to the corresponding *k*-d tree. The other panels show the average number of cells crossed per path $\langle N_{\text{cross}} \rangle$, the density quality metric $\Delta\rho$, and the optical depth quality metric $\Delta\tau$ as a function of N_{cells}.

trees in the remainder of this thesis) is the most suitable option for radiative transfer simulations.

3.4.2 Octrees versus *k*-d trees

In this subsection we compare the qualities of octree and *k*-d tree grids. Given the results of the previous subsection, we concentrate on the regular versions of both grids.

Figure 3.8 shows the results of a comparison of octree and *k*-d tree based SKIRT simulations of our three test cases. The top left panel shows N_{cells}, the total number of cells in the grid, as a function of the threshold mass fraction δ_{max}. Impressively, for a fixed value of δ_{max}, the *k*-d tree generates only half as many cells as the octree, irrespective

of the chosen model. This alone already strongly advocates for the use of k-d trees in radiative transfer simulations.

In the top right panel of Figure 3.8 we show the average number of cells crossed per path. If we would have plotted this quantity as a function of the threshold mass fraction $\delta_{\max}$, the k-d tree would easily beat the octree grid, as the former contains only half the number of cells of the latter. If we plot $\langle N_{\text{cross}} \rangle$ as a function of N_{cells}, the picture is more mixed: the k-d tree performs slightly better than the octree for the logarithmic spiral galaxy model, but slightly worse for the other two models. Averaging out, we find that the average straight path through the k-d tree crosses roughly the same number of cells as the average path through the octree with the same total number of cells (with a more relaxed value of $\delta_{\max}$).

Looking at the quality of the grids, we find that, for a fixed $\delta_{\max}$, the octree grids have a more accurate discretisation than the corresponding k-d trees. This is no surprise, as they contain up to double as many cells. On the other hand, if we compare the quality of the octree and k-d tree grids for fixed values of N_{cells} (bottom panels of Figure 3.8), the results turn around: for a fixed number of cells, the k-d tree grids typically correspond to lower values of $\Delta\rho$ and $\Delta\tau$ compared to the octree grids. This means that, for a certain required density or optical depth grid quality, we can generate a k-d tree with roughly 20% fewer cells compared to an octree grid.

The general conclusion is that the k-d tree based grids outperform the octree grids in all grid quality measures. As they are as simple to implement as the more widely used octree grids, we recommend their use in radiative transfer codes.

3.5 Discussion and conclusions

In this Chapter, we have critically investigated the use of hierarchical octree and *k*-d tree grids to partition a dusty medium in the frame of 3D dust radiative transfer codes. Octree and *k*-d tree grids can refine the gridding in higher density regions without the need to create undesirable dust cells in low density regions. We have implemented flexible octree and *k*-d tree structures in SKIRT, which allows for either a regular or a barycentric iterative subdivision of the cells.

Our first important conclusion is that barycentric grids are less efficient than the corresponding regular grids in all cases, even for simulations in which the regular grid contains more grid cells. To explain this perhaps unexpected result, we investigated the characteristics of both grid types. The barycentric grids have grid cells with, on average, a lower level, i.e. we need fewer successive grid subdivisions to meet the same mass resolution. But this does not necessarily imply that the total number of grid cells is lower in the barycentric grids; this depends on the geometry of the model. The regular grids are also more accurate in their discretisation, and they are faster in shooting photons because, on average, fewer cells need to be crossed per path.

Secondly, we have investigated the use of hierarchical *k*-d tree grids as an alternative to octree grids in partitioning the dusty medium. Using the three different test models, and a set the grid quality metrics, we have critically compared the octree and *k*-d based grids. We have found that, for a fixed value of the mass threshold δ_{max}, the *k*-d tree generates only half as many cells as the octree, irrespective of the chosen model. Moreover, if we compare the quality of the octree and *k*-d tree grids for a fixed total number of cells, the latter have a higher accuracy. We can generate a *k*-d tree with roughly 20% fewer cells compared to an octree grid for a certain required density or optical depth quality.

Based on the above, we recommend the regular subdivision for octrees and *k*-d trees in the frame of 3D radiative transfer simulations, and we strongly advocate the use of the lesser-known *k*-d trees as an alternative to the popular octrees.

Grid traversal in hierarchical grids

4

The material presented in this Chapter is original work; it is published in a condensed form in Saftly et al. (2013).

4.1 Introduction

In Monte Carlo radiative transfer simulations we follow millions of photon packages as they are scattered, absorbed, and re-emitted within the interstellar medium. The life cycle of every photon package implies the calculation of several random straight paths through the dust grid (depending on the optical depth of the system and the kind of simulation, this can vary from one to tens of paths per photon package). The calculation of a straight path essentially comes down to calculating the ordered list of dust cells that the path intersects, and the physical distance covered in each individual cell (see Figure 4.1). If this information is known, we can calculate the optical depth along the path and translate a given covered optical depth to a physical path length. The calculation of the path of each individual photon package through the dusty medium is often the most time-consuming aspect of a 3D Monte Carlo radiative transfer simulation. Therefore it is crucial to make the propagation of the photons as efficient as possible.

The grid traversal is a loop that consists of a repetition of two simple steps. The first step is to determine in which cell the position $\boldsymbol{x}$ is located, and the next step is to move $\boldsymbol{x}$ to the boundary of the cell while recording the covered distance. This sequence is repeated until the path crosses the outer boundary of the grid. In a cartesian grid structure, both steps are very straightforward. The cell that contains the initial position is found immediately by bracketing the individual x, y and z coordinates of the position $\boldsymbol{x}$. Given the propagation direction, the intersection with the different walls of the cell can be calculated directly, and the first wall that will be hit determines the exit point from the cell and hence the new position. The distance covered between these two points is trivial to compute and the index of the next cell is found by just moving up or down one index in the x, y or z array, depending on which wall is hit first. The loop can then be repeated.

In the previous Chapter we have introduced two kinds of hierarchical grids that we have implemented in SKIRT to efficiently partition a dusty medium with an arbitrary 3D density distribution. In an octree or a k-d tree grid structure, one can use exactly the same procedure to determine which wall will be hit first, and to calculate the distance between the initial position and the exit point. The more difficult step is identifying the next cell that the path will cross. Indeed, as the cells in octrees and k-d trees are hierarchically ordered, it is not sufficient to just increase or decrease an index as in the case of a cartesian grid structure. Most Monte Carlo codes that use octree grids, use a simple top-down method to traverse the grid (unfortunately, the details of grid traversal are not explicitly given for several codes). The traversal of rays through hierarchical

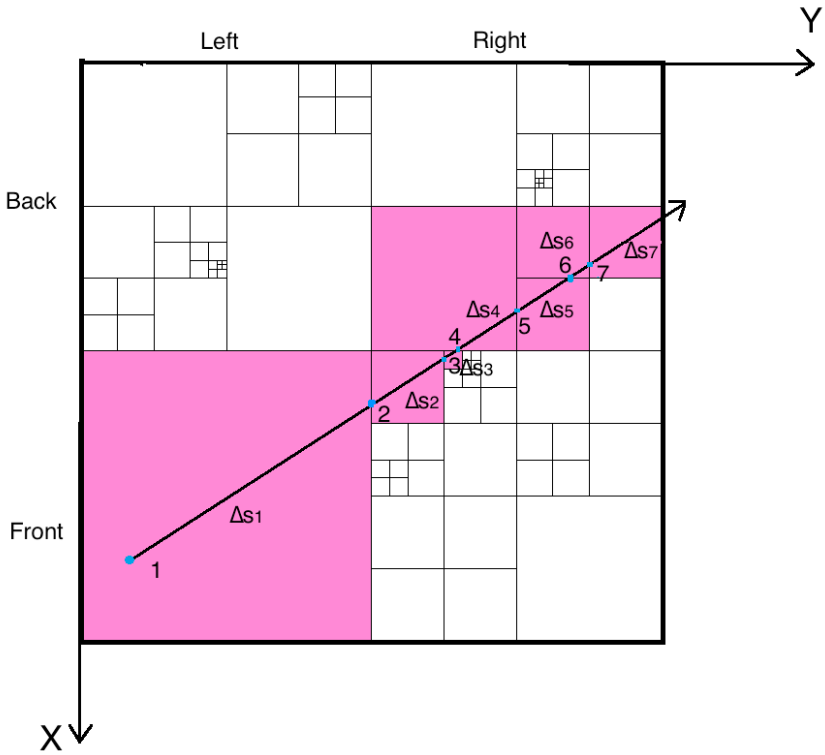

Figure 4.1: The calculation of a random path through an octree grid (here we show the 2D quadtree analogue). The information needed in a Monte Carlo simulation is an ordered list of cells crossed by the straight path defined by the starting location $\boldsymbol{x}$ and the propagation direction $\boldsymbol{k}$, as well as the physical path length Δs covered within each cell along the path.

trees has been a source of discussion in the computer graphics literature, and different traversal algorithms have been developed (e.g. Glassner 1984; Amanatides and Woo 1987; Samet 1989, 1990; Agate et al. 1991; Revelles et al. 2000; Frisken and Perry 2002). It remains to be investigated whether these might be more efficient in the context of radiative transfer simulations.

The goal of this Chapter is to compare how different grid traversal methods perform in the context of realistic Monte Carlo radiative transfer simulations. Loosely based on the methods used in the computer graphics community, we have implemented three different methods in SKIRT (the top-down method, the neighbour list search method, and the bookkeeping method). These are presented in Section 4.2. In Section 4.3 we test these methods on both regular and barycentric octree grids, constructed for the same three test models as considered in the previous Chapter. The results are summarised in Section 4.4.

4.2.1 The top-down method

The most straightforward method to traverse an octree or a *k*-d tree grid is a top-down method (Glassner 1984). The idea of this method is simple: once a photon package crosses the boundary of a cell and we have determined the new position (which is now in a yet unidentified cell), we start from the root node and descend down the tree. For every node along the tree, we determine in which of its subnodes the new position is located. This loop ends when the node is a leaf node, i.e. an actual dust cell. The method is illustrated in Figure 4.2, where we show the traversal of a photon package through a quadtree. The path starts at the bottom-left, and the task is to find the next cell after the path has crossed the first cell (the bottom-left cell). The method iteratively descends the tree from the root node (top panel) and moves down one level in every step until the node is a leaf node (i.e. an actual dust cell), which takes 4 levels in this particular case. The same thing is applied in *k*-d tree algorithms. As a *k*-d tree subdivides each node into two instead of eight subnodes, the depth of a *k*-d tree is typically a factor three higher than the depth of the corresponding octree. The number of operations to descend a *k*-d tree is, however, roughly equal in both cases, as one test only needs to be done per level in the *k*-d tree, compared to three tests in the octree.

This top-down method is very easy to implement, and it does not depend on whether the subdivision is regular or barycentric. This algorithm is implemented in most Monte Carlo radiative transfer codes (e.g. Kurosawa and Hillier 2001; Bianchi 2008).

4.2.2 The neighbour list method

An alternative method of traversing an octree or a *k*-d tree makes use of a list of the neighbouring cells of each node. This method was first advocated by Samet (1989, 1990) in the frame of computer graphics ray-tracing. Instead of blindly looking for the cell that contains the position of the photon package once it has traversed a cell wall, we make use of the fact that the yet unknown cell is a neighbour of the previous dust cell. If we hence construct our octree such that all cells have pointers to their neighbours stored, finding the next cell is limited to searching among the possible neighbours.

We have implemented in our octree and *k*-d tree dust grids in SKIRT the possibility to store pointers to all the neighbours of each grid cell. In particular, every dust cell contains six different lists with pointers to the neighbouring cells, corresponding to

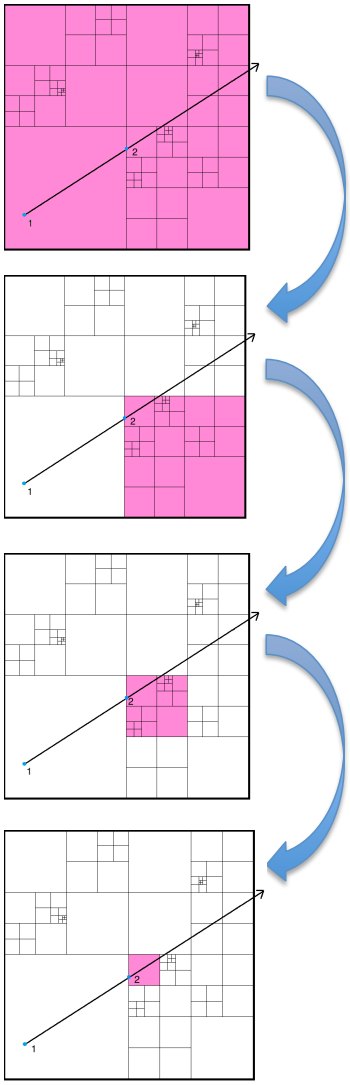

Figure 4.2: Illustration of the top-down method of traversing a 2D quadtree. See Section 4.2.1 for details.

the six different walls of the cell (back, front, left, right, bottom and top). If we know through which wall the photon package is escaping the cell, we just have to search the corresponding list of cells. This search is just a simple loop over the list of neighbour cells. The cells in the neighbour list are ordered by decreasing area of overlap, so we start checking from the cell with the biggest common area with the current cell. This loop is stopped as soon as we find the correct cell, as illustrated in Figure 4.3 in a quadtree analogue. In this case, the cell has six dust cells as neighbours on its right-hand side. They are checked one by one, in the order of the overlapping border length. In this case, the third cell in the list is the correct one, and the loop is stopped.

This algorithm is straightforward and simple to implement, and again is applicable both to regular and barycentric grids. The additional memory usage of this method is

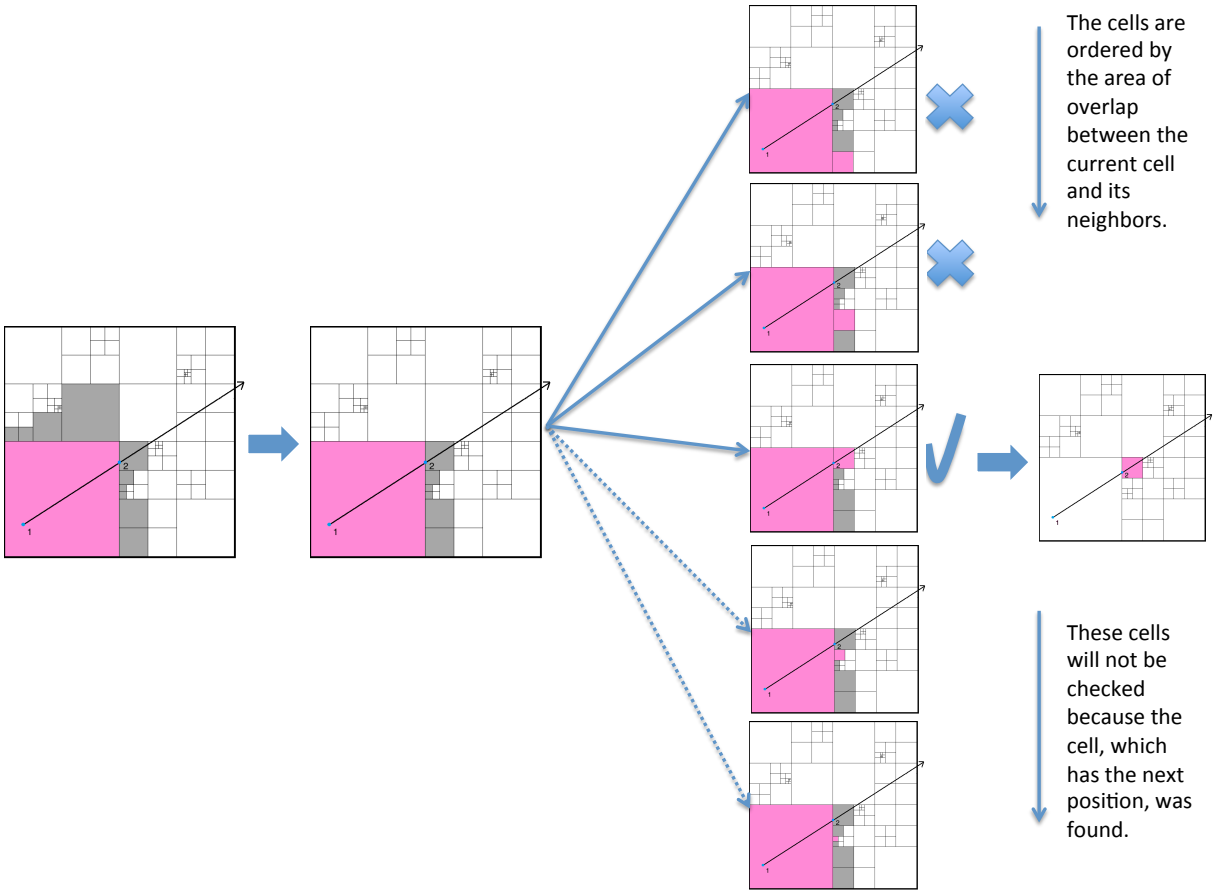

Figure 4.3: Illustration of the neighbour list method of traversing 2D quadtree. See Section 4.2.2 for details.

modest: it just implies that six lists of pointers need to be stored for each cell, which is typically negligible compared to the amount of data that is stored in each cell in a Monte Carlo simulation (e.g. the properties of dust and the strength of the radiation field at a large number of wavelengths).

The main complication of the neighbour list search method is that the neighbour lists of all cells need to be computed. Determining the neighbouring cells for the N cells in an arbitrary dust grid could be an N^2 problem if performed without proper care. Fortunately in the case of a hierarchical tree grid it is easy to build the neighbour lists in $N \log N$ time during the construction of the tree (in fact, proportional to the number of nodes in the tree, including non-leaf nodes). The trick is to adjust the neighbour lists each time a node is being subdivided.

Each node in an octree or a k-d tree is equipped with six neighbour lists, one for each wall. When a new node is freshly created, these lists are initially empty. Clearly the root node has no neighbours (because by definition it encompasses the complete dust domain) so its neighbour lists remain empty. Whenever a node is being subdivided

(starting with the root node and continued recursively), the neighbour lists for the newly created children and for the immediately surrounding nodes are adjusted as described below. As a result the neighbour lists remain up to date at all times during the grid construction.

A first obvious requirement is to setup the *internal neighbours* for the subdivided node. In an octree, each of the eight newly created children has three neighbours among its siblings, while in a *k*-d tree, each children has only one internal neighbour. Adding these internal neighbours is straightforward.

The remaining and slightly more complicated task is to push the neighbours of the subdivided node to the child nodes. Since the subdivided node becomes a non-leaf node, its own neighbour lists will no longer be used and must be replaced by the appropriate entries in its children's neighbour lists (only the actual dust cells represented by octree leaf cells are used for calculating photon paths). This task can be achieved by performing the following steps consecutively for each neighbour (hereafter called the target node) of the subdivided node: (1) remove the subdivided node from the target node's neighbour list, and vice versa; (2) add the target node to the neighbour list of any newly created children that share a wall and nonzero area overlap with the target node, and vice versa. Note that a particular target node may overlap with and thus be inherited by multiple children. When implementing these steps, it is practical to provide a separate loop for each of the 6 walls rather than trying to combine everything in a single loop.

Sorting the neighbours in each neighbour list by decreasing area of overlap can be done most effectively in a separate pass over the cells after the octree has been fully constructed, so that the geometry no longer changes.

4.2.3 The bookkeeping method

Finally, we explored a third method of traversing a tree grid that is inspired by the work of Frisken and Perry (2002) and which we denote as the bookkeeping method. One of the drawbacks of the top-down method is that, for every passage through a wall, the search for the new cell has to start from the root node. This is unfortunate, as we often know in which branch of the tree the next position will be: indeed each node in the octree or a *k*-d tree has a place-awareness, i.e. the knowledge of its position as a subnode with respect to its sibling nodes (e.g. the front-right-top subnode in an octree, the back subnode in a *k*-d tree). This place awareness is easily computed as nodes are always added to the tree in sets of eight in octrees or two in *k*-d trees. All nodes with the same place awareness hence have the same index modulo in the list of nodes in the tree.

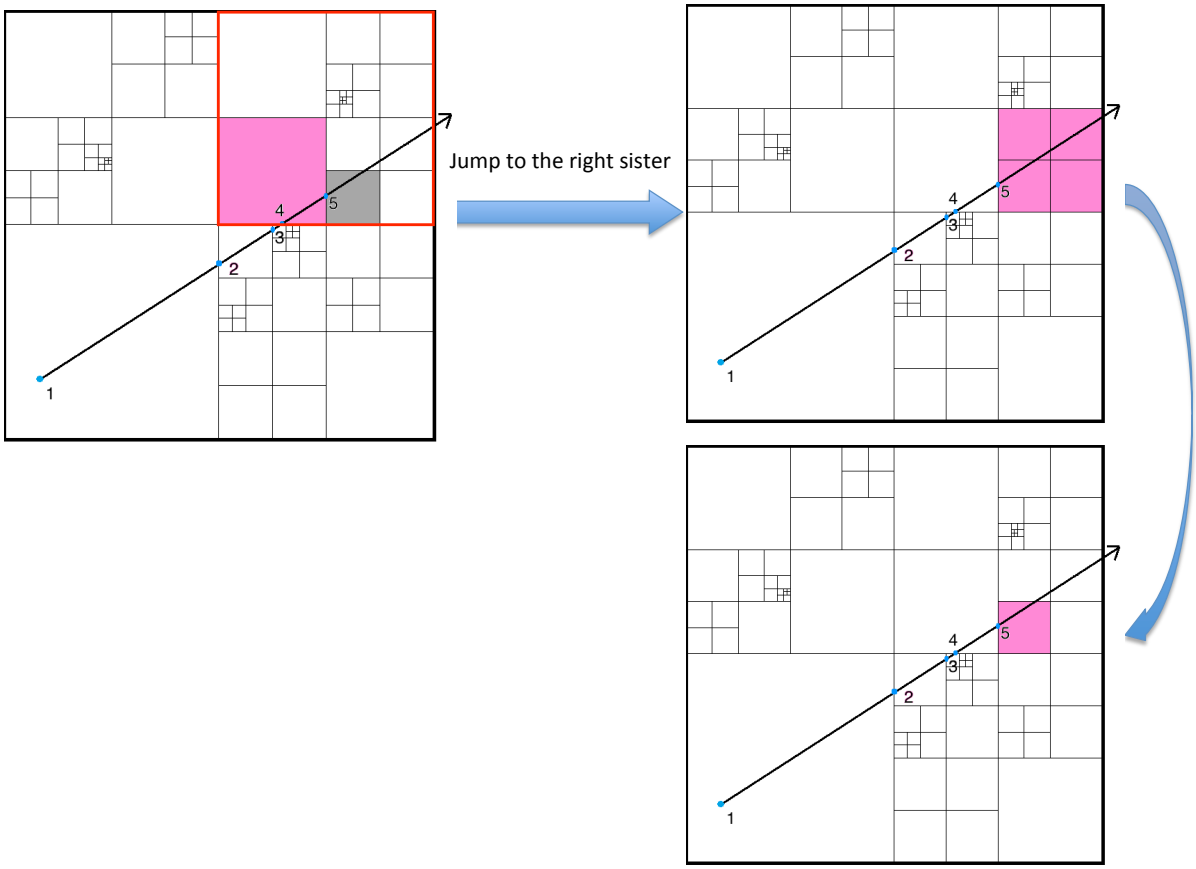

Figure 4.4: Illustration of the bookkeeping method of traversing a quadtree (internal transition). See Section 4.2.3 for details.

This place awareness can be used to determine the next cell. Consider the situation depicted in Figure 4.4. The photon package leaves the pink cell to the next cell which is in grey through the right edge and our task is to find out the identity of the grey cell. This original cell is aware that it is the bottom-left subnode of its parent (surrounded by the red line). As the photon package leaves the cell through the right edge, we know that the next cell will be either the bottom-right node of the same branch (in this case the bottom-right node of the red node) or one of its subnodes. The search can hence start from this node, which requires in this case one step down to find the cell, rather than from the root node as in the case of the simple top-down method presented in Section 4.2.1.

A slightly more difficult case occurs when the transition through a wall is not an internal transition, e.g. the photon package in Figure 4.5 passes through the ceiling of the pink node which is one of the top subnodes of its parent node. The next cell (in grey is not a sibling node. In this case, one option could be to start the search then from the root node as in the standard top-down method. An alternative, which we have

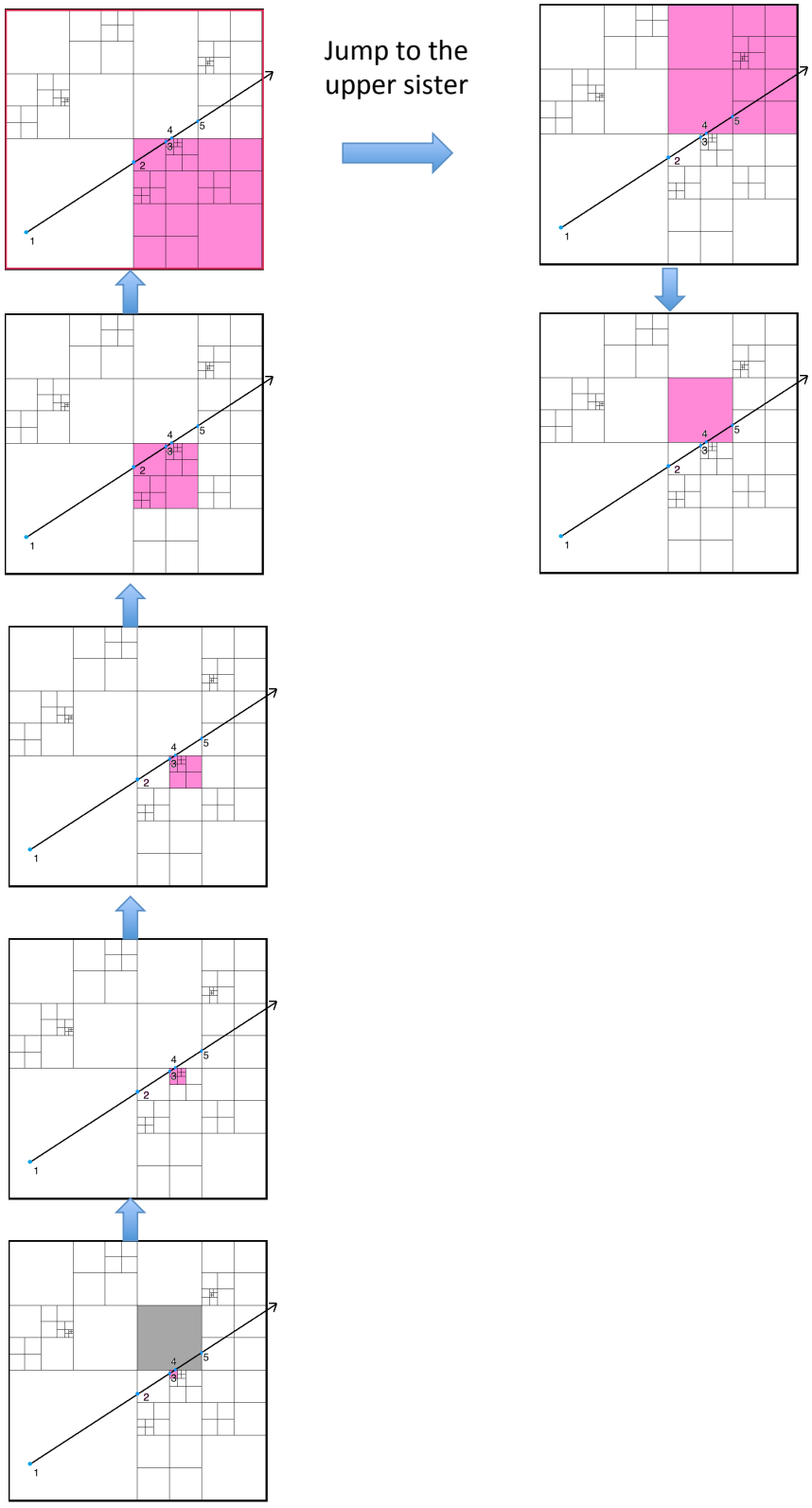

Figure 4.5: Illustration of the bookkeeping method of traversing a quadtree (external transition). See Section 4.2.3 for details.

implemented, is to iteratively go up the tree starting from the current node until the transition is an internal transition. In our example of a passage through the ceiling of a cell, we go up the tree four times until the node is on the bottom row of the father node (it is the bottom-right node of the red node). We then determine the sibling node that is directly on top of it and then iteratively descend the tree until the node is a leaf node, which is only one step in this case.

Of the three methods presented, this method is the most complex in terms of implementation. However, it is still very manageable, it implies no memory overhead or additional computations, and it is, again, applicable to regular as well as barycentric grids.

4.3.1 Timings

The main goal of this Chapter is to find the most efficient way to traverse complex hierarchical grids, in the sense that the time spent for photon packages traversing the dusty medium during the Monte Carlo simulation is minimised. We tested the efficiency by doing accurate timings of the Monte Carlo routine, for each of the 18 models in our test suite (i.e. for the three geometries, the two grid subdivision methods, and the three grid traversal algorithms). Note that we have done the testings for octree grids in this Chapter, but the methods and results are equally applicable to *k*-d trees.

Obtaining precise and repeatable timings to compare the efficiency of alternate methods is trickier than it might seem. The uncertainty introduced by executing multiple threads in parallel – with its inherent randomness and resource contention – is easily avoided by using only a single thread. However modern hardware further complicates matters. Some desktop computers lower the processor's clock rate when the chip warms up, substantially decreasing performance after a certain time of sustained computation. On larger multi-processor systems performance often depends on where data structures are allocated in main memory relative to the processing core that happens to execute the program. To alleviate these issues we performed our timing tests on a slightly older server installed in a temperature-controlled room. The simulations were run one after the other in a single execution thread, and nothing else was happening on the computer. Numbering the 18 tests from 1 to 18, we ran the sequence 1–18, 1–18, 18–1. The timing variations between the three runs turned out to be less than 2 seconds for each simulation, well below the differences between the various methods.

Octree construction times are not considered in these timing tests, as this needs to be done only once for each simulation, the octree construction time is a few minutes at most (depending on the complexity of the dust density field), whereas a typical full-scale radiative transfer simulation can last several hours. In other applications where the efficiency of the octree construction is important, more advanced tree construction algorithms can be applied (Sundar et al. 2008; Burstedde et al. 2011).

The average run times for each of the different runs can be found in the top three rows of Table 4.1. Ignoring intricacies such as loop overhead, the run time of each simulation can schematically be written as

$$t_{\text{run}} = N_{\text{pp}} \langle N_{\text{path}} \rangle \left[\langle t_{\text{launch}} \rangle + \langle N_{\text{cross}} \rangle \Big(\langle t_{\text{id}} \rangle + \langle t_{\text{cross}} \rangle \Big) \right] \tag{4.1}$$

where N_{pp} is the total number of photon packages in the simulation, $\langle N_{\text{path}} \rangle$ is the average number of random straight paths in a photon package, $\langle t_{\text{launch}} \rangle$ is the average time needed to generate the starting location and orientation of a path[1], $\langle N_{\text{cross}} \rangle$ is the average number of cells crossed by a path, $\langle t_{\text{id}} \rangle$ is the average time necessary to identify the next cell along the path, and $\langle t_{\text{cross}} \rangle$ is the average time necessary to cross this cell (i.e. find the exit point and the covered path length within the cell). Of these six factors, N_{pp} and $\langle t_{\text{cross}} \rangle$ are identical for all runs, and $\langle N_{\text{path}} \rangle$ and $\langle t_{\text{launch}} \rangle$ are similar for all runs corresponding to a given test model. Furthermore, $\langle t_{\text{launch}} \rangle$ is expected to be small compared to the grid traversal[2]. For a fixed geometry, the differences in run time are hence only due to differences in $\langle N_{\text{cross}} \rangle$ and $\langle t_{\text{id}} \rangle$, where the former depends only on the grid subdivision method (regular or barycentric), and the latter depends on both the grid subdivision method and the grid traversal method.

4.3.2 Results

The first clear result that we find from a comparison of the run times listed in Table 4.1, is that for all simulations in our suite, the neighbour list algorithm is the fastest method to traverse photon packages through the dust grid. It is faster than the other two methods, which are almost equally efficient, by about 20%. For the neighbour list method, $\langle t_{\text{id}} \rangle$ is proportional to the number of neighbouring dust cells that needs to be tested every time a cell is crossed. In this respect, it is important to make the distinction between the average number of neighbours of each cell wall (row 9 in Table 4.1), the average number of neighbours of every wall crossed (row 10) and the number of neighbours that need to be tested for each crossing (row 11). These statistics turn out to be substantially different, because some cells are crossed more often than others and because neighbouring cells with the largest overlap area are tested first in the neighbour search algorithm. The ordering of the neighbour list by overlapping surface area makes the neighbour list algorithm extremely efficient.

Another remarkable result is that simulations with a barycentric grid are *always* slower than the corresponding simulations with a regular grid, even if the number of cells in the barycentric grid is smaller than in the regular grid. We obtained a similar result when we compared the quality measures of regular and barycentric grids in Section 3.4.2. As demonstrated there, regular grids generate fewer crossed cells than the

[1] After an emission event, the position is generated randomly according to the source distribution, and the orientation is typically chosen randomly from the unit sphere, although this is not mandatory (e.g. Juvela 2005; Niccolini et al. 2003; Stalevski et al. 2012). After a scattering event, the starting location is already known, and the orientation needs to be chosen randomly according to the scattering phase function (e.g. Witt 1977).

[2] In separate timing experiments, we confirmed that roughly 75% of the simulation run time is spent in performing grid traversal.

corresponding barycentric grids, which makes the regular grid more efficient in shooting photons. Row 8 in Table 4.1 shows that the average number of cells crossed per path $\langle N_{\text{cross}} \rangle$ is indeed systematically larger for the barycentric octrees compared to the corresponding regular octrees. This quantity also makes the top-down and the bookkeeping methods slower in barycentric grids than in the regular ones. Consider, for example, the top-down method, where $\langle t_{\text{id}} \rangle$ is proportional to the average level of every cell crossed. As the average level of each cell in a barycentric grid is lower than in a regular grid (Rows 5 and 6 in Table 4.1), one would expect the barycentric grid to be more efficient than the regular grid, but this not the case and the opposite is true. The reason for the difference in $\langle N_{\text{cross}} \rangle$ (and so in efficiency) is geometrical in nature. By construction, barycentric grids are more irregular in structure, with more neighbours per cell wall. In a regular grid, every cell has, on average, only 1.03 neighbours per wall, whereas the barycentric grid cells have, on average, 1.86 neighbours per wall. Having more neighbours and a more irregular distribution also leads to shorter paths crossed per cell and so more cells along each path.

	Spiral galaxy		AGN torus		SPH galaxy	
	regular	barycentric	regular	barycentric	regular	barycentric
Top-down run time (s)	878	975	1171	1350	1142	1322
Neighbour list run time (s)	713	800	938	1104	897	1082
Bookkeeping run time (s)	893	1006	1168	1374	1117	1351
Number of cells	3252264	3150295	3050573	3383906	3315075	3373280
Average level of each cell	8.37	7.45	7.99	7.56	9.48	7.82
Average level of each cell crossed	7.84	7.29	7.67	7.19	8.84	7.38
Average number of paths per photon package	3.69	3.70	1.85	1.99	3.76	3.76
Average number of cells crossed per path	94.8	102.5	126.9	139.7	124.8	150.3
Average number of neighbours per wall	1.02	1.87	1.06	1.85	1.03	1.87
Average number of neighbours per wall crossed	1.01	1.95	1.22	2.15	1.07	2.04
Average number of neighbours tested per wall crossed	1.01	1.14	1.10	1.20	1.03	1.17

Table 4.1: Statistics of the different models and grids.

4.4 Discussion and conclusions

In this Chapter we implemented and tested three traversal methods for hierarchical trees (the top-down method, the neighbour list search method, and the bookkeeping method). We ran simulations on three representative astrophysical models to test the efficiency of the node's construction types (regular or barycentric) and the traversal methods in typical research circumstances.

As a first result, we found that the neighbour list method is consistently the most efficient method to calculate paths through an octree. With this method, the total simulation run time is about 20% shorter than with the two other methods, which are roughly equally efficient. The efficiency of the neighbour list method is illustrated by the fact that the correct neighbour is almost always found as the first item in the list. This is achieved in part by ordering the neighbour lists according to decreasing overlap area. The neighbour list method implies an overhead both in memory and processor time, as the neighbours of each cell wall need to be determined, ordered and stored. However the memory overhead is negligible compared to the other information stored for each cell, and the neighbour lists must be created only once at the start of the simulation. One caveat of this method is that this method cannot be used to locate the first cell along a path, i.e. find the cell that corresponds to a new emission event. This operation needs to be done using top-down search.

As a second result, we find that simulations on barycentric grids are *always* slower than simulations on the corresponding regular grids, irrespective of the grid traversal method. This is even the case for geometries in which the barycentric grid has fewer grid cells than the regular grid . The main reason for this is that, in a barycentric grid, the average number of grid cells crossed by a photon package is significantly larger than in the corresponding regular grid, which makes the barycentric grids slower for grid traversal. The reason for this is purely geometric.

Based on the above, we conclude that the most efficient grid for Monte Carlo radiative transfer simulations is regular grids with neighbour list traversal method.

5 Subdivision stopping criteria for hierarchical grids

The material presented in this Chapter is original work; it is published in a condensed form in Saftly et al. (2014).

5.1 Introduction

In Chapter 3 we have introduced hierarchical octrees and *k*-d trees in the SKIRT Monte Carlo code. One important issue that we have not yet considered in detail is the stopping criterion used for construction of the grids. In broad lines, two different schemes are being applied for octree grids in Monte Carlo radiative transfer simulations. Either, a criterion is implied on the distribution of optical depth or dust mass in each node: if the amount of dust in a node is larger than a preset threshold value, the node is recursively subdivided in eight identical subnodes (Kurosawa and Hillier 2001; Wolf 2003; Harries et al. 2004; Bianchi 2008). A variation on this strategy was implemented by Niccolini and Alcolea (2006), who base their criterion on the absorption rate rather than the dust mass density. The second way of building an octree structure is specifically tuned to Monte Carlo simulations designed to work jointly with smoothed particle hydrodynamics (SPH) codes. In this case, the dusty medium is defined by a set of gas/dust particles, and the dust density field is calculated by interpolating the density of the different particles. For such simulations, an efficient way of building an octree structure is a recursive subdivision that continues until each node contains one particle and/or until the size of each node is smaller than the smallest particle smoothing length in the model (Harries et al. 2004; Jonsson 2006).

Ideally, the spatial dust grid used in radiative transfer simulations should be optimised to discretise the intensity of the radiation field, the fundamental quantity that is the objective of radiative transfer studies. Obviously, this quantity is not known at the beginning of a radiative transfer simulation, which makes the task to set up the grid hard: the challenge is to construct the best possible grid without a priori knowledge of the radiation field. The most obvious choice is to base the grid on the dust density field, but the question still remains on which criterion we should base the discretisation.

In the previous Chapters, we used grids based on a simple criterion that continues the subdivision of each node until it contains a dust mass smaller than some preset threshold value. While this criterion is intuitive, simple and straightforward to implement, it has a number of potential drawbacks. It cannot make a distinction between large cells with a low density and tiny cells with a high density, while this distinction should be made if we want to concentrate the subdivision of the cells in regions with high optical depth. In addition, such a criterion has difficulty with strong density gradients and sharp edges: it stops the subdivision of nodes with large gradients or sharp edges relatively quickly, whereas a high spatial resolution is usually required in these regions. In this Chapter we investigate two other stopping criteria, one based on the optical depth and the other one based on the dust density dispersion inside the cell to solve

the sharp edges.

This Chapter is divided as follow: in Section 5.2 we introduce and discuss a new grid subdivision criterion based on optical depth, and we compare it with the dust mass criterion. We also discuss a possible combination of both criteria. In Section 5.3 we focus on the particular problems caused by strong gradients and sharp edges and formulate another grid subdivision criterion designed to solve these problems. in Section 5.4 we present our conclusions.

5.2.1 Implementation of an optical depth criterion

For the construction of both the octree and the k-d tree based dust grids we have used so far, we have adopted a simple mass-based criterion to stop the recursive subdivision of the nodes. As long as the fractional dust mass $\delta = M/M_{\text{tot}}$ in a node is larger than a preset threshold value δ_{max}, the node is further subdivided. Here, the mass in a node is determined by evaluating the true input density at N_{ran} randomly generated positions $\boldsymbol{x}_i$ within the node, i.e.

$$M = \frac{V}{N_{\text{ran}}} \sum_{i=1}^{N_{\text{ran}}} \rho_{\text{t}}(\boldsymbol{x}_i) \tag{5.1}$$

with V the volume of the node. This criterion ensures that there will be more subdivision, and hence higher resolution, in regions with higher density, which is exactly what is desired. Moreover, the criterion is very easy to implement. One weakness of this construction algorithm is that it does not distinguish between large cells with a low dust density and small cells with a large density. This implies that different cells, even if they contain the same dust mass, can have strongly different volumes or densities. In order to resolve the crucial regions where the radiation field changes most rapidly, it probably makes sense to subdivide those cells with a high density slightly more than the ones with a lower density, even if they contain the same mass. This inspired us to look for another criterion that can be used instead of, or in addition to, the mass criterion.

There are different possible options that can be explored to stimulate the subdivision of nodes with a high density. All of these, essentially, use a combination of the mass and the volume of a node, and these quantities are easy to calculate during the construction of the tree. We have opted for an optical depth criterion, where we continue the subdivision if the optical depth of a node is larger than a threshold τ_{max}. For the optical depth of a node, we use the maximum optical depth through the node. For cuboidal nodes (as we have in our octree and k-d tree grids), with sides a, b and c, total mass M, and opacity coefficient κ, the optical depth is

$$\tau = \kappa\, M\, \frac{\sqrt{a^2 + b^2 + c^2}}{abc} \tag{5.2}$$

We prefer this criterion above, for example, a criterion based on the mean density, as the optical depth is a quantity that has a direct link to the radiative problem (changes in the radiation field are proportional to the optical depth in the optically thin case).

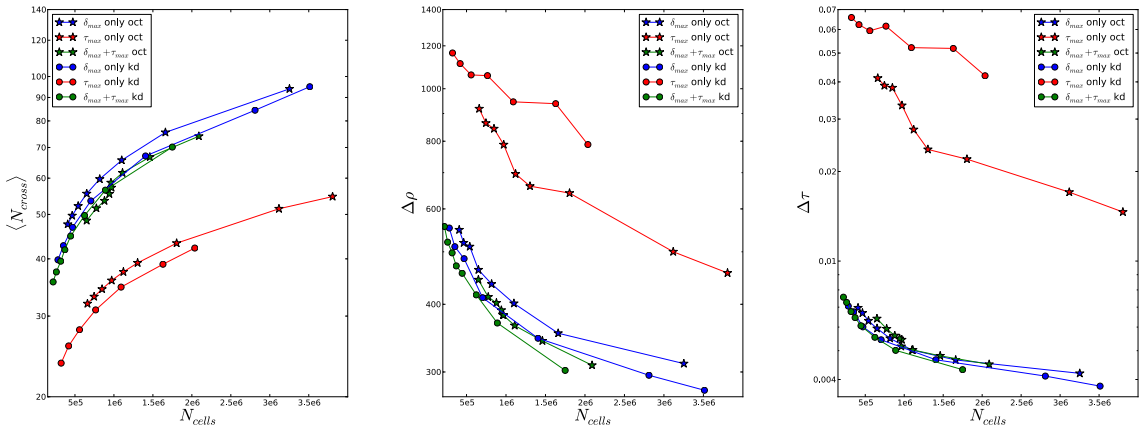

Figure 5.1: Comparison of the grid quality metrics for octree (stars) and *k*-d-tree (dots) based grids of the spiral galaxy model, using different node subdivision stopping criteria. The blue lines correspond to a mass threshold only, the red lines lines to an optical depth threshold only, and the green lines to a combination of both criteria. The different panels represent the average number of cells crossed per path $\langle N_{\text{cross}} \rangle$, the density quality $\Delta\rho$, and the optical depth quality metric $\Delta\tau$ as a function of the total number of cells in the grid, N_{cells}.

A first question to consider is whether this optical depth criterion can be used an alternative for the mass criterion we have used so far. In Figure 5.1 we show the results of test simulations based on the logarithmic three-armed spiral galaxy model. For both the octree grid (stars) and the *k*-d tree grid (dots), we constructed a set of dust grids using only a mass criterion (blue lines) and using only an optical depth criterion (red lines). The three different panels compare the grid metrics $\langle N_{\text{cross}} \rangle$, $\Delta\rho$ and $\Delta\tau$ as a function of the total number of grid cells N_{cells}. It is clear from this figure that using only the optical depth criterion is not a sensible option. For a fixed N_{cells}, an optical depth based grid has a stronger subdivision in the high density regions compared to a grid with mass based subdivision, but, unavoidably, this also results in a larger number of large cells. The positive result is that the former grids are faster, in the sense that the average path crosses fewer cells. However, this advantage does not weigh up against the loss of accuracy: the optical depth based grids have a much poorer accuracy than the mass based grids, as measured by both $\Delta\rho$ and $\Delta\tau$. To achieve the same accuracy, around an order of magnitude more cells are required.

5.2.2 Combination of mass and optical depth criteria

This does not imply that the optical depth criterion is useless, as it can also be combined with the mass criterion. In Figure 5.1 we also show the results of a grid that uses a combination (green lines) of both criteria (details on how these two criteria are combined are given below). Here we clearly see that the combination is advantageous: by

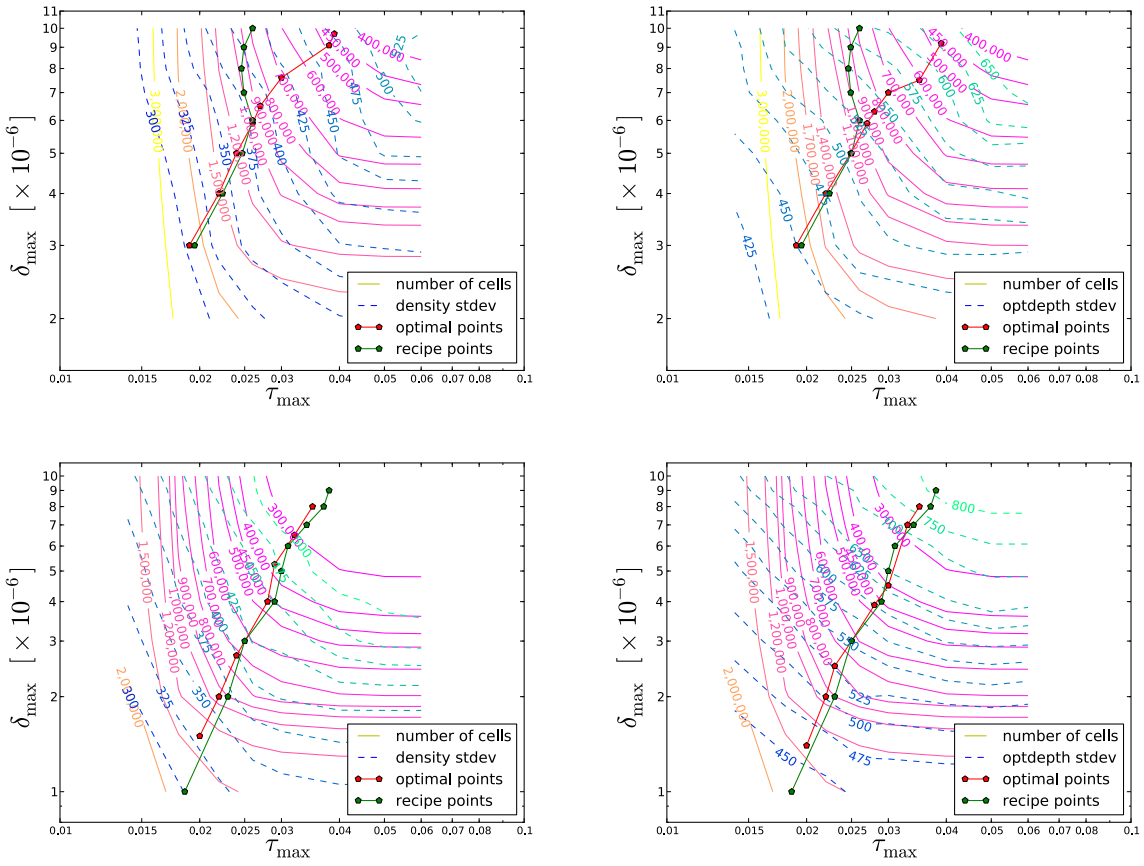

Figure 5.2: Contour plots illustrating different properties of octree grids (top panels) and k-d tree grids (bottom panels), corresponding as a function of the $\delta_{\max}$ and $\tau_{\max}$ threshold values. The solid lines in each panel correspond to lines of equal numbers of grid cells, whereas the dashed lines correspond to iso-quality contours, corresponding to the density quality metric $\Delta\rho$ (left panels) and the optical depth quality metric $\Delta\tau$ (right panels).

combining both criteria, we can improve the accuracy of the grid, as measured by both $\Delta\rho$ and $\Delta\tau$, and we decrease the average number of cells crossed on a path, resulting in a speed-up of the simulation.

A useful tool to understand the complex interplay between these two quantities are contour plots that display the total number of grid cells and the different grid quality metrics as a function of the stopping criteria $\tau_{\max}$ and $\delta_{\max}$. Figure 5.2 shows such plots for the logarithmic three-armed spiral galaxy model, for both the octree and k-d tree grids. In each of these panels, the stopping criteria become more stringent towards the bottom-left corner. Consequently, the number of cells and the quality increase towards that same corner.

From these plots, we can identify the best combination of the stopping criteria to construct a grid with a certain quality metric. Assume, for example, that we want to construct an octree based grid with a density quality metric $\Delta\rho = 375$ (recall that the

absolute value is not relevant). We can then look at the top left plot, which displays the contours of N_{cells} and $\Delta\rho$ as a function of δ_{max} and τ_{max}. The contour corresponding to $\Delta\rho = 375$ connects all points in the parameters space that correspond to grids with the same quality. We can, for example, create such a grid by setting $\delta_{\text{max}} = 3 \times 10^{-6}$ and $\tau_{\text{max}} = 0.033$, and looking at the N_{cells} contours, we see that this grid will contain about 1.2 million grid cells. We can relax the mass criterion to $\delta_{\text{max}} = 6 \times 10^{-6}$ and tighten the optical depth criterion to $\tau_{\text{max}} = 0.026$: this will yield a grid with the same density quality, but the number of grid cells reduces to about 1 million. If we relax the mass threshold even further to $\delta_{\text{max}} = 10^{-5}$ and tighten the optical depth threshold to $\tau_{\text{max}} = 0.022$, we obtain another grid with the same density quality, but the number of cells increases again to about 1.4 million. The same exercise can be repeated for other values of the density quality, but also for the optical depth quality. The bottomline is always the same: for a given quality requirement, there seems to be an optimal combination of δ_{max} and τ_{max} that yields grids with a minimum number of cells. Typically, the number of cells in this ideal combination is reduced by 20% compared to the grid based on a mass criterion only (which corresponds to the asymptotic values of the contours towards the right in the panels of Figure 5.2).

These figures also demonstrate the superiority of the *k*-d tree compared to the octree. In Section 3.4.2 we already showed that *k*-d trees are superior to octrees for the case of a simple mass subdivision stopping criterion. Here we see that the same conclusion can be drawn for grids in which more advanced tree construction criteria are adopted. Taking the same example as used above, we see that the smallest octree with a density quality $\Delta\rho = 375$ contains around 1 million cells, whereas a *k*-d tree with 800,000 cells can be constructed with the same quality.

5.2.3 The search for the optimal $\delta_{\text{max}} - \tau_{\text{max}}$ combination

The question is now how the two criteria need to be combined to give the optimal results. In other words, how do we set the values δ_{max} and τ_{max} such that this combination is ideal? In our parameter space study, we can identify these point by searching along every iso-quality contour the point that corresponds to the smallest number of grid cells. These points are indicated in red in the different panels of Figure 5.2. However, it is obviously impossible to construct this entire parameter space of grids for every possible radiative transfer simulation. Instead, it would be useful to have a simple recipe that can identify this combination. A simple numerical relation between δ_{max} and τ_{max} seems impossible, as the useful range of τ_{max} values depends on the total mass, the geometric complexity, and the opacity of our model.

Our approach consists of two steps. As a first step, we fix the value of δ_{max} and con-

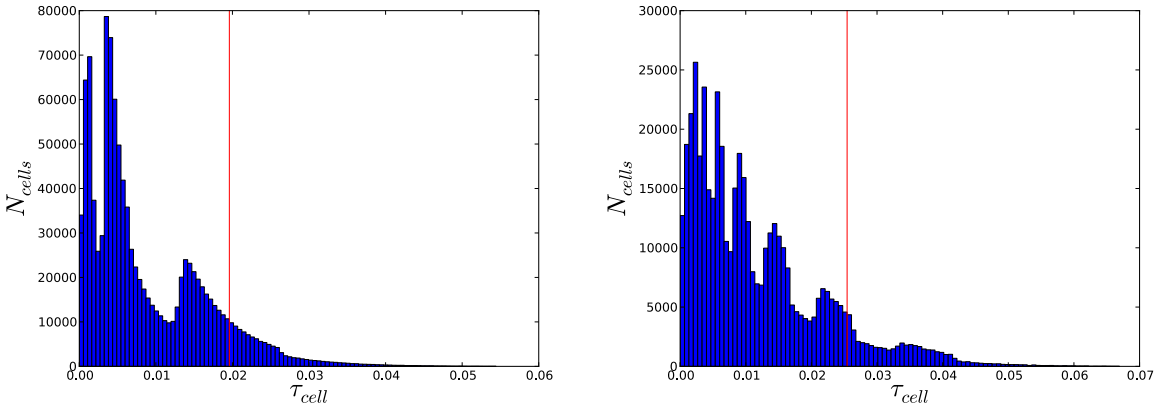

Figure 5.3: Histograms of the distribution of the optical depth τ_{cell} in each cell for the spiral galaxy model octree grid (left panel) and k-d tree (right panel), corresponding to a mass threshold criterion $\delta_{\text{max}} = 3 \times 10^{-6}$.

struct a grid using this subdivision stopping criterion only. Subsequently, we look at the distribution of the optical depth of the cells. Figure 5.3 shows the histograms of cell optical depth for the logarithmic spiral galaxy models for a fixed $\delta_{\text{max}} = 3 \times 10^{-6}$, for the octree and k-d tree grids respectively. In both histograms, there is a long tail of high optical depth, but not necessarily high mass, cells which are the prime candidates for further subdivision. The vertical lines in these plots indicates the 90% percent of the optical depth distribution, which we found to be a suitable value as to where this distribution should be cut off. In other words, we create an ordered list of the τ values, and we set τ_{max} equal to the optical depth of the cell at position $0.9\, N_{\text{cells}}$. The combinations of δ_{max} and τ_{max} we have obtained in this way are indicated as green dots in the different panels of Figure 5.2, and they lie very close to the optimal points recovered from searching the parameter space.

This recipe of finding the optimal value of τ_{max} corresponding to a given value of δ_{max} is simple and fast, as the necessary calculations are easily done during the tree construction phase. The recipe is exactly the same for both octree and k-d tree based grids.

In Figure 5.4 we applied this recipe on the SPH spiral galaxy model as a final test case. The blue lines in this figure represent simulations with only a mass threshold, whereas the green lines correspond to simulations with a combination of a mass and optical depth threshold according to the recipe described above. For the same total number of grid cells, both approaches result in roughly the same accuracy, as measured by $\Delta\rho$ and $\Delta\tau$ (middle and right panels). The important difference between both approaches it the average number of cells crossed per path (left panel): the simulations with the combined δ_{max} and τ_{max} criteria have a significantly lower value of $\langle N_{\text{cross}} \rangle$, which

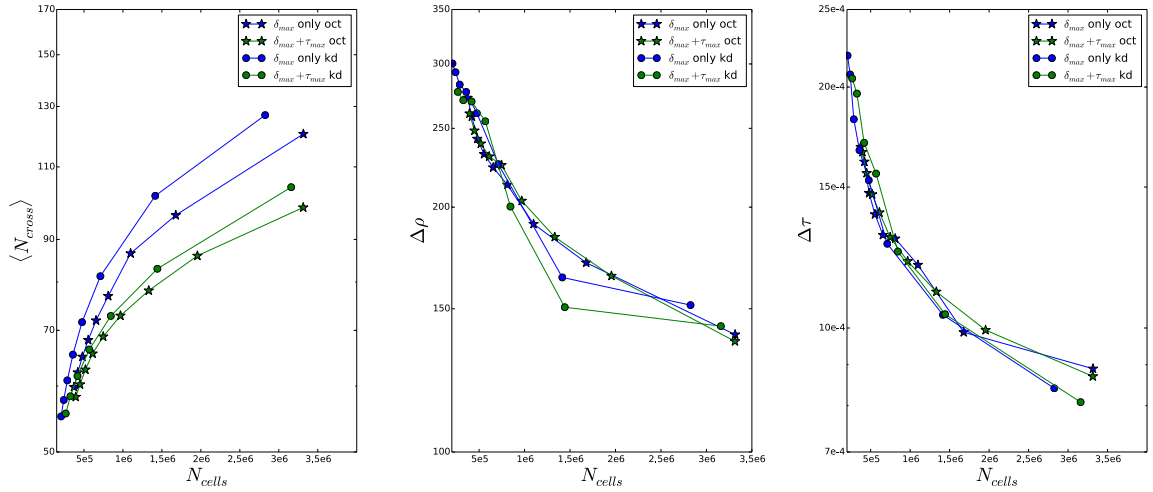

Figure 5.4: Comparison of the grid quality metrics for octree (stars) and k-d tree (dots) based grids of the SPH galaxy model, using different node subdivision stopping criteria. The blue lines correspond to a mass threshold only, and the green lines to the combination of both criteria according to the simple $\delta_{\max} - \tau_{\max}$ recipe detailed in Section 5.2.3. The different panels represent the average number of cells crossed per path $\langle N_{\text{cross}} \rangle$, the density quality $\Delta\rho$, and the optical depth quality metric $\Delta\tau$ as a function of the total number of cells in the grid, N_{cells}.

means that the simulations will be correspondingly faster. Our conclusion is that an additional optical depth criterion, chosen according to a simple recipe, is very useful in producing octree or k-d trees with fewer cells for a given quality requirement, or vice versa, with higher quality for a fixed number of grid cells.

5.3.1 Strong gradients and sharp edges

The other problem we referred to in the Introduction is the issue of very strong gradients or sharp boundaries in the density fields. Grids based on a mass criterion (or the combination of a mass and optical depth criterion) have difficulties in dealing with these. A clear example is the octree based grid for the clumpy AGN model considered in Figure 3.1. This model is characterised by a density field with sharp boundaries at the edges of the torus. During the tree construction process, we encounter many nodes at the edges of this boundary, that only have a tiny and compact corner filled with dust. When we compute the dust mass in such a node, it will soon be below the dust mass (and/or optical depth) threshold, such that the subdivision is stopped. This result is relatively large cells with a relatively low density, whereas the true underlying density field is relatively high in one tiny corner and zero in most of the cell, see the central panel in Figure 5.6 . This automatic stopping of subdivision is a problem, as the regions with strong density gradients and/or sharp boundaries are exactly regions that we want to resolve at high resolution.

One way to solve this problem is to introduce artificial boundaries in the grid. In the case of the clumpy AGN model, one could construct a hierarchical grid within the sharp boundaries of the torus itself. This solution might work efficiently for a number of analytical models, but it is not the general solution desired for arbitrary applications, where the occurrence and location of sharp boundaries and strong gradients is not always known a priori.

5.3.2 Implementation of a density gradient criterion

Our proposed solution is to introduce a node subdivision criterion that depends on the density gradient within a node, and add this criterion to the already applied dust mass (and optical depth) threshold criteria. We have considered a very simple approach that does not introduce a strong computational overhead. During the construction of the grid, the mass density is evaluated in N_{ran} random positions in each node as part of the estimate of the mass in that node. If a certain node is not to be subdivided further according to the δ_{max} and/or τ_{max} criteria, we compute the quantity

$$q = \begin{cases} \dfrac{\rho_{\text{max}} - \rho_{\text{min}}}{\rho_{\text{max}}} & \text{if } \rho_{\text{max}} > 0, \\ 0 & \text{if } \rho_{\text{max}} = 0. \end{cases} \tag{5.3}$$

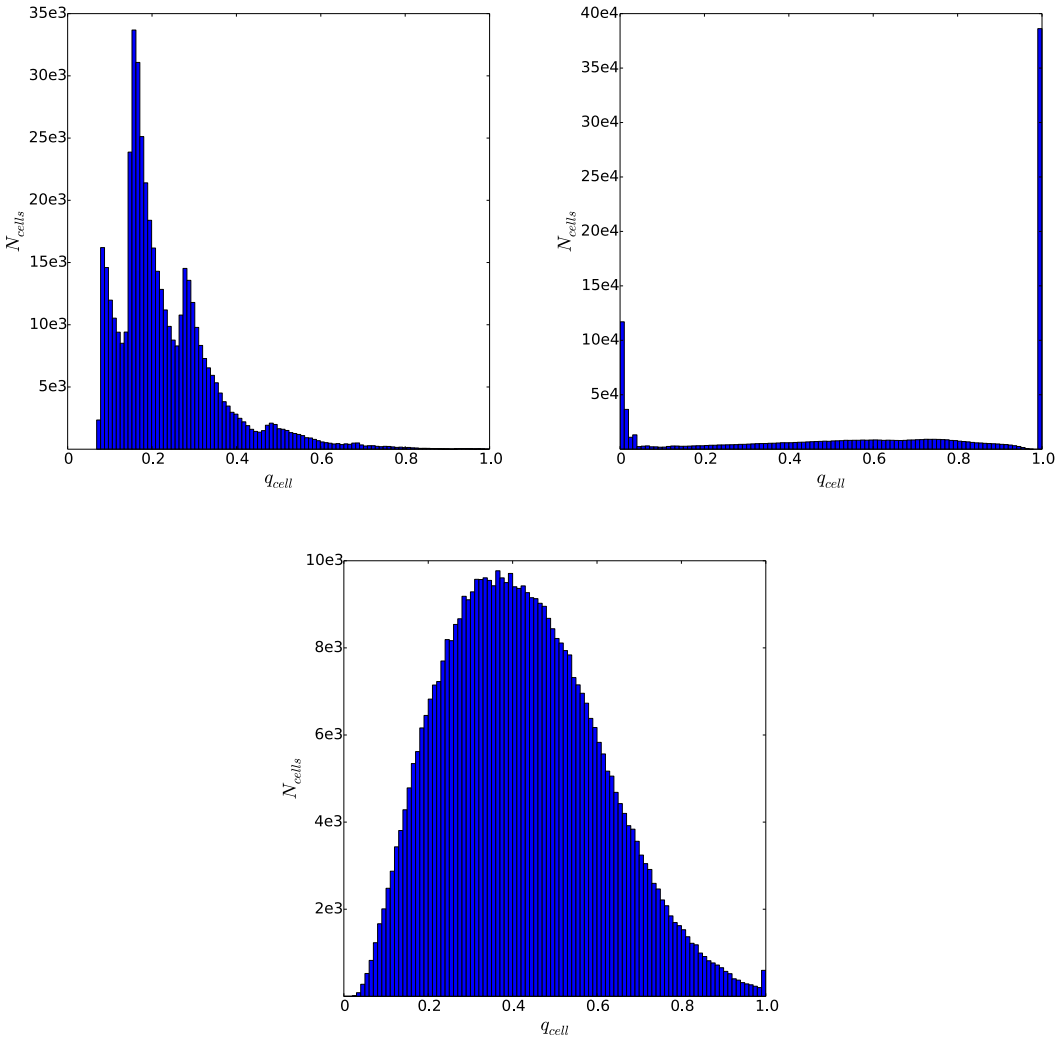

Figure 5.5: Histograms of the distribution of the density dispersion q in each cell in our three models using the k-d tree grids, corresponding to a mass threshold criterion $\delta_{\max} = 3 \times 10^{-6}$. The top left panel is the three-armed spiral galaxy model, the top right panel the clumpy AGN model, and the bottom panel the SPH galaxy model.

where $\rho_{\min}$ and $\rho_{\max}$ are the smallest and largest sampled density values from the list of N_{ran} sampled positions in the node. The quantity q is a simple measure for the uniformity of the density within the node: for a constant density in the node, $q = 0$, whereas q approaches 1 if a steep gradient is present (the special case $\rho_{\max} = 0$ is included as it is possible that a cell in the tree is empty, in which case the uniform value $q = 0$ should be returned). The additional criterion we impose is that a node is subdivided if q exceeds a preset maximum value $q_{\max} \lesssim 1$. In principle, nodes that contain a sharp edge will continue to be subdivided for ever, since such cells have by definition $q = 1$. Thus it is important to always specify a reasonable maximum subdivision level when using this subdivision criterion.

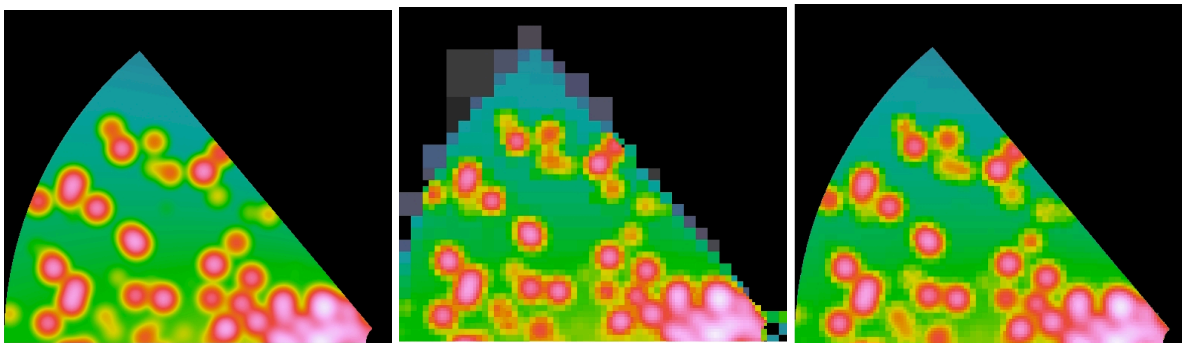

Figure 5.6: Illustration on how the density dispersion criterion $q_{\rm max}$ solves the problem of sharp edges in models such as the AGN torus. In this example we used an octree grid. The left panel represents a cut through the true dust density in xz plane, and the central panel shows the grid density as obtained without a density dispersion criterion with about 3 million cells. The edges of the torus are clearly poorly resolved. The right panel shows the grid density after adding the density dispersion criterion $q_{\rm max} = 0.99$ and a maximum subdivision level of 10. The edges are now extremely well resolved using about 7 million of additional cells.

In Figure 5.5 we show histograms of q for k-d tree based grids for the three test models we consider, before applying any q-based subdivision. The logarithmic three-armed spiral galaxy model (top left panel) is the smoothest and most regular of the three models, and is characterised by cells in which the vast majority has $q < 0.35$. The SPH galaxy model (bottom panel) is characterised by a somewhat more irregular, but still relatively smooth density field. The corresponding distribution of q values is a fairly broad distribution that peaks around 0.35 and then decreases smoothly towards larger values of q. A small number of cells have $q = 1$: these correspond to cells at the edges of cavities in the dust density. Finally, the clumpy AGN model (top right panel) is designed to be a test model with strong density gradients and sharp edges. This is clearly evident in the histogram: a large fraction of the cells is characterised by large values of q and particularly conspicuous is the large number of cells with $q = 1$, corresponding to grid cells overlapping with the sharp edge of the torus. In such a model, we clearly need higher resolution for those cells. Figure 5.6 illustrates the differences in the octree based grid for this model before and after adding the q-based subdivision criterion. This simple recipe clearly solves the problem.

5.4 Discussion and conclusions

In this Chapter, we have investigated whether there are useful alternatives to the simple mass threshold as a criterion to stop the recursive subdivision of the nodes in hierarchical trees (both octrees and k-d trees). In order to stimulate the subdivision of small, high-density cells, we have tested the option of an optical depth criterion, but this gave rise to grids with an unacceptably low accuracy. A combination of a mass and an optical depth criterion, however, turned out to be a sensible criterion. Using an optimal combination of both, it was possible to reduce the number of cells in the grids by 20% for a given quality requirement, and also decrease the average number of cells crossed on a path, resulting in faster run time of the simulations. We have presented a simple recipe that enables us to approximate this optimal combination without the need to scan the entire parameter space.

We have also considered the problem caused by discontinuities, strong gradients or sharp edges. In hierarchical grids (octrees or k-d trees) governed by mass and/or optical depth threshold criteria, such features can lead to undesirable large, low-density cells, whereas a strong subdivision is particularly needed in these cases. We have presented a simple solution for this problem, in the form of an additional gradient threshold criterion. The criterion is very simple to implement and is shown to give the desired results.

The main results of this investigation are that, in the context of radiative transfer simulations, we can strongly advocate the use of the combination of different subdivision stopping criteria, rather than a simple mass criterion, which can lead to more efficient grids. While this is another step forward towards the construction of the ideal grid, we are well aware that this is not the end stage. A number of side notes are required.

The first caveat refers to the different grid quality metrics that we have used in this Chapter and the previous Chapters. We have attempted to quantify the quality of a grid using different criteria: the total number of cells, the average number of cells crossed per path, and an estimate of the standard deviation of the density and optical depth discretisation error. These quantities are an attempt to translate what one would consider intuitively as a good grid to a quantitative measure by which different grids can be compared. They are only based on the dust density field, and they are relatively straightforward to calculate. But the question remains whether these metrics are sufficient to really measure whether one grid is better than the other for radiative transfer simulations.

As we mentioned in the introduction, the ideal spatial grid in radiative transfer simulations should discretise the intensity of the radiation field as accurately as possible, but

this quantity is unknown at the start of the simulation (it is exactly the goal of radiative transfer simulation to recover the radiation field). As the radiation field is not only determined by the dust density, but equally well by the distribution of sources and the optical properties of the dust, it is simply impossible to construct the ideal grid with only knowledge of the dust density field, or to construct grid quality metrics based on the density field alone that measure the appropriateness of a grid.

A more advanced option could in principle be achieved iteratively from running a series of radiative transfer simulations, in which the grid is adapted at every step based on the properties of the radiation field (strength of the radiation field, temperature distribution,...) in the previous iteration step (see also Niccolini and Alcolea 2006). This approach is clearly too complex and time-consuming for every single simulation. Grid construction guidelines and quality metrics based on the dust density field alone, such as discussed in this Chapter, are probably a good compromise between effectiveness and computational cost, but future work might investigate this in more detail.

6 The dust energy balance problem

The material presented in this Chapter is original work; it is published in a slightly modified form in Saftly et al. (2015).

6.1 Introduction

Broadly speaking, the dust in galaxies can be traced in two ways. The first way is by studying the thermal emission of the dust at far-infrared (FIR) and submm wavelengths. We can determine the total dust mass of a galaxy with a reasonable accuracy by fitting a modified blackbody or more advanced models to the FIR/submm observed spectral energy distribution. Especially after the launch of the *Herschel* Space Observatory (Pilbratt et al. 2010), a wealth of FIR/submm data has become available that allowed different teams to determine dust masses in thousands of galaxies (e.g., Dunne et al. 2011; Dale et al. 2012; Smith et al. 2013; Ciesla et al. 2014). Due to the diffraction limit in the FIR/submm and the limited diameter of space observatories, detailed investigations of the distribution of the dust remains difficult, except for the most nearby galaxies (e.g., Kramer et al. 2010; Fritz et al. 2012).

An alternative method, which does not suffer from the poor spatial resolution affecting FIR/submm observations, consists of carefully modelling the attenuation effects of the dust on the stellar emission in the optical window using advanced radiative transfer techniques. Today, a range of powerful 3D radiative transfer codes is available (for an overview, see Steinacker et al. 2013), and the fitting of the radiative transfer models to data is being optimised beyond the elementary chi-by-eye (Xilouris et al. 1997; Steinacker et al. 2005; Bianchi 2007; Schechtman-Rook et al. 2012; De Geyter et al. 2013, 2014).

Traditionally, detailed radiative modelling has been applied mainly to edge-on spiral galaxies, as the dust is then clearly visible as prominent dust lanes in optical images. Most studies focus on a single galaxy (e.g., Kylafis and Bahcall 1987; Xilouris et al. 1997, 1998; Popescu et al. 2000, 2011; Baes et al. 2010; de Looze et al. 2012; De Looze et al. 2012; Schechtman-Rook et al. 2012) or modest sets of edge-on spiral galaxies (Xilouris et al. 1999; Bianchi 2007; MacLachlan et al. 2011; De Geyter et al. 2014).

A comparison of the extinction and the FIR/submm emission, i.e. a study of the dust energy balance, gives the strongest constraints on the dust content of spiral galaxies. Dust energy balance studies of edge-on spiral galaxies reveal a discrepancy between the FIR/submm emission predicted by radiative transfer models and the observed emission. Although the radiative transfer models explain the optical extinction very well, they typically underestimate the observed dust emission by a factor of about three (Popescu et al. 2000; Misiriotis et al. 2001; Alton et al. 2004; Dasyra et al. 2005; Baes et al. 2010; de Looze et al. 2012; De Looze et al. 2012). This has become generally known as the dust energy balance problem in edge-on spiral galaxies.

Two broad scenarios have been proposed to explain this problem. A first possibility is

that FIR/submm emissivity, standardly taken from semi-empirical dust models based on the interstellar medium (ISM) in the Milky Way, is underestimated by a factor of a few. This idea was advocated by Alton et al. (2004) and Dasyra et al. (2005), and is corroborated by the large range of empirical values for emissivity circulating in the literature. However, based on a detailed study of the edge-on spiral UGC 4754, Baes et al. (2010) argued that this possibility cannot explain the discrepancy. Indeed, they found an incompatibility between the absorbed stellar luminosity as obtained from the radiative model fits to the optical data and the emitted dust luminosity in the FIR/submm that cannot be lifted by just increasing the value of the dust emissivity.

The alternative scenario to explain the dust energy balance problem in spiral galaxies is geometrical in nature. As already indicated, the relative star-dust geometry in a galaxy is extremely important for the amount of attenuation. If a sizeable fraction of the dust is distributed in such a way that it hardly attenuates the bulk of the starlight, one could easily underestimate the amount of dust from radiative transfer modelling. At the same time, this dust can still contribute substantially to the observed FIR/submm emission. How exactly this additional dust would have to be distributed is subject to debate, and various options have been proposed.

One option is a very thin and dense dust disc next to the thicker dust disc that is responsible for the dust lane in the optical (Popescu et al. 2000, 2011; Misiriotis et al. 2001; Driver et al. 2007). For example, Schechtman-Rook and Bershady (2014) find a very thin dust disk in certain edge-on spiral galaxies. On the other hand, Dasyra et al. (2005) showed that such a disc would have an observational signature at NIR wavelengths, which is at odds with the observations of the prototypical edge-on spiral galaxy NGC 891.

A second option is that most of the dust is locked up in so-called "clumps", a rather vaguely defined term used in the radiative transfer community to indicate any form of inhomogeneities relative to a smooth medium. One can consider large-scale inhomogeneities such as bars and spiral arms, as well as small-scale structures such as dusty molecular clouds with or without embedded young stars. Thanks to the advancement of 3D dust radiative transfer, the effect of a non-homogeneous multi-phase dusty medium has been investigated by various teams (e.g., Witt and Gordon 1996, 2000; Wolf et al. 1998; Városi and Dwek 1999; Bianchi et al. 2000; Hegmann and Kegel 2003; Indebetouw et al. 2006). While the dusty ISM in spiral galaxies is far from smooth and homogeneous, the radiative transfer models being fitted to the optical images in energy balance studies are usually smooth and axisymmetric. This simplification may very well affect the results of these studies.

Whether or not an inhomogeneous distribution of the dust, on small and/or on large

scales, is a possible solution for the dust energy balance problem is still an open question. Several studies have attempted to address this issue. Concerning the role of spiral arms, the work of Misiriotis et al. (2000, hereafter M00) is the most advanced study. They set up a suite of galaxy models with an analytical spiral structure, created mock edge-on optical images for these galaxies, and subsequently fitted these simulated observations with a smooth, axisymmetric radiative transfer model. The fitted models were surprisingly accurate; essentially all parameters of the input model (dust mass, inclination, scale parameters of stars and dust, etc.) were properly recovered. In a similar way, Misiriotis and Bianchi (2002, hereafter M02) investigated the effect of clumps or small-scale inhomogeneities: rather than models with a spiral perturbation they adopted the clumpy disk galaxy models of Bianchi et al. (2000) as input models. They concluded that, for the range of clumpy distributions they considered, the neglect of clumping results in a systematic underestimate of the dust mass. The underestimate was found to be never larger than 40%, however.

These results seem to cast doubts on the ability of inhomogeneities such as spiral arms or large molecular clouds to provide an answer to the dust energy balance problem. However, one needs to take into account that the input models used in the studies by M00 and M02 were still relatively well-behaved. They were constructed using theoretical perturbations on essentially the same exponential discs as those used in the fitting, and still featured a rather symmetric and regular geometry. They are therefore a relatively poor representation for real galaxies, which are generally characterised by a much larger degree of geometrical complexity and asymmetry.

The goal of this Chapter is to investigate whether a complex and inhomogeneous dusty ISM could provide an answer to the dust energy balance problem. In Section 6.2 we start with basic input models similar to those used by M00 and M02, and we verify that our fitting procedure recovers similar results. In Section 6.3 we apply the same approach to galaxy snapshots produced by state-of-the-art hydrodynamic simulations. We consider two models from different simulations, both of which show a complex and asymmetric geometry similar to our own Milky Way. In Section 6.4 we discuss and interpret the results, and a summary is presented in Section 6.5.

Before we set out to model mock images from hydrodynamical simulations and compare the results to previous work, we first need to investigate whether we can reproduce the results of this previous work. In particular, we should verify that our fitting routine can reproduce the results of M00 and M02 for basic input models. This is not as obvious as it may seem. Indeed, while we follow a similar approach, there are potentially relevant differences in the modelling mechanisms. For example, the radiative transfer code used by M00 and M02 adopts the so-called method of scattered intensities (for details, see Kylafis and Bahcall 1987; Xilouris et al. 1997; Baes and Dejonghe 2001b), whereas the fundamental algorithm in our SKIRT code is the Monte Carlo method. Perhaps more importantly, while M00 and M02 fit each model to a single image, we use oligochromatic fitting, i.e. we fit a single model simultaneously to images in the five SDSS optical bands. This approach can help to eliminate degeneracies in the parameter space (De Geyter et al. 2014). Hence, we set up two test cases that are very similar to the basic input models explored by M00 and M02.

6.2.1 The input models

The first step in our modelling is the setup of the models, i.e., the choice of the basic model from which to start and the perturbations that we apply this model. For the underlying model, we assume a smooth and axisymmetric model, consisting of a double-exponential stellar disc, a flattened Sérsic bulge, and a double-exponential dust disc (see also, e.g., Xilouris et al. 1999; Bianchi 2007; MacLachlan et al. 2011). For the parameters of the underlying model, we use the average values obtained by fitting 10 real galaxies with FitSKIRT from the CALIFA survey (see Table 4 in De Geyter et al. 2014).

First, we consider a spiral structure perturbation, similar to the models by M00. Both the stars in the disk and the dust are perturbed into a logarithmic spiral arm pattern. For the parameters of the spiral arm perturbation, we select an average model also considered in M00. There are two spiral arms, the weight of the spiral perturbation is 30% for the stars and 40% for the dust, and the spiral arm pitch angle is 20 degrees.

Secondly, we set up an idealised model for a clumpy disc galaxy similar to M02. In this case, we divide the dusty medium into a smooth and a clumpy component. We take a different approach from Bianchi et al. (2000), who adopted the two-phase medium algorithm explored by many authors (Witt and Gordon 1996, 2000; Matthews and Wood 2001; Wolf et al. 1998; Stalevski et al. 2012). Instead, we deposit half of the total dust mass in 10,000 individual spherical clumps, each with an outer radius of 300 pc and an

Table 6.1: Model parameter values recovered by the FitSKIRT radiative transfer fits for two basic input models. The third column provides the "true" values of the input models, and the fourth and fifth columns list the values recovered for the model with a spiral arm perturbation and a clumpy structure respectively. For a definition of each parameter, see De Geyter et al. (2014).

Parameter	Units	Input	Spiral	Clumpy
$h_{R,*}$	kpc	4.23	4.26 ± 0.03	4.48 ± 0.06
$h_{z,*}$	kpc	0.51	0.59 ± 0.03	0.58 ± 0.01
R_{eff}	kpc	2.31	2.44 ± 0.15	2.52 ± 0.09
n	—	2.61	2.27 ± 0.12	2.0 ± 0.1
q	—	0.56	0.58 ± 0.01	0.55 ± 0.01
$h_{R,\text{d}}$	kpc	6.03	4.89 ± 0.56	4.94 ± 0.22
$h_{z,\text{d}}$	kpc	0.23	0.201 ± 0.004	0.203 ± 0.003
M_{d}	$10^7\ M_\odot$	3.02	2.34 ± 0.12	2.5 ± 0.1
i	deg	90	90.01 ± 0.01	89.96 ± 0.02

internal cubic spline kernel distribution (Hockney and Eastwood 1981). Each of these clumps is positioned at a random location chosen according to the underlying smooth dust density field (see also De Looze et al. 2014; Camps and Baes 2015).

6.2.2 Creation of mock images

The second step in our analysis is the creation of mock images for these two models. In particular, we need images in the SDSS *ugriz* bands and in the edge-on orientation, so that they can be used subsequently for radiative transfer modelling. The mock images were created with SKIRT (see Chapter 2).

6.2.3 Radiative transfer modelling

Finally, the third step in the modelling consists of fitting radiative transfer models to the mock images, as is done for real galaxies. We use the FitSKIRT code for this goal (see Section 2.1.3). In this work, we use the same radiative transfer fitting model as the one employed by De Geyter et al. (2014) to fit real edge-on spiral galaxies. We fit a smooth axisymmetric model, similar to the underlying model, to the mock images of the perturbed model. The radiative transfer modelling essentially comes down to a strongly nonlinear χ^2-minimisation in a 21-dimensional parameter space (we consider

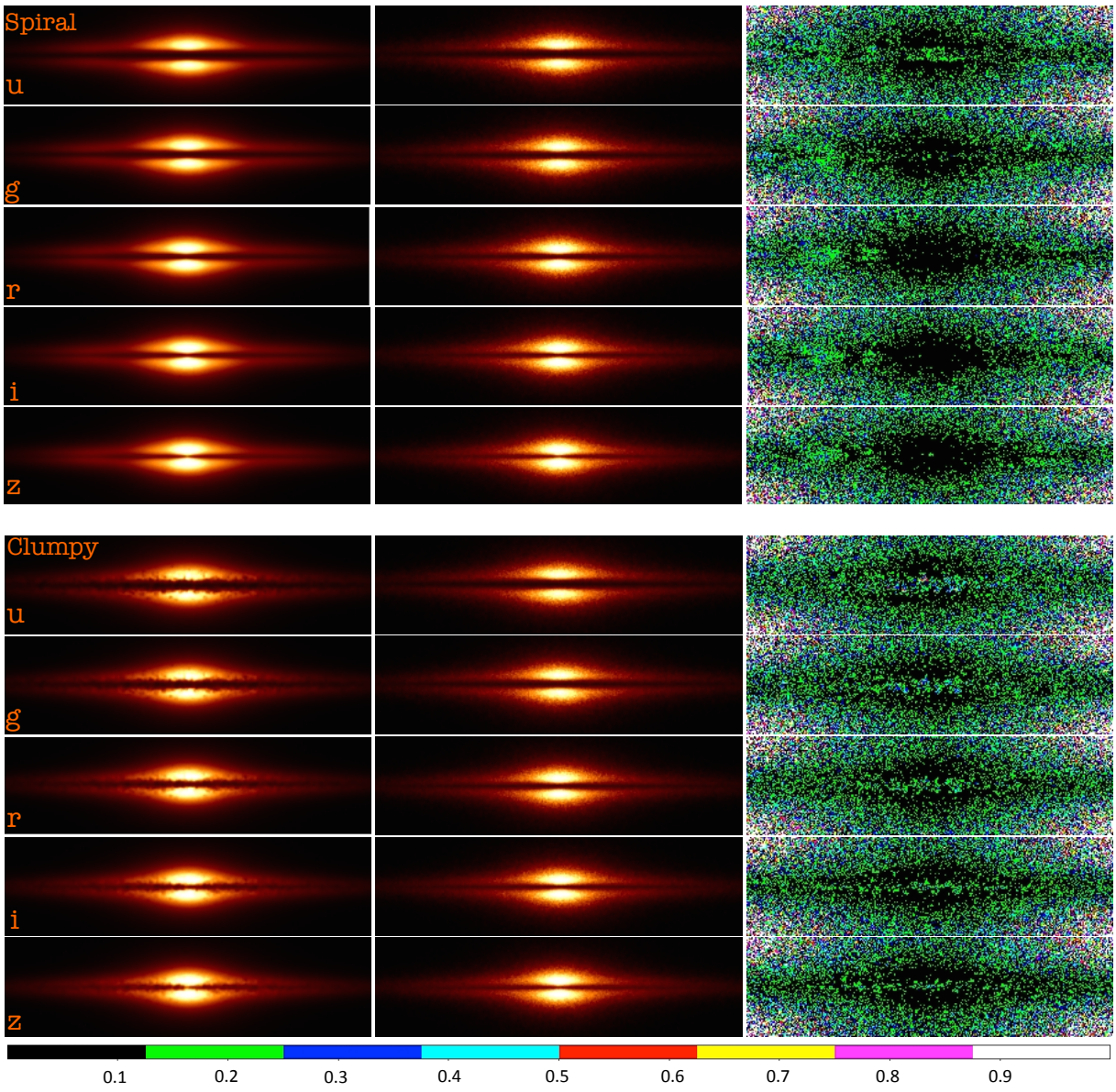

Figure 6.1: Results of the FitSKIRT radiative transfer fits for two basic input models; one with analytical spiral perturbation (upper half) and one with random clumps (lower half). The left column shows the reference images produced by SKIRT in each of the u, g, r, i, and z bands. The middle column shows the corresponding fit obtained with FitSKIRT. The right column contains residual images showing the relative deviation between the fit and the reference image. The colour bar at the bottom presents the scale of the deviation in the residual images.

five parameters describing the stellar geometry, two parameters for the dust geometry, the luminosity of the bulge and disc in each of the five bands, the total dust mass and three projection parameters).

The fitting results are presented in Figure 6.1 and Table 6.1. The leftmost column in Figure 6.1 represents the original mock images in the five bands (corresponding to an azimuth of 0 deg), the central column shows the images corresponding to the best fitting model, and the rightmost column presents the residual images, expressed as the relative difference between the surface brightness of the real image and the model fit. The residual frames for the first input model show some discrepancies to the left of the centre of the galaxy, corresponding to a maximum in the spiral arm perturbation. Even in this feature, the relative difference between model and fit is only of the order of 20%, so this is an excellent fit. For the clumpy input model, the largest discrepancies occur in the u and g bands, where the effects of the dust are most prominent, but in general the quality of the fit is very satisfactory as well.

Table 6.1 compares the parameters recovered by the fitting procedure to the corresponding parameters of the input models. For both models, all input parameters are recovered to within 25%, and often even better. Specifically, the total dust mass is underestimated by less than 25% in both cases. These results are in line with those reported by M00 and M02.

Now that we have shown that we can reproduce the previous results by M00 and M02, we can move to the next level, and consider more realistic models for spiral galaxies. The modelling follows the same strategy as we used for the basic input models considered in the previous section.

6.3.1 The input models

In recent years, hydrodynamical simulations have started to successfully reproduce late-type spiral galaxies (Bournaud et al. 2007, 2009; Governato et al. 2009; Agertz et al. 2011; Guedes et al. 2011; Wada et al. 2011; Stinson et al. 2013; Renaud et al. 2013; Marinacci et al. 2014; Inoue and Saitoh 2014). The spatial resolution of these simulations is sufficient to resolve both large- and small-scale inhomogeneities. We consider snapshots from two different simulations for the analysis in this paper.

The first input model is taken from the simulation by Renaud et al. (2013), hereafter called the R13 simulation. This is a self-consistent hydrodynamical simulation of a Milky Way-like galaxy performed with the Adaptive Mesh Refinement (AMR) code RAMSES (Teyssier 2002). The goal of this simulation was to reproduce an isolated grand-design spiral galaxy and to focus on the structure of the interstellar medium at the highest resolution possible. The simulation resolves the ISM down to scales of 0.05 pc, and includes stellar feedback through photo-ionization, radiative pressure and supernovae. The simulation started with 30 million particles in the dark matter halo and another 30 million particles representing the stars distributed over a bulge, spheroid, thin disc and thick disc. The gaseous disc is represented with 240 million AMR cells varying in size depending on the structure of the ISM. The mass resolution is 160 $M_\odot$ for young star particles and 30 $M_\odot$ for the gas in the most refined cells. The initial components in the simulation are axisymmetric, but non-axisymmetric structures such as a prominent bar and spiral structure are developed quickly because of the instabilities in the velocity distribution.

We use the snapshot corresponding to the final state of the galaxy, after a run time of 800 Myr. We consider a box with dimensions $20 \times 20 \times 4$ kpc^3, which contains a total stellar mass of 4.4×10^{10} $M_\odot$ and a total gas mass of 3.0×10^9 $M_\odot$. The galaxy hosts a prominent bulge and spiral arms, and is characterised by a high star formation rate (SFR); the total SFR for stars younger than 57 Myr is about 7.3 $M_\odot$ yr^{-1}. The bar has a central area of 1 kpc^2 that contains almost no ongoing star formation (see Emsellem et al. 2015), whereas dense star-forming clouds are abundant at the outer regions of the bar. Along the spiral arms, dense clumps of gas and star forming regions have formed

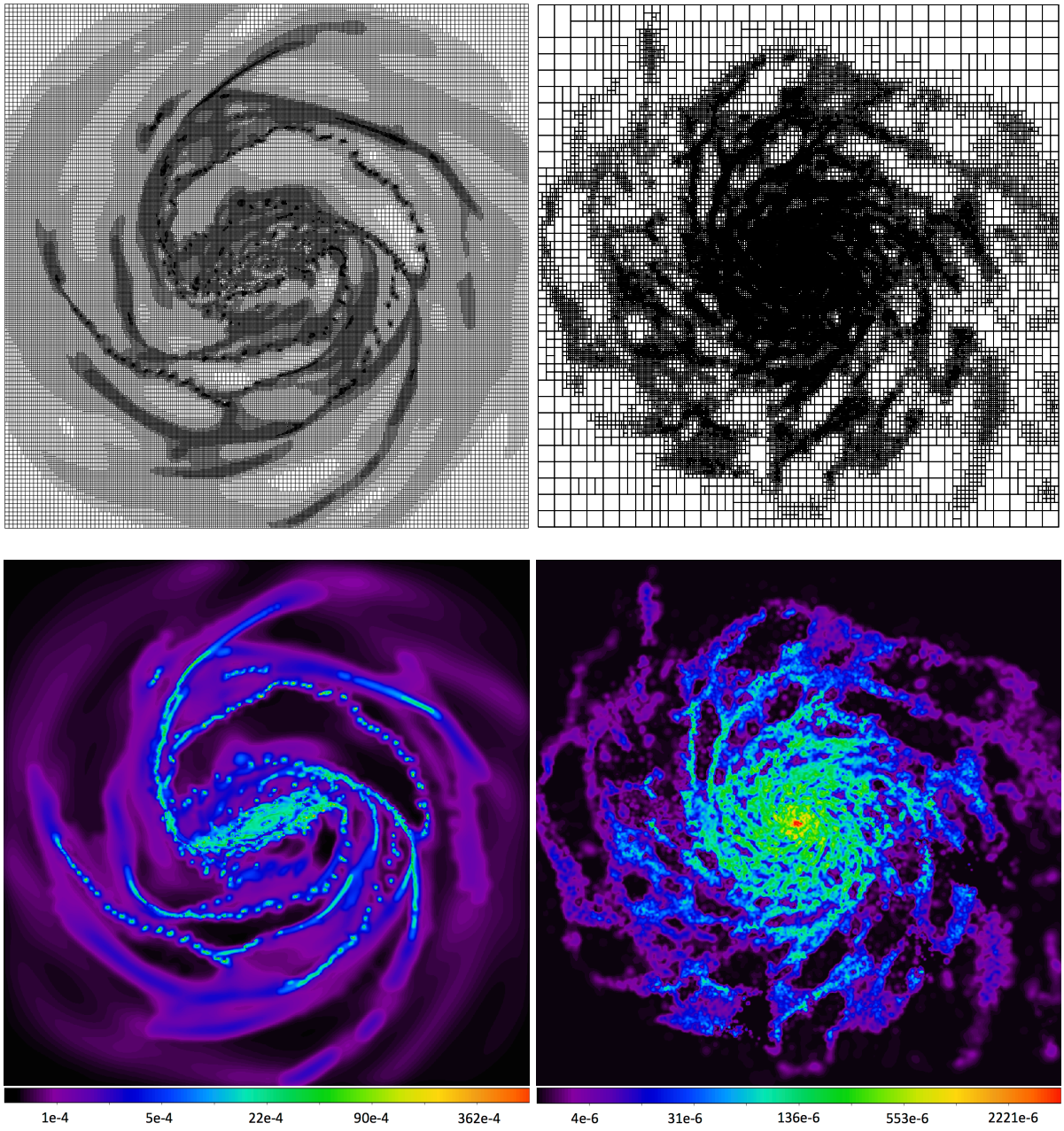

Figure 6.2: Top panels are cuts through the *k*d-tree grids along the equatorial plane of the R13 galaxy (top left panel) and of the Eris galaxy (top right panel). Bottom panels are cuts through the dust density distribution corresponding to the same plane of the R13 galaxy (bottom left panel) and of the Eris galaxy (bottom right panel). The dust density is given in $M_{\odot}$ pc^{-3}.

with a relatively uniform separation (the so-called "beads on a string"). This high level of concentration is related to the relatively short simulation run time; continuing the simulation would cause stellar feedback to more evenly spread matter along the disc.

The second input model in our study is taken from the Eris simulation (Guedes et al. 2011), one of the most advanced and realistic simulations of the formation of a Milky

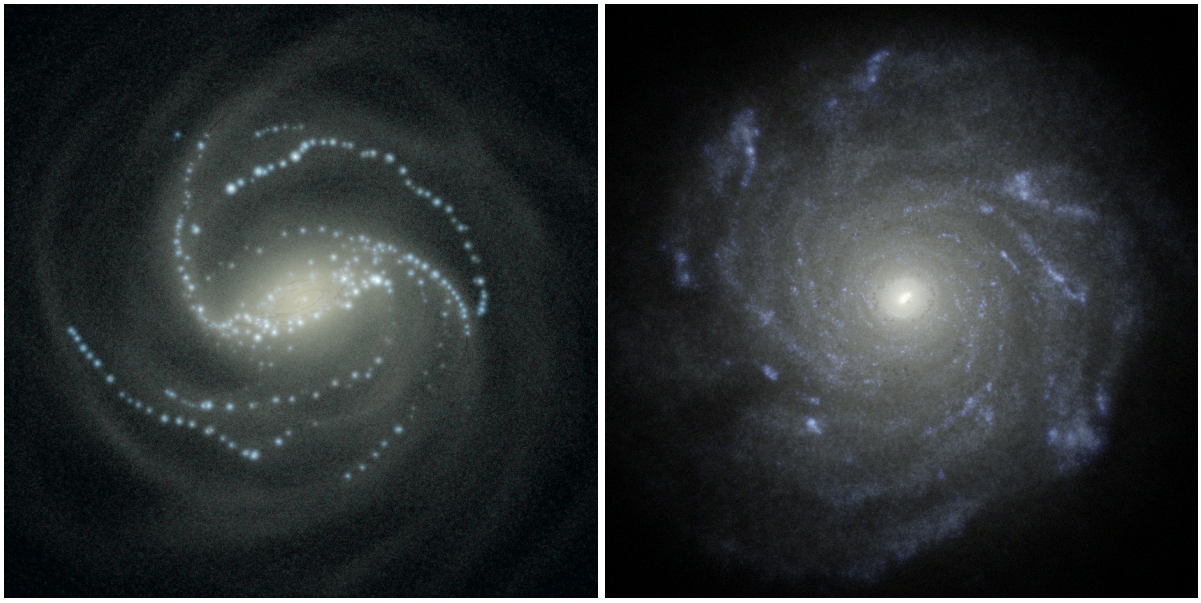

Figure 6.3: Mock face-on views for the R13 galaxy (left panel) and for the Eris galaxy (right panel). The three-colour images are based on the r, g and u band images produced by the SKIRT radiative transfer code.

Way class galaxy. Eris was set up as a zoom-in cosmological simulation, powered by the N-body/SPH GASOLINE code (Wadsley et al. 2004). The simulation follows the formation of a galaxy halo with mass $M_{\rm vir} = 7.9 \times 10^{11}\ M_\odot$ from $z = 90$ to the present epoch in a full cosmological setting. The target halo is sampled with 26 millions particles divided equally between the dark matter particles and gas particles. Apart from the obvious gravity and hydrodynamical forces, the simulation includes Compton cooling, atomic cooling, metallicity-dependent radiative cooling at low temperatures, the ionising effect of a uniform UV background, star formation and supernova feedback.

We use the final snapshot corresponding to the present epoch. At $z = 0$, Eris is a Milky Way-like galaxy characterised by a beautiful spiral structure and a small bulge in the centre. The structural properties, the mass budget in the various components, and the scaling relations between mass and luminosity are consistent with a host of observational constraints. For our analysis, we consider all particles in a box of $28 \times 28 \times 6$ kpc^3. This box has 7.8 million star particles and 0.25 million gas particles, with a total stellar mass of $3.5 \times 10^{10}\ M_\odot$ and a total gas mass of $4.3 \times 10^9\ M_\odot$ (about $5 \times 10^3\ M_\odot$ per star particle and $2 \times 10^4\ M_\odot$ per gas particle). The smoothing length for the gas particles ranges between 56 and 2455 pc.

6.3.2 Creation of mock images

The second step in the analysis is again the creation of mock images. In order to do so, SKIRT was extended with modules that read the output of hydrodynamical simulations as input for the radiative transfer calculations (see also Schaye et al. 2015). We used the GALAXEV library of simple stellar populations (Bruzual and Charlot 2003) to determine the intrinsic emission of the stars in the simulation. For the optical properties of the dust we use the BARE-GR-S dust model from Zubko et al. (2004), which is fine-tuned to be consistent with the extinction, diffuse emission and depletion in the Milky Way.

One particular aspect that needs special care is the determination of the dust density. As the hydrodynamical simulations do not track the dust directly, a recipe needs to be chosen to set the dust density from the properties of the gaseous medium. We use the assumption that a constant fraction of the metals in the ISM is locked up into dust grains. While observations show metallicity gradients across galaxies (Dobashi et al. 2008; Paradis et al. 2012) and local variations in the fraction of metals locked into dust grains (Hirashita 2012), this simplification does not affect our analysis, because we only need to create mock images reflecting a certain dust mass. In particular, we set the 3D dust density using

$$\rho_{\text{dust}} = f_{\text{dust}}\, Z\, \rho_{\text{gas}} \tag{6.1}$$

where Z is the metallicity of the gas, and f_{dust} is the fraction of metals locked up in dust grains. For the R13 simulation we use $f_{\text{dust}} = 0.3$, the same value as used in the EAGLE simulation (Schaye et al. 2015). For the Eris simulation, we use a slightly larger value, $f_{\text{dust}} = 0.5$, since this galaxy has a relatively low metal content. Both values are within the range suggested by observations, roughly between 0.2 and 0.7 (Dwek 1998; James et al. 2002; Mattsson and Andersen 2012; De Cia et al. 2013; Zafar and Watson 2013). For both simulations, the gas density can be determined from the simulation snapshot. In the R13 simulation, the metallicity is not stored or evolved, and we adopt a fixed solar metallicity. Combined with the fixed value for f_{dust} this comes down to a constant gas-to-dust ratio of 166, which is in good agreement with the gas-to-dust ratio in the Milky Way and other spiral galaxies (Zubko et al. 2004; Draine et al. 2007; Rémy-Ruyer et al. 2014). For the Eris simulation, the gas metallicity is stored for every SPH gas particle, such that the dust density can be calculated. Using a higher value of f_{dust} boosts the total dust mass, even with the rather low metallicities in this galaxy (ranging from zero up to $Z = 0.266$).

Another crucial ingredient for the present simulations is the setup of the grid on which the dust density is defined. SKIRT can handle any 3D geometry, thanks to the efficient use of hierarchical and unstructured grids for the dust medium in Chapter 3, Chapter 4,

Figure 6.4: Mock edge-on views for the R13 galaxy, looking at the head of the bar (left panel), and for the Eris galaxy (right panel). The three-colour images are based on the *r*, *g* and *u* band images produced by the SKIRT radiative transfer code.

and Chapter 5 of this thesis and in Camps et al. (2013). For the simulations in this paper, we used a hierarchical *k*-d tree with a resolution up to 0.6 pc for the R13 and 6.8 pc for the Eris simulation. For both simulations, the final grid contains about 1.5 million dust cells. Figure 6.2 shows cuts through the *k*-d tree grids (top panels) and the dust density distribution (bottom panels) in the equatorial plane for both models.

For each of the two input models, we created mock images in the SDSS *ugriz* bands, in face-on and edge-on configurations (although we only need the edge-on views for our study). Three-colour images based on the *r*, *g* and *u* bands are shown in Figs. 6.3 and 6.4. In spite of the complex intrinsic structure of both the stellar and dust distribution apparent in the face-on views, the edge-on morphology seems rather smooth and regular.

6.3.3 Radiative transfer modelling

Finally, we fit radiative transfer models to the mock images using FitSKIRT, where we use exactly the same approach as for the basic input models from the previous section. The results for both snapshots are shown in Figures 6.5 and 6.6, and in Table 6.2.

The global morphology of each input model is accurately reproduced in the fit, although some features are not fitted completely. In particular, the residual frames for the R13 model show some discrepancies in the dust lane area. This structure is most strongly present in the shortest wavelength bands, but it persists up to the *z* band. These discrepancies correspond to clumpy structures, both in the stellar distribution (the beads on a string) and in the dust distribution. However, most of the pixels in the residual frames have a discrepancy of less than 30%. In fact, the central areas of the residual frames for the R13 model shows an obvious similarity to those corresponding to the clumpy disc model (Figure 6.1, lower panels). For the Eris simulation, the dust lane is not very prominent and it has a discontinuous shape with a lot of clumpy and irregular structures up to the edges of the galaxy, which makes it a hard galaxy to fit. The residual frames show discrepancies around the bulge corresponding to the molecular clouds and star forming regions.

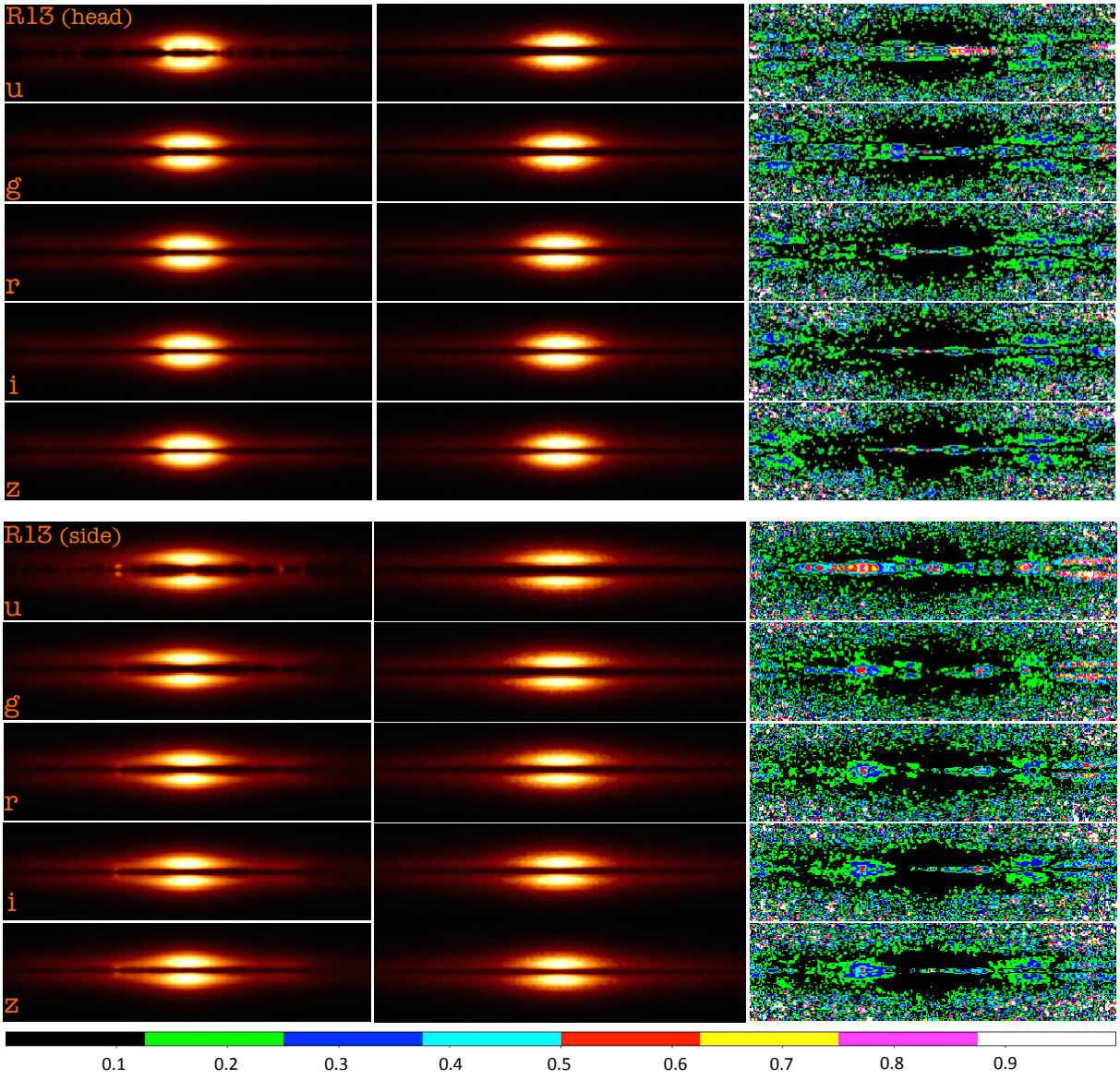

Figure 6.5: Results of the FitSKIRT radiative transfer fits for the R13 galaxy, looking at the head of the bar (upper half), and at the side of the bar (lower half). The left column shows the reference images produced by SKIRT in each of the u, g, r, i, and z bands. The middle column shows the corresponding fit obtained with FitSKIRT. The right column contains residual images showing the relative deviation between the fit and the reference image. The colour bar at the bottom presents the scale of the deviation in the residual images.

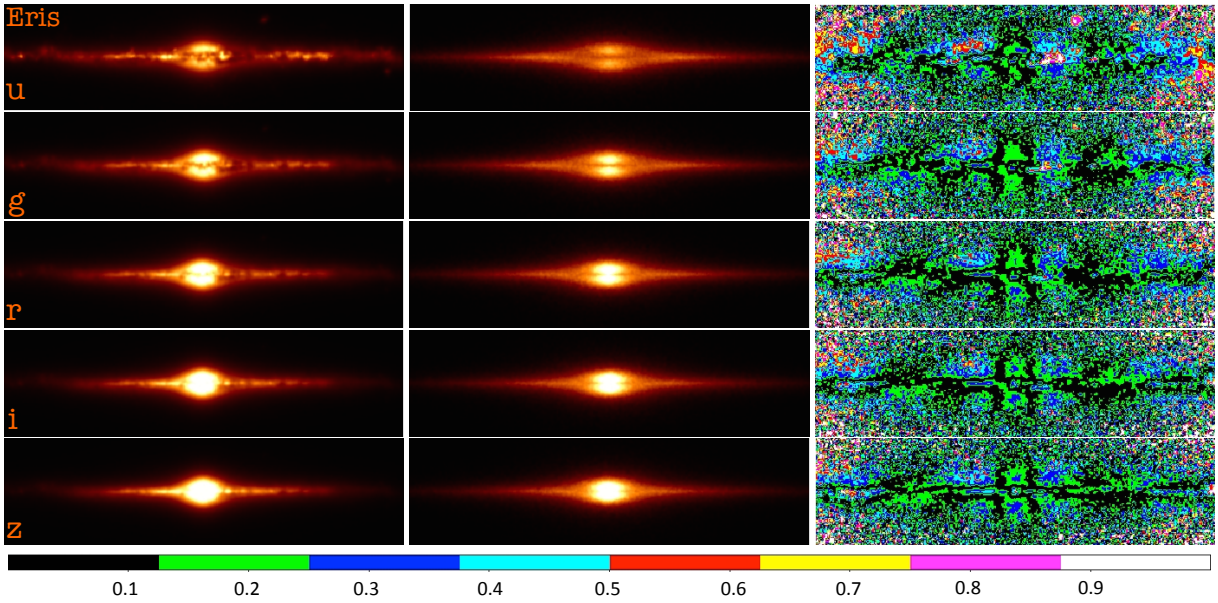

Figure 6.6: Results of the FitSKIRT radiative transfer fits for the Eris galaxy. The different panels have the same meaning as in Figure 6.5.

Table 6.2 lists the most important model parameter values recovered by the radiative transfer fits for each galaxy. To gauge the effect of the large-scale asymmetry in the R13 galaxy due to its prominent bar, we performed two independent fitting procedures based on perpendicular edge-on viewpoints, respectively looking at the head and the side of the bar. Given the dust masses of the input models ($M_{\mathrm{d,R13}} = 1.81 \times 10^7\ M_\odot$; $M_{\mathrm{d,Eris}} = 5.94 \times 10^6\ M_\odot$) and the recovered values in Table 6.2, it follows that the radiative transfer model underestimates the "true" dust mass by a factor of 2.9 ± 0.2 respectively 2.4 ± 0.2 for the R13 galaxy, and by a factor of 4.0 ± 0.4 for the Eris galaxy.

Table 6.2: Model parameter values recovered by the FitSKIRT radiative transfer fits for the R13 and Eris galaxies. For the R13 galaxy, we list two sets of parameters (head and side). They correspond to two independent radiative transfer fits, based on perpendicular edge-on viewpoints, respectively looking at the head and the side of the bar. For a definition of each parameter, see De Geyter et al. (2014).

Par.	Units	R13 (head)	R13 (side)	Eris
$h_{R,*}$	kpc	4.17 ± 0.38	3.57 ± 0.39	4.14 ± 0.13
$h_{z,*}$	kpc	0.43 ± 0.01	0.40 ± 0.01	0.37 ± 0.01
R_{eff}	kpc	0.93 ± 0.04	1.12 ± 0.08	0.49 ± 0.07
n	—	0.64 ± 0.03	0.80 ± 0.04	6.71 ± 0.48
q	—	0.47 ± 0.01	0.40 ± 0.03	0.56 ± 0.03
$h_{R,\text{d}}$	kpc	9.47 ± 0.69	4.23 ± 0.80	0.35 ± 0.05
$h_{z,\text{d}}$	kpc	0.064 ± 0.005	0.091 ± 0.006	0.095 ± 0.008
M_{d}	$10^6\ M_\odot$	6.26 ± 0.24	7.68 ± 0.33	1.48 ± 0.18
i	deg	89.96 ± 0.02	89.96 ± 0.02	90.04 ± 0.16

6.4 Discussion

The previous work by M00 and M02 cited in Section 6.1, and our results presented in Section 6.2, indicate that fitting a smooth galaxy model to a certain class of basic, quasi-analytical input models recovers the intrinsic dust mass of the input model to within 40% or better. In fact, as evidenced by the close correspondence between recovered and input values listed in Table 6.1, a logarithmic spiral arm perturbation or a clumpy dust distribution seem to have only a modest effect on the structural parameters observed in an optical edge-on view of a disc galaxy, including the derived dust mass.

In contrast, our results presented in Section 6.3 indicate that fitting a smooth galaxy model to more realistic galaxy models, obtained from high-resolution hydrodynamical simulations, underestimates the intrinsic dust mass of the input model by a factor of about three. This is a tantalising result, especially since a factor of roughly the same magnitude has been found in energy balance studies of real edge-on spiral galaxies (Popescu et al. 2000; Misiriotis et al. 2001; Alton et al. 2004; Dasyra et al. 2005; Baes et al. 2010; de Looze et al. 2012; De Looze et al. 2012).

It is tempting to conclude that the level of dust underestimation is driven by the fundamental differences between the input models. The models in M00 and M02, and in

our Section 6.2, are derived from well-behaved, smooth disc models by applying a relatively modest perturbation. For example, the spiral arm perturbation is fully analytical and cancels out exactly when averaged over azimuth. The galaxy models constructed from hydrodynamical simulation snapshots, presented in Section 6.3, feature much more realistic inhomogeneities at a wide range of scales, from large-scale bars and spiral arms to parsec-sized clumps and filaments. These structural complexities may very well be responsible for a higher level of dust underestimation in the radiative transfer fits.

In other words, our modelling suggests that the complex and inhomogeneous structure of galaxies can hide up to three times more dust than is "observed" when the optical images are fitted with smooth axisymmetric models. FIR/submm observations of several spiral galaxies also imply a factor of three times more dust than visible in the optical; this correspondence suggest that the inhomogeneous structure of the ISM possibly is the source of the dust energy balance problem. The recent work by De Looze et al. (2014) supports this hypothesis. They performed a detailed panchromatic radiative transfer modelling of the face-on galaxy M51 with a model that includes the complex geometry as derived from the FUV attenuation map. The model self-consistently reproduces the surface brightness images from UV to submm wavelengths. The face-on analysis is of course less affected by optical depth effects along the line of sight, which may have contributed to this result as well.

We must be careful not to jump to conclusions. First, while a typical factor of about three is found by several teams for different edge-on spiral galaxies (Popescu et al. 2000; Misiriotis et al. 2001; Alton et al. 2004; Dasyra et al. 2005; Baes et al. 2010; de Looze et al. 2012; De Looze et al. 2012), this is by no means an ubiquitous feature. This was shown most recently by De Geyter et al. (2015), who performed the same fitting procedure as presented in this paper on two edge-on spiral galaxies from the sample analysed in De Geyter et al. (2014). For one of the two galaxies, a typical factor-of-three discrepancy is observed between the best fitting FitSKIRT model and the observed FIR/submm SED, whereas for the other galaxy the FitSKIRT model accurately describes the observed spectrum both in absolute values and shape.

Secondly, even for those galaxies in which a dust energy balance problem is encountered, it is up to debate whether this can be ascribed to the same physical scenario. For example, the dust emission excess in the Sombrero galaxy is shown to be compatible with an additional unresolved cold dust reservoir (De Looze et al. 2012), whereas the excess emission in the edge-on spiral UGC 4754 is rather compatible with an additional warmer component, such as expected when linked to recent star formation (Baes et al. 2010, 2011).

Finally, our present study is based on just two simulated spiral galaxies, and each of them has its strengths and weaknesses. In both galaxies we recognise the structures and morphologies of real galaxies, including spiral arms, bars, bulges, star forming regions, and compact clumps. However, the R13 galaxy contains star forming regions that look somewhat artificial, and the galaxy's dust lane is very thin and extended; and the Eris galaxy has a faint and rather fuzzy dust lane that is not visible in the r, i and z bands, which is atypical for real galaxies.

6.5 Conclusion

We set out to shed light on the dust energy balance problem in edge-on spiral galaxies by performing the radiative transfer fitting procedure that has been used previously for studying real galaxies on snapshots obtained from hydrodynamical simulations. These simulated galaxies feature a more realistic inhomogeneous structure than typical quasi-analytical models, and their "true" dust mass is known.

We used two simulated Milky Way-like galaxies as input models. The R13 simulation is a self-consistent hydrodynamical simulation performed with the AMR code RAMSES. The Eris simulation is a zoom-in cosmological simulation performed by the N-body/SPH GASOLINE code. We used our radiative transfer code SKIRT to create mock observational images in the SDSS *ugriz* bands for an edge-on view of both galaxies, and we fitted the parameters of a basic, smooth disc galaxy model to these images with our radiative transfer fitting code FitSKIRT. We found that, for both galaxies, the dust mass is underestimated by a factor of about three. This result is strikingly close to what has been found in previous work by several teams who performed similar analyses for real edge-on spiral galaxies.

In contrast, previous studies have shown that fitting a smooth disc galaxy model to a modestly perturbed, quasi-analytical model (including structures such as spiral arms or dust clumps) can properly recover the "true" dust mass of the input model. To eliminate the possibility that our fitting procedure would behave differently, we repeated our analysis for such basic input models, using exactly the same procedure as for the more realistic input models. We found that our fits could indeed recover the proper dust mass within a narrow margin.

These results suggest that the level of dust underestimation is driven by the fundamental differences between the input models, implying that the complex and inhomogeneous structure of galaxies can hide up to three times more dust than is "observed" when the optical images are fitted with smooth axisymmetric models. Although our analysis is too anecdotal to be conclusive, we would still argue that this effect may help explain the dust energy balance problem, at least in part and for certain types of galaxies.

7 Summary and outlook

The main objectives of this thesis were twofold. Firstly, we wanted to implement two different hierarchical grid structures in the 3D Monte Carlo radiative transfer SKIRT, and to investigate the efficiency of different grid traversal methods and grid construction criteria. The second objective was to use these advanced grids to investigate the dust energy balance problem in spiral galaxies using radiative transfer simulations based on high-resolution hydrodynamics simulations. In this final Chapter we summarise the results obtained in this thesis and present some possibilities for future research.

7.1.1 Hierarchical grids in SKIRT

In Chapter 3 we critically investigate the use of octree and *k*-d tree grids in the context of Monte Carlo radiative transfer. Both types of hierarchical grids can automatically refine the resolution in higher density regions without the need to create undesirably small dust cells in low density regions. For both octree and *k*-d tree grids, we consider two different tree construction algorithms (regular and barycentric subdivision), and in order to compare the efficiency of the grids, we consider three different test models and four different quality metrics.

Our first conclusion is that an average random path through a regular grid crosses fewer cells than the same path through the equivalent barycentric grid. Surprisingly, this conclusion turns out to be valid in all test cases, even for simulations in which the regular grid contains more grid cells. This implies that barycentric grids are less efficient for the purpose of Monte Carlo radiative transfer than the corresponding regular grids. Furthermore, we find that, for a given required mass resolution, *k*-d tree grids require only half the number of cells compared to the corresponding octree grids. Moreover, for the same number of grid cells, the *k*-d tree is characterised by a better discretisation accuracy. Therefore, we recommend the use of *k*-d trees with regular subdivision in Monte Carlo simulations as an alternative to the more commonly used octrees.

In Chapter 4 we focus on the traversal of photon packages through hierarchical octree and *k*-d tree grids. As the traversal through the dusty medium is the most time-consuming part of most Monte Carlo radiative transfer simulations, identifying the most efficient method is crucial for the overal efficiency. Inspired by the methods used in the computer graphics community, we have implemented three traversal methods for hierarchical trees (the top-down method, the neighbour list search method, and the bookkeeping method) in SKIRT. These methods can be used for both octrees and

k-d trees, with both regular and barycentric subdivision. The efficiency of these three methods is tested using the test models introduced in Chapter 3.

We find that the neighbour list method is consistently the most efficient method to calculate paths through an octree or a *k*-d tree, with total simulation run times about 20% shorter than for the other two methods. This is mainly achieved by ordering the neighbour lists according to decreasing overlap area, which makes the search almost trivial in the majority of the cases. We also find that simulations on barycentric grids are always slower than simulations on the corresponding regular grids, confirming the results from Chapter 3, which were only based on the average number of cells along a path. We conclude that the combination of regular grid subdivision and neighbour list grid traversal is the ideal combination for efficient Monte Carlo radiative transfer simulations.

Chapter 5 is devoted to a search for the optimal subdivision stopping criteria that should be used during the construction of a hierarchical grid in a Monte Carlo simulation. In the ideal case, the grid subdivision should be optimised to discretise the intensity of the radiation field, but this quantity is not known at the beginning of the radiative transfer simulation. The most simple alternative, and the one most often applied in the literature, is a criterion based on the dust density field, but this also has a number of drawbacks. In an attempt to define a better alternative, we consider three different node subdivision stopping criteria, based on mass, optical depth, and density gradient thresholds, respectively. We test and compare them using our previously introduced test models and quality metrics.

We find that an optical depth criterion alone is not a useful alternative to the more standard mass threshold, as the resulting grids have a poor accuracy. Both criteria can be combined, however. In the optimal combination, this can lead to a 20% reduction in the number of cells needed to reach a certain grid quality. We provide a simple approximate recipe for this optimal combination. An additional density gradient threshold criterion can be added to solve the problem of poorly resolving sharp edges and strong density gradients.

Based on these tests, we can easily formulate general recommendations for the use of hierarchical grids in 3D Monte Carlo radiative transfer simulations. We advocate

- the use of *k*-d tree grids as an alternative to the more popular octrees,
- regular subdivision instead of barycentric subdivision, even though barycentric grids sometimes need fewer cells for the same subdivision criteria,
- a combination of mass and optical depth thresholds as grid subdivision criteria,
- the neighbour list method to traverse the grid.

To the best of our knowledge, this work is the first one devoted to a detailed analysis of the use of hierarchical grids in Monte Carlo radiative transfer. But it is definitely not the last word, and there are still various possible improvements and extensions possible.

One obvious extension is the investigation to more general grids. The hierarchical octree and k-d tree grids that we have considered here constitute only a small corner of the entire zoo of possible grid structures that could be considered. There is a large variety of other space partitioning structures, each with their own strengths and weaknesses. Particularly interesting are unstructured grids based on Voronoi or Delaunay tessellation. These grids have existed for a long time, but they have recently gained popularity thanks to the development of hydrodynamics codes that operate on them (Xu 1997; Springel 2010; Duffell and MacFadyen 2011). Radiative transfer on such grids has been shown to be possible (Paardekooper et al. 2010; Brinch and Hogerheijde 2010; Camps et al. 2013). While unstructured grids can probably not compete with hierarchical grids in terms of grid traversal, they could be more efficient in some situations, e.g. in simulations where in-cell operations (such as the calculation of the temperature distribution or the dust emission profile), rather than grid traversal, are the most expensive operation.

Another possible future investigation is the search for better criteria for the grid construction. As already indicated, the ideal grid for a Monte Carlo simulation does not only depend on the dust density, but also on the mean intensity of the radiation field, which can only be determined through the radiative transfer simulation itself. Possible ways to deal with this include using knowledge about the source function when constructing the dust grid (Stamatellos and Whitworth 2005), or refining the grid structure based on low-resolution pre-calculations (Niccolini and Alcolea 2006). Probably the most general approach is using an iterative scheme: start with an initial grid structure derived from the dust density field (based on total mass and/or density gradient), determine the radiation field in every cell using the radiative transfer simulation, and iteratively refine/redetermine the grid based on the properties of the cell-to-cell variance of the radiation field. An exercise of this kind based on realistic 3D models, and a possible derivation of approximate subdivision criteria that can avoid such an iterative process, would be most interesting.

7.1.2 The dust energy balance problem

The second part of this thesis focuses on the so-called dust energy balance problem in edge-on spiral galaxies. The essence of this problem is an inconsistency between the dust seen in absorption at optical wavelengths and the dust seen in emission in

the FIR/submm. More specifically, several radiative transfer models that successfully explain the optical extinction in edge-on spiral galaxies underestimate the observed FIR/submm fluxes by a factor of about three.

In Chapter 6 we use two Milky Way-like galaxies produced by high-resolution hydrodynamical simulations to search for a possible explanation for this dust energy balance problem. We use SKIRT to create mock optical edge-on views of the simulated galaxies, and subsequently fit the parameters of a basic spiral galaxy model to these mock images using the fitting code FitSKIRT. This basic model is similar to the ones that are used to model real galaxies, and consists of a smooth axisymmetric Sérsic bulge and an exponential disc for the stars, and a second exponential disc for the dust. We find that the dust mass recovered by the fitted models is about three times smaller than the known dust mass of the hydrodynamical input models. On the other hand, fitting the same basic model to less complex input models (e.g., a smooth exponential disc with a spiral perturbation or with random clumps), we do recover the dust mass of the input model almost perfectly. The conclusion is that the complex asymmetries and the inhomogeneous structure of simulated galaxies are apparently more efficient at hiding dust than the rather contrived geometries in typical quasi-analytical models. Small and large-scale asymmetries might hence contribute to explain the dust energy balance problem.

However, we must be careful not to jump to conclusions, as there are a number of arguments that suggest that small and large-scale asymmetries are not the ultimate answer to the dust energy balance problem in all galaxies. Not all edge-on galaxies show an inconsistency between the optical and FIR/submm dust mass, and it is still under debate whether the dust energy balance problem can be ascribed to the same physical scenario for all galaxies where it is observed. More work needs to be done to clarify this situation.

A first way to extend our study is the use of a larger sample of even more realistic simulated galaxies. In Chapter 6 we only considered two simulated spiral galaxies, and both of them have some characteristics that deviate from real galaxies (in particular, the characteristics of the dust lane in both galaxies do not seem to correspond to those in real galaxies). A similar but more systematic study based on a larger sample of simulated galaxies could minimise some of the potential biases that we might have encountered. Fortunately, hydrodynamical simulations of spiral galaxies in a cosmological context are becoming ever more realistic, even on a relatively short timescale, so a follow-up study could probably be done in the next few years. A particularly interesting development is the possibility to actually simulate the dust component in galaxies in a self-consistent way (Bekki 2015).

Besides a more detailed theoretical study, there is a strong need for a better observational understanding of the dust energy balance problem in nearby galaxies. Since fitting radiative transfer models to images is a very computationally expensive job, most dust energy balance studies have concentrated on a single or at most a very modest set of galaxies. Each of these studies typically used different codes, different input data and different assumptions on geometry, stellar populations and dust properties. We require a sufficiently large set of galaxies with the needed multi-wavelength data available and modelled in a homogeneous way, such that physical effects can be disentangled from effects connected to the modelling approach. A first step to such a systematic investigation is the work by De Geyter et al. (2014, 2015). A very promising sample for a systematic dust energy balance study is the combined sample of HEROES (Verstappen et al. 2013) and NHEMESES (Holwerda et al. 2012) galaxies. This joint sample contains 19 nearby edge-on spiral galaxies with sufficient spatial resolution and the availability of a large multi-wavelength data set. A systematic and uniform modelling of this sample using automated modelling techniques will hopefully provide new insights into this fascinating problem.

7.2.1 Inleiding

Melkwegstelsels bevatten miljarden sterren en worden algemeen beschouwd als de bouwstenen van het Heelal. Ze zijn echter meer dan enkel een verzameling sterren: tussen de sterren door bevindt zich een complexe mengeling van atomen, moleculen en ionen: het zogenaamde interstellaire medium. Een klein gedeelte van dit interstellaire medium bestaat uit minuscule stukjes vaste materie, die we interstellair stof noemen. Interstellair stof is lang beschouwd als een hinderpaal voor sterrenkundigen, aangezien het heel efficiënt sterlicht kan absorberen en verstrooien. Tegenwoordig wordt interstellair stof beschouwd als een interessante en dynamische component van het interstellair medium die een onmiskenbare rol vervult in verschillende astrofysische processen, zoals stervorming en planeetvorming.

In dit proefschrift concentreren we ons op stralingsoverdracht door interstellair stof in melkwegstelsels, d.w.z. de interactie tussen stofdeeltjes en sterlicht. Ongeveer de helft van alle sterlicht uitgezonden in het Heelal wordt door stof geabsorbeerd of verstrooid. Indien we de waargenomen beelden van melkwegstelsels correct willen interpreteren, dan is het noodzakelijk om de effecten van stof (in de eerste plaats absorptie, verstrooiing en thermische emissie) op een correcte manier in rekening te brengen. Dit vereist een oplossing van de stralingsoverdrachtsvergelijking, een complexe, niet-lineaire partiële integro-differentiaalvergelijking. Dit kan enkel via speciale numerieke technieken, waarvan de Monte Carlo methode de meest populaire is. SKIRT is een Monte Carlo stralingsoverdrachtscode die specifiek ontworpen is om de effecten van interstellair stof te onderzoeken op de schaal van melkwegstelsels.

Bij Monte Carlo stralingsoverdrachtssimulaties worden miljarden fotonpakketjes individueel gevolgd tijdens hun doortocht doorheen het stofrijke medium. Hiervoor wordt dit medium gediscretiseerd op een rooster, m.a.w. het medium wordt ingedeeld in een groot aantal cellen. Een verstandige keuze van dit rooster is fundamenteel, aangezien de berekening van de doorkruising van de verschillende cellen het meest tijdrovende deel is van een Monte Carlo simulatie. In het bijzonder is het nuttig over roosters te beschikken waarvan de resolutie kan variëren van plaats tot plaats, zodat er voldoende kleine cellen kunnen worden gebruikt waar een hoge resolutie nodig is, terwijl grotere cellen kunnen worden gebruikt waar dit voldoende is.

Dit proefschrift had twee doelstellingen voor ogen. Een eerste doel was om twee verschillende hiërarchische roosterstructuren in de 3D stralingsoverdrachtscode SKIRT in te bouwen, en om de efficiëntie te onderzoeken van verschillende manieren om

deze roosters op te bouwen en te doorkruisen. De tweede doelstelling was om het zogenaamde probleem van de energiebalans van het stof in melkwegstelsels te onderzoeken aan de hand van deze geavanceerde roosterstructuren in SKIRT en state-of-the-art hydrodynamische simulaties.

7.2.2 Hiërarchische roosters in SKIRT

In Hoofdstuk 3 onderzoeken we op kritische wijze het gebruik van hiërarchische octree en *k*-d tree roosters in de context van Monte Carlo stralingsoverdracht. Beide roostertypes kunnen automatisch de ruimtelijke resolutie verfijnen in gebieden met een hogere dichtheid, zonder dat er ongewenst kleine cellen worden aangemaakt in gebieden met een lage dichtheid. Voor zowel octrees als *k*-d trees beschouwen we twee verschillende constructie-algoritmen (gebaseerd op een reguliere en een barycentrische onderverdeling van de cellen). Om de efficiëntie van de roosters te kunnen vergelijken, beschouwen we drie verschillende testmodellen en vier verschillende kwaliteitskenmerken.

Onze eerste conclusie is dat een gemiddeld pad doorheen een regulier rooster minder cellen doorkruist dan hetzelfde pad doorheen een barycentrisch rooster. Het is verwonderlijk dat deze conclusie standhoudt voor alle testmodellen, zelfs voor diegene waarin het reguliere rooster meer cellen bevat dan het equivalente barycentrische rooster. Deze vaststelling impliceert dat barycentrische roosters minder efficiënt zijn voor Monte Carlo stralingsoverdracht dan de corresponderende reguliere roosters. Verder vinden we dat, voor een gegeven massaresolutie, *k*-d tree roosters slechts half zoveel cellen nodig hebben als de equivalente octree roosters. Bovendien scoren *k*-d tree roosters voor een vast aantal cellen beter op het gebied van nauwkeurigheid. De algemene conclusie van Hoofdstuk 3 is dan ook dat we het gebruik van *k*-d tree roosters met reguliere onderverdeling sterk aanraden voor Monte Carlo stralingsoverdracht als alternatief voor de meer populaire octree roosters.

In Hoofdstuk 4 concentreren we ons op de doorkruising van fotonpakketjes doorheen hiërarchische octree en *k*-d tree roosters. Aangezien de berekening van de paden van individuele fotonpakketten het meest tijdrovende aspect is van de meeste Monte Carlo stralingsoverdrachtssimulaties, is het identificeren van het meest efficiënte algoritme belangrijk voor de algemene efficiëntie van de code. Geïnspireerd door methoden die gebruikt worden in de computerwetenschappen en computer gaming, hebben we drie verschillende methoden om roosters te doorkruisen in SKIRT geïmplementeerd: de top-down methode, de lijst-van-buren methode, en de boekhoudingsmethode. Elk van deze methoden kan gebruikt worden voor zowel octrees als *k*-d trees, en voor zowel reguliere als barycentrische roosters. De efficiëntie van deze methoden werd getest aan

de hand van de testmodellen die in Hoofdstuk 3 werden ingevoerd.

Het resultaat van dit onderzoek is dat de lijst-van-buren methode steeds de meest efficiënte methode blijkt te zijn om een octree of hiërarchisch rooster te doorkruisen. Simulaties met deze methode zijn gemiddeld 20% sneller dan simulaties met de andere twee methoden. Het cruciale aspect dat deze efficiëntie mogelijk maakt is een rangschikking van de lijst van buren zodanig dat de buren met de grootste overlap eerst in de lijst staan, waardoor de zoektocht naar de correcte cel bijna triviaal is in de meeste gevallen. We vinden ook dat simulaties op barycentrische roosters steeds langzamer zijn dan simulaties op de corresponderende reguliere roosters. Deze bevinding bevestigt de voorlopige conclusie van Hoofdstuk 3, die enkel was gebaseerd op het gemiddeld aantal cellen dat per pad wordt doorkruisd. We besluiten dat de combinatie van een rooster met reguliere onderverdeling en een doorkruising op basis van de lijst-van-buren methode de ideale combinatie is voor efficiënte Monte Carlo stralingsoverdrachtssimulaties.

Hoofdstuk 5 is gewijd aan de zoektocht naar de optimale criteria om de onderverdeling van cellen te stoppen tijdens het opstellen van een rooster voor Monte Carlo simulaties. In een ideale wereld zou de onderverdeling van de cellen bepaald worden aan de hand van de intensiteit van het stralingsveld, maar dit is nu exact de grootheid die we willen bepalen door middel van een stralingsoverdrachtssimulatie en is dus per definitie ongekend *a priori*. Het eenvoudigste alternatief, en hetgeen ook in bestaande codes wordt toegepast, is een criterium gebaseerd op de dichtheid. Dit heeft echter ook enkele nadelen. In een poging om een beter alternatief te vinden beschouwen we drie verschillende criteria om het onderverdelen van cellen in een hiërarchisch grid te stoppen, gebaseerd op respectievelijk de totale massa, de optische diepte en de dichtheidsgradiënt in een cel. We testen en vergelijken deze drie criteria op basis van de testmodellen en de kwaliteitskenmerken die we tevoren hebben ingevoerd.

We vinden dat het criterium gebaseerd op optische diepte alleen geen volwaardig alternatief vormt voor het standaardcriterium gebaseerd op massa, aangezien de roosters die op dit criterium zijn gebaseerd zwak scoren op het gebied van nauwkeurigheid. Dit wil echter niet zeggen dat dit criterium waardeloos is, aangezien beide criteria kunnen worden gecombineerd. Bij een optimale combinatie van beide criteria, waarvoor we ook een eenvoudig benaderend recept formuleren, kan dit leiden tot een reductie van 20% in het aantal cellen dat nodig is om aan een bepaalde kwaliteitseis te voldoen. We voeren tenslotte ook nog een derde eenvoudig criterium in dat met succes het probleem van scherpe randen en grote dichtheidsgradiënten kan oplossen. Ook dit criterium kan probleemloos worden gecombineerd met de twee andere.

Gebaseerd op al deze testresultaten, kunnen we een aantal aanbevelingen formuleren

voor het gebruik van hiërarchische roosters in 3D Monte Carlo stralingsoverdrachtssimulaties. Met name bevelen we het volgende aan

- het gebruik van *k*-d tree roosters als alternatief voor de meer populaire octrees,
- reguliere onderverdeling in plaats van barycentrische onderverdeling, zelfs al vereisen barycentrische roosters soms minder cellen dan de equivalente reguliere roosters,
- een combinatie van criteria gebaseerd op massa en optische diepte om de onderverdeling van de cellen bij het opstellen van het rooster te stoppen,
- de methode van de lijst-van-buren om het rooster te doorkruisen.

7.2.3 De energiebalans van het interstellair stof

Het tweede deel van dit proefschrift buigt zich over het zogenaamde probleem van de energiebalans van het interstellair stof in spiraalstelsels op hun kant. De essentie van dit probleem is een inconsistentie tussen de hoeveelheid stof die we kunnen zien in absorptie bij optische golflengten en de hoeveelheid stof die we zien in emissie in het verre infrarood. Meer specifiek zien we dat, voor verschillende nabijgelegen spiraalgalaxieën, stralingsoverdrachtsmodellen die de optische extinctie met succes kunnen reproduceren de waargenomen emissie in het verre infrarood onderschatten met een factor van ongeveer drie.

In Hoofdstuk 6 gebruiken we twee gesimuleerde modellen voor spiraalgalaxieën die op onze Melkweg lijken om een mogelijke verklaring voor het probleem van de energiebalans van het stof te onderzoeken. Met behulp van de SKIRT code, en de hiërarchische grids die daarin zijn geïmplementeerd, creëren we artificiële optische beelden van deze twee gesimuleerde galaxieën in zij-aanzicht. Vervolgens fitten we een stralingsoverdrachtsmodel aan deze beelden met behulp van de FitSKIRT code. Het model waarvan we de parameters bepalen is analoog aan de modellen die gebruikt worden bij stralingsoverdrachtsmodellering van echte spiraalgalaxieën, en bestaat uit een sferoïdale Sérsic bult en een exponentiële schijf voor de sterren, en een tweede exponentiële schijf voor het interstellaire stof. De totale massa aan interstellair stof die door deze modellering bepaald wordt is ongeveer drie keer kleiner dan de originele massa stof in de oorspronkelijke modellen. We hebben dezelfde oefening ook gedaan voor minder complexe semi-analytische input modellen (smoothe modellen met een spiraalarm, of modellen met een klonterige structuur), en hier vinden we wel de exacte input waarde voor de hoeveelheid stof terug. De les die we hieruit trekken is dat de complexe asymmetrie en de inhomogene structuur van realistische hydrodynamisch gesimuleerde galaxieën blijkbaar efficiënt stof kunnen verbergen in optische beelden,

terwijl minder realistische quasi-analytische modellen dat niet kunnen.

Klein- en grootschalige asymmetrieën in de verdeling van het interstellaire medium van spiraalgalaxieën vormen dus een bijdrage tot de verklaring van de energiebalans van het stof in melkwegstelsels. Het dient echter te worden benadrukt dat het hoogstwaarschijnlijk niet de enige verklaring is, en dat verder onderzoek, zowel op theoretisch als observationeel vlak, noodzakelijk is om dit probleem duidelijk in kaart te brengen en mogelijke verklaringen te onderzoeken.

Refereed publications

Most of the work presented in this thesis has been published in the following refereed publications:

Baes M., Verstappen J., De Looze I., Fritz J., Saftly W., Vidal E., Stalevski M., Valcke S.
Efficient three-dimensional NLTE dust radiative transfer with SKIRT
The Astrophysical Journal Supplement, **196**, 22 (2011)

Saftly W., Camps P., Baes M., Gordon K. D., Vandewoude S., Rahimi A., Stalevski M.
Using hierarchical octrees in Monte Carlo radiative transfer simulations
Astronomy & Astrophysics, **554**, A10 (2013)

Camps P., Baes M., Saftly W.
Using 3D Voronoi grids in radiative transfer simulations
Astronomy & Astrophysics, **560**, A35 (2013)

Saftly W., Baes M., Camps P.
Hierarchical octree and k-d tree grids for 3D radiative transfer simulations
Astronomy & Astrophysics, **561**, A77 (2014)

Saftly W., Baes M., De Geyter G., Camps P., Renaud F., Guedes J., De Looze I.
Large and small-scale structures and the dust energy balance problem in spiral galaxies
Astronomy & Astrophysics, **576**, A31 (2015)

Gentile G., Tydtgat C., Baes M., De Geyter G., Koleva M., Angus G. W., de Blok W. J. G., Saftly W., Viaene S.
Disk mass and disk heating in the spiral galaxy NGC 3223
Astronomy & Astrophysics, **576**, A57 (2015)

Bibliography

Abdikamalov, E., Burrows, A., Ott, C. D., Löffler, F., O'Connor, E., Dolence, J. C., and Schnetter, E. (2012). A New Monte Carlo Method for Time-dependent Neutrino Radiation Transport. *ApJ*, 755:111.

Agate, M., Grimsdale, R. L., and Lister, P. F. (1991). The hero algorithm for ray-tracing octrees. In *Advances in Computer Graphics Hardware IV (Eurographic 89 Workshop)*, page 61.

Agertz, O., Teyssier, R., and Moore, B. (2011). The formation of disc galaxies in a ΛCDM universe. *MNRAS*, 410:1391.

Alton, P. B., Xilouris, E. M., Bianchi, S., Davies, J., and Kylafis, N. (2000). Dust properties of external galaxies; NGC 891 revisited. *A&A*, 356:795.

Alton, P. B., Xilouris, E. M., Misiriotis, A., Dasyra, K. M., and Dumke, M. (2004). The emissivity of dust grains in spiral galaxies. *A&A*, 425:109.

Amanatides, J. and Woo, A. (1987). A fast voxel traversal algorithm for ray tracing. In *In Eurographics 87*, page 3.

Baes, M. (2008). Smart detectors for Monte Carlo radiative transfer. *MNRAS*, 391:617.

Baes, M. and Camps, P. (2015). Continuous scattering: a new acceleration technique in Monte Carlo radiative transfer simulations. *A&A*.

Baes, M., Davies, J. I., Dejonghe, H., Sabatini, S., Roberts, S., Evans, R., Linder, S. M., Smith, R. M., and de Blok, W. J. G. (2003). Radiative transfer in disc galaxies - III. The observed kinematics of dusty disc galaxies. *MNRAS*, 343:1081.

Baes, M. and Dejonghe, H. (2000). Kinematics of elliptical galaxies with a diffuse dust component. *MNRAS*, 313:153–164.

Baes, M. and Dejonghe, H. (2001a). Dark Matter Halos around Elliptical Galaxies: How Reliable Is the Stellar Kinematical Evidence? *ApJL*, 563:L19.

Baes, M. and Dejonghe, H. (2001b). Radiative transfer in disc galaxies - I. A comparison of four methods to solve the transfer equation in plane-parallel geometry. *MNRAS*, 326:722.

Baes, M. and Dejonghe, H. (2001c). Radiative transfer in disc galaxies - II. The influence of scattering and geometry on the attenuation curve. *MNRAS*, 326:733.

Baes, M. and Dejonghe, H. (2002). Kinematics of elliptical galaxies with a diffuse dust component - III. A Monte Carlo approach to include the effects of scattering. *MNRAS*, 335:441.

Baes, M., Fritz, J., Gadotti, D. A., Smith, D. J. B., Dunne, L., da Cunha, E., Amblard, A., Auld, R., Bendo, G. J., Bonfield, D., Burgarella, D., Buttiglione, S., Cava, A., Clements, D., Cooray, A., Dariush, A., de Zotti, G., Dye, S., Eales, S., Frayer, D., Gonzalez-Nuevo, J., Herranz, D., Ibar, E., Ivison, R., Lagache, G., Leeuw, L., Lopez-Caniego, M., Jarvis, M., Maddox, S., Negrello, M., Michałowski, M., Pascale, E., Pohlen, M., Rigby, E., Rodighiero, G., Samui, S., Serjeant, S., Temi, P., Thompson, M., van der Werf, P., Verma, A., and Vlahakis, C. (2010). Herschel-ATLAS: The dust energy balance in the edge-on spiral galaxy UGC 4754. *A&A*, 518:L39.

Baes, M., Verstappen, J., De Looze, I., Fritz, J., Saftly, W., Vidal Pérez, E., Stalevski, M., and Valcke, S. (2011). Efficient Three-dimensional NLTE Dust Radiative Transfer with SKIRT. *ApJS*, 196:22.

Baes, M., Vidal, E., Van Winckel, H., Deroo, P., and Gielen, C. (2007). Efficient Radiative Transfer in a Circumstellar Disk Environment. *Baltic Astronomy*, 16:92.

Barnes, J. and Hut, P. (1986). A hierarchical O(N log N) force-calculation algorithm. *Nature*, 324:446.

Bekki, K. (2015). Cosmic Evolution of Dust in Galaxies: Methods and Preliminary Results. *ApJ*, 799:166.

Bentley, J. L. (1975). Multidimensional binary search trees used for associative searching. *Commun. ACM*, 18:509.

Bianchi, S. (2007). The dust distribution in edge-on galaxies. Radiative transfer fits of V and K'-band images. *A&A*, 471:765.

Bianchi, S. (2008). Dust extinction and emission in a clumpy galactic disk. An application of the radiative transfer code TRADING. *A&A*, 490:461.

Bianchi, S., Ferrara, A., Davies, J. I., and Alton, P. B. (2000). Effects of clumping on the observed properties of dusty galaxies. *MNRAS*, 311:601.

Bianchi, S., Ferrara, A., and Giovanardi, C. (1996). Monte Carlo Simulations of Dusty Spiral Galaxies: Extinction and Polarization Properties. *ApJ*, 465:127.

Blum, J., Wurm, G., Kempf, S., Poppe, T., Klahr, H., Kozasa, T., Rott, M., Henning, T., Dorschner, J., Schräpler, R., Keller, H. U., Markiewicz, W. J., Mann, I., Gustafson, B. A., Giovane, F., Neuhaus, D., Fechtig, H., Grün, E., Feuerbacher, B., Kochan, H., Ratke, L., El Goresy, A., Morfill, G., Weidenschilling, S. J., Schwehm, G., Metzler, K., and Ip, W.-H. (2000). Growth and Form of Planetary Seedlings: Results from a Microgravity Aggregation Experiment. *Physical Review Letters*, 85:2426.

Boissé, P. (1990). Radiative transfer inside clumpy media - The penetration of UV photons inside molecular clouds. *A&A*, 228:483.

Bournaud, F., Elmegreen, B. G., and Elmegreen, D. M. (2007). Rapid Formation of Exponential Disks and Bulges at High Redshift from the Dynamical Evolution of Clump-Cluster and Chain Galaxies. *ApJ*, 670:237.

Bournaud, F., Elmegreen, B. G., and Martig, M. (2009). The Thick Disks of Spiral Galaxies as Relics from Gas-rich, Turbulent, Clumpy Disks at High Redshift. *ApJL*, 707:L1.

Bouwman, J., Henning, T., Hillenbrand, L. A., Meyer, M. R., Pascucci, I., Carpenter, J., Hines, D., Kim, J. S., Silverstone, M. D., Hollenbach, D., and Wolf, S. (2008). The Formation and Evolution of Planetary Systems: Grain Growth and Chemical Processing of Dust in T Tauri Systems. *ApJ*, 683:479.

Brinch, C. and Hogerheijde, M. R. (2010). LIME - a flexible, non-LTE line excitation and radiation transfer method for millimeter and far-infrared wavelengths. *A&A*, 523:A25.

Bruzual, G. and Charlot, S. (2003). Stellar population synthesis at the resolution of 2003. *MNRAS*, 344:1000.

Bruzual, G. A., Magris, G., and Calvet, N. (1988). A model for the effects of dust on the spectra of disk galaxies. I - General treatment. *ApJ*, 333:673.

Bryan, G. L., Norman, M. L., O'Shea, B. W., Abel, T., Wise, J. H., Turk, M. J., Reynolds, D. R., Collins, D. C., Wang, P., Skillman, S. W., Smith, B., Harkness, R. P., Bordner, J., Kim, J.-h., Kuhlen, M., Xu, H., Goldbaum, N., Hummels, C., Kritsuk, A. G., Tasker, E., Skory, S., Simpson, C. M., Hahn, O., Oishi, J. S., So, G. C., Zhao, F., Cen, R., Li, Y., and Enzo Collaboration (2014). ENZO: An Adaptive Mesh Refinement Code for Astrophysics. *ApJS*, 211:19.

Burstedde, C., Wilcox, L. C., and Ghattas, O. (2011). `p4est`: Scalable algorithms for parallel adaptive mesh refinement on forests of octrees. *SIAM J. Sci. Comput.*, 33:1103.

Byun, Y. I., Freeman, K. C., and Kylafis, N. D. (1994). Diagnostics of dust content in spiral galaxies: Numerical simulations of radiative transfer. *ApJ*, 432:114.

Calzetti, D. (2008). Star Formation Rate Determinations. In *Pathways Through an Eclectic Universe*, volume 390, page 121.

Camps, P. and Baes, M. (2015). SKIRT: An advanced dust radiative transfer code with a user-friendly architecture. *Astronomy and Computing*, 9:20.

Camps, P., Baes, M., and Saftly, W. (2013). Using 3D Voronoi grids in radiative transfer simulations. *A&A*, 560:A35.

Cashwell, E. D. and Everett, C. J. C. J. (1959). *A practical manual on the Monte Carlo method for random walk problems*. Pergamon.

Chandrasekhar, S. (1960). *Radiative transfer*. Oxford, Clarendon Press.

Ciardi, B., Ferrara, A., Marri, S., and Raimondo, G. (2001). Cosmological reionization around the first stars: Monte Carlo radiative transfer. *MNRAS*, 324:381.

Ciesla, L., Boquien, M., Boselli, A., Buat, V., Cortese, L., Bendo, G. J., Heinis, S., Galametz, M., Eales, S., Smith, M. W. L., Baes, M., Bianchi, S., de Looze, I., di Serego Alighieri, S., Galliano, F., Hughes, T. M., Madden, S. C., Pierini, D., Rémy-Ruyer, A., Spinoglio, L., Vaccari, M., Viaene, S., and Vlahakis, C. (2014). Dust spectral energy distributions of nearby galaxies: an insight from the Herschel Reference Survey. *A&A*, 565:A128.

Code, A. D. (1973). Radiative Transfer in Circumstellar Dust Clouds. *IAU Symposium*, 52:505.

Code, A. D. and Whitney, B. A. (1995). Polarization from scattering in blobs. *ApJ*, 441:400.

Compiègne, M., Verstraete, L., Jones, A., Bernard, J.-P., Boulanger, F., Flagey, N., Le Bourlot, J., Paradis, D., and Ysard, N. (2011). The global dust SED: tracing the nature and evolution of dust with DustEM. *A&A*, 525:A103.

Cortese, L., Ciesla, L., Boselli, A., Bianchi, S., Gomez, H., Smith, M. W. L., Bendo, G. J., Eales, S., Pohlen, M., Baes, M., Corbelli, E., Davies, J. I., Hughes, T. M., Hunt, L. K., Madden, S. C., Pierini, D., di Serego Alighieri, S., Zibetti, S., Boquien, M., Clements, D. L., Cooray, A., Galametz, M., Magrini, L., Pappalardo, C., Spinoglio, L., and Vlahakis, C. (2012). The dust scaling relations of the Herschel Reference Survey. *A&A*, 540:A52.

Cox, P., Krips, M., Neri, R., Omont, A., Güsten, R., Menten, K. M., Wyrowski, F., Weiß, A., Beelen, A., Gurwell, M. A., Dannerbauer, H., Ivison, R. J., Negrello, M., Aretxaga, I., Hughes, D. H., Auld, R., Baes, M., Blundell, R., Buttiglione, S., Cava, A., Cooray, A., Dariush, A., Dunne, L., Dye, S., Eales, S. A., Frayer, D., Fritz, J., Gavazzi, R., Hopwood, R., Ibar, E., Jarvis, M., Maddox, S., Michałowski, M., Pascale, E., Pohlen, M., Rigby, E., Smith, D. J. B., Swinbank, A. M., Temi, P., Valtchanov, I., van der Werf, P., and de Zotti, G. (2011). Gas and Dust in a Submillimeter Galaxy at z = 4.24 from the Herschel Atlas. *ApJ*, 740:63.

Dale, D. A., Aniano, G., Engelbracht, C. W., Hinz, J. L., Krause, O., Montiel, E. J., Roussel, H., Appleton, P. N., Armus, L., Beirão, P., Bolatto, A. D., Brandl, B. R., Calzetti, D., Crocker, A. F., Croxall, K. V., Draine, B. T., Galametz, M., Gordon, K. D., Groves, B. A., Hao, C.-N., Helou, G., Hunt, L. K., Johnson, B. D., Kennicutt, R. C., Koda, J., Leroy, A. K., Li, Y., Meidt, S. E., Miller, A. E., Murphy, E. J., Rahman, N., Rix, H.-W., Sandstrom, K. M., Sauvage, M., Schinnerer, E., Skibba, R. A., Smith, J.-D. T., Tabatabaei, F. S., Walter, F., Wilson, C. D., Wolfire, M. G., and Zibetti, S. (2012). Herschel Far-infrared and Submillimeter Photometry for the KINGFISH Sample of nearby Galaxies. *ApJ*, 745:95.

Dasyra, K. M., Xilouris, E. M., Misiriotis, A., and Kylafis, N. D. (2005). Is the Galactic submillimeter dust emissivity underestimated? *A&A*, 437:447.

De Cia, A., Ledoux, C., Savaglio, S., Schady, P., and Vreeswijk, P. M. (2013). Dust-to-metal ratios in damped Lyman-α absorbers. Fresh clues to the origins of dust and optical extinction towards γ-ray bursts. *A&A*, 560:A88.

De Geyter, G., Baes, M., Camps, P., Fritz, J., De Looze, I., Hughes, T. M., Viaene, S., and Gentile, G. (2014). The distribution of interstellar dust in CALIFA edge-on galaxies via oligochromatic radiative transfer fitting. *MNRAS*, 441:869.

De Geyter, G., Baes, M., De Looze, I., Bendo, G. J., Bourne, N., Camps, P., Cooray, A., De Zotti, G., Dunne, L., Dye, S., Fritz, J., Furlanetto, C., Gentile, G., Ivison, R. J., Maddox, S., Michałowski, M., Smith, M. W. L., Hughes, T. M., and Viaene, S. (2015). Dust energy balance study of two edge-on spiral galaxies in Herschel-ATLAS survey. *MNRAS*, submitted.

De Geyter, G., Baes, M., Fritz, J., and Camps, P. (2013). FitSKIRT: genetic algorithms to automatically fit dusty galaxies with a Monte Carlo radiative transfer code. *A&A*, 550:A74.

de Looze, I., Baes, M., Bendo, G. J., Ciesla, L., Cortese, L., de Geyter, G., Groves, B., Boquien, M., Boselli, A., Brondeel, L., Cooray, A., Eales, S., Fritz, J., Galliano, F., Gentile, G., Gordon, K. D., Hony, S., Law, K.-H., Madden, S. C., Sauvage, M., Smith, M. W. L., Spinoglio, L., and Verstappen, J. (2012). The dust energy balance in the edge-on spiral galaxy NGC 4565. *MNRAS*, 427:2797.

De Looze, I., Baes, M., Fritz, J., and Verstappen, J. (2012). Panchromatic radiative transfer modelling of stars and dust in the Sombrero galaxy. *MNRAS*, 419:895.

De Looze, I., Fritz, J., Baes, M., Bendo, G. J., Cortese, L., Boquien, M., Boselli, A., Camps, P., Cooray, A., Cormier, D., Davies, J. I., De Geyter, G., Hughes, T. M., Jones, A. P., Karczewski, O. ., Lebouteiller, V., Lu, N., Madden, S. C., Rémy-Ruyer, A., Spinoglio, L., Smith, M. W. L., Viaene, S., and Wilson, C. D. (2014). High-resolution, 3D radiative transfer modeling. I. The grand-design spiral galaxy M 51. *A&A*, 571.

Deschamps, R., Braun, K., Jorissen, A., Siess, L., Baes, M., and Camps, P. (2015). Non-conservative evolution in Algols: where is the matter? *A&A*, in press.

di Bartolomeo, A., Barbaro, G., and Perinotto, M. (1995). Internal extinction in spiral disc galaxies. *MNRAS*, 277:1279.

Dobashi, K., Bernard, J.-P., Hughes, A., Paradis, D., Reach, W. T., and Kawamura, A. (2008). Extinction and dust/gas ratio in LMC molecular clouds. *A&A*, 484:205.

Domínguez-Tenreiro, R., Obreja, A., Granato, G. L., Schurer, A., Alpresa, P., Silva, L., Brook, C. B., and Serna, A. (2014). GRASIL-3D: an implementation of dust effects in the SEDs of simulated galaxies. *MNRAS*, 439:3868.

Dominik, C., Blum, J., Cuzzi, J. N., and Wurm, G. (2007). Growth of Dust as the Initial Step Toward Planet Formation. *Protostars and Planets V*, page 783.

Draine, B. T., Dale, D. A., Bendo, G., Gordon, K. D., Smith, J. D. T., Armus, L., Engelbracht, C. W., Helou, G., Kennicutt, Jr., R. C., Li, A., Roussel, H., Walter, F., Calzetti, D., Moustakas, J., Murphy, E. J., Rieke, G. H., Bot, C., Hollenbach, D. J., Sheth, K., and Teplitz, H. I. (2007). Dust Masses, PAH Abundances, and Starlight Intensities in the SINGS Galaxy Sample. *ApJ*, 663:866.

Draine, B. T. and Li, A. (2001). Infrared Emission from Interstellar Dust. I. Stochastic Heating of Small Grains. *ApJ*, 551:807.

Driver, S. P., Popescu, C. C., Tuffs, R. J., Liske, J., Graham, A. W., Allen, P. D., and de Propris, R. (2007). The Millennium Galaxy Catalogue: the B-band attenuation of bulge and disc light and the implied cosmic dust and stellar mass densities. *MNRAS*, 379:1022–1036.

Duffell, P. C. and MacFadyen, A. I. (2011). TESS: A relativistic hydrodynamics code on a moving Voronoi mesh. *ApJS*, 197:15.

Dullemond, C. P. and Monnier, J. D. (2010). The Inner Regions of Protoplanetary Disks. *ARA&A*, 48:205.

Dunne, L., Gomez, H. L., da Cunha, E., Charlot, S., Dye, S., Eales, S., Maddox, S. J., Rowlands, K., Smith, D. J. B., Auld, R., Baes, M., Bonfield, D. G., Bourne, N., Buttiglione, S., Cava, A., Clements, D. L., Coppin, K. E. K., Cooray, A., Dariush, A., de Zotti, G., Driver, S., Fritz, J., Geach, J., Hopwood, R., Ibar, E., Ivison, R. J., Jarvis, M. J., Kelvin, L., Pascale, E., Pohlen, M., Popescu, C., Rigby, E. E., Robotham, A., Rodighiero, G., Sansom, A. E., Serjeant, S., Temi, P., Thompson, M., Tuffs, R., van der Werf, P., and Vlahakis, C. (2011). Herschel-ATLAS: rapid evolution of dust in galaxies over the last 5 billion years. *MNRAS*, 417:1510.

Dwek, E. (1998). The Evolution of the Elemental Abundances in the Gas and Dust Phases of the Galaxy. *ApJ*, 501:643.

Dwek, E., Galliano, F., and Jones, A. P. (2007). The Evolution of Dust in the Early Universe with Applications to the Galaxy SDSS J1148+5251. *ApJ*, 662:927.

Efstathiou, A. and Rowan-Robinson, M. (1995). Dusty discs in active galactic nuclei. *MNRAS*, 273:649.

Emsellem, E., Renaud, F., Bournaud, F., Elmegreen, B., Combes, F., and Gabor, J. M. (2015). The interplay between a galactic bar and a supermassive black hole: nuclear fuelling in a subparsec resolution galaxy simulation. *MNRAS*, 446:2468.

Flannery, B. P., Roberge, W., and Rybicki, G. B. (1980). The penetration of diffuse ultraviolet radiation into interstellar clouds. *ApJ*, 236:598.

Frisken, S. F. and Perry, R. N. (2002). Simple and efficient traversal methods for quadtrees and octrees. *Journal of Graphics Tools*, 7:2002.

Fritz, J., Franceschini, A., and Hatziminaoglou, E. (2006). Revisiting the infrared spectra of active galactic nuclei with a new torus emission model. *MNRAS*, 366:767.

Fritz, J., Gentile, G., Smith, M. W. L., Gear, W. K., Braun, R., Duval, J. R., Bendo, G. J., Baes, M., Eales, S. A., Verstappen, J., Blommaert, J. A. D. L., Boquien, M., Boselli, A., Clements, D., Cooray, A. R., Cortese, L., De Looze, I., Ford, G. P., Galliano, F., Gomez, H. L., Gordon, K. D., Lebouteiller, V., O'Halloran, B., Kirk, J., Madden, S. C., Page, M. J., Remy, A., Roussel, H., Spinoglio, L., Thilker, D., Vaccari, M., Wilson, C. D., and Waelkens, C. (2012). The Herschel Exploitation of Local Galaxy Andromeda (HELGA). I. Global far-infrared and sub-mm morphology. *A&A*, 546:A34.

Fryxell, B., Olson, K., Ricker, P., Timmes, F. X., Zingale, M., Lamb, D. Q., MacNeice, P., Rosner, R., Truran, J. W., and Tufo, H. (2000). FLASH: An Adaptive Mesh Hydrodynamics Code for Modeling Astrophysical Thermonuclear Flashes. *ApJS*, 131:273.

Fuchs, H., Kedem, Z. M., and Naylor, B. (1979). Predetermining visibility priority in 3-d scenes (preliminary report). *SIGGRAPH Comput. Graph.*, 13:175.

Fuchs, H., Kedem, Z. M., and Naylor, B. F. (1980a). On visible surface generation by a priori tree structures. *SIGGRAPH Comput. Graph.*, 14:124–133.

Fuchs, H., Kedem, Z. M., and Naylor, B. F. (1980b). On visible surface generation by a priori tree structures. *SIGGRAPH Comput. Graph.*, 14:124.

Gadotti, D. A., Baes, M., and Falony, S. (2010). Radiative transfer in disc galaxies - IV. The effects of dust attenuation on bulge and disc structural parameters. *MNRAS*, 403:2053.

Garrod, R. T., Weaver, S. L. W., and Herbst, E. (2008). Complex chemistry in star-forming regions: An expanded gas-grain warm-up chemical model. *ApJ*, 682:283.

Gerner, T. (2014). *Chemical characterization of the early evolutionary phases of high-mass star-forming regions*. PhD thesis, University of Heidelberg.

Glassner, A. S. (1984). Space Subdivision for Fast Ray Tracing. *IEEE Comput. Graph. Appl.*, 4:15.

Goosmann, R. W. and Gaskell, C. M. (2007). Modeling optical and UV polarization of AGNs. I. Imprints of individual scattering regions. *A&A*, 465:129.

Governato, F., Brook, C. B., Brooks, A. M., Mayer, L., Willman, B., Jonsson, P., Stilp, A. M., Pope, L., Christensen, C., Wadsley, J., and Quinn, T. (2009). Forming a large disc galaxy from a $z<1$ major merger. *MNRAS*, 398:312.

Granato, G. L. and Danese, L. (1994). Thick Tori around Active Galactic Nuclei - a Comparison of Model Predictions with Observations of the Infrared Continuum and Silicate Features. *MNRAS*, 268:235.

Guedes, J., Callegari, S., Madau, P., and Mayer, L. (2011). Forming Realistic Late-type Spirals in a ΛCDM Universe: The Eris Simulation. *ApJ*, 742:76.

Guhathakurta, P. and Draine, B. T. (1989). Temperature fluctuations in interstellar grains. I - Computational method and sublimation of small grains. *ApJ*, 345:230.

Gustafson, B. A. S. (1994). Physics of Zodiacal Dust. *Annual Review of Earth and Planetary Sciences*, 22:553.

Hao, C.-N., Kennicutt, R. C., Johnson, B. D., Calzetti, D., Dale, D. A., and Moustakas, J. (2011). Dust-corrected Star Formation Rates of Galaxies. II. Combinations of Ultraviolet and Infrared Tracers. *ApJ*, 741:124.

Harries, T. J. (2011). An algorithm for Monte Carlo time-dependent radiation transfer. *MNRAS*, 416:1500.

Harries, T. J., Monnier, J. D., Symington, N. H., and Kurosawa, R. (2004). Three-dimensional dust radiative-transfer models: the Pinwheel Nebula of WR 104. *MNRAS*, 350:565.

Havran, V. (1999). A summary of octree ray traversal algorithms. *Ray Tracing News*, 12:2.

Havran, V. (2000). *Heuristic Ray Shooting Algorithms*. PhD thesis, Czech Technical University.

Hayward, C. C., Jonsson, P., Kereš, D., Magnelli, B., Hernquist, L., and Cox, T. J. (2012). How to distinguish starbursts and quiescently star-forming galaxies: the 'bimodal' submillimetre galaxy population as a case study. *MNRAS*, 424:951.

Hayward, C. C., Kereš, D., Jonsson, P., Narayanan, D., Cox, T. J., and Hernquist, L. (2011). What Does a Submillimeter Galaxy Selection Actually Select? The Dependence of Submillimeter Flux Density on Star Formation Rate and Dust Mass. *ApJ*, 743:159.

Hayward, C. C., Lanz, L., Ashby, M. L. N., Fazio, G., Hernquist, L., Martínez-Galarza, J. R., Noeske, K., Smith, H. A., Wuyts, S., and Zezas, A. (2014). The total infrared luminosity may significantly overestimate the star formation rate of quenching and recently quenched galaxies. *MNRAS*, 445:1598.

Hayward, C. C., Narayanan, D., Kereš, D., Jonsson, P., Hopkins, P. F., Cox, T. J., and Hernquist, L. (2013). Submillimetre galaxies in a hierarchical universe: number counts, redshift distribution and implications for the IMF. *MNRAS*, 428:2529.

Hegmann, M. and Kegel, W. H. (2003). Radiative transfer in clumpy environments: absorption and scattering by dust. *MNRAS*, 342:453.

Hendrix, T., Keppens, R., and Camps, P. (2015). Modelling ripples in Orion with coupled dust dynamics and radiative transfer. *A&A*, 575:A110.

Henyey, L. G. (1937). The Illumination of Reflection Nebulae. *ApJ*, 85:107.

Hernquist, L. (1987). Performance characteristics of tree codes. *ApJS*, 64:715.

Hernquist, L. and Katz, N. (1989). TREESPH - A unification of SPH with the hierarchical tree method. *ApJS*, 70:419.

Heymann, F. and Siebenmorgen, R. (2012). GPU-based Monte Carlo Dust Radiative Transfer Scheme Applied to Active Galactic Nuclei. *ApJ*, 751:27.

Hirashita, H. (2012). Dust growth in the interstellar medium: how do accretion and coagulation interplay? *MNRAS*, 422:1263.

Hockney, R. W. and Eastwood, J. W. (1981). *Computer Simulation Using Particles*. New York: McGraw-Hill.

Hollenbach, D. and Salpeter, E. E. (1971). Surface Recombination of Hydrogen Molecules. *ApJ*, 163:155.

Holwerda, B. W., Bianchi, S., Baes, M., de Jong, R. S., Dalcanton, J. J., Radburn-Smith, D., Gordon, K., and Xilouris, M. (2012). New HErschel Multi-wavelength Extragalactic Survey of Edge-on Spirals (NHEMESES). *IAU Symposium*, 284:128.

Hönig, S. F., Beckert, T., Ohnaka, K., and Weigelt, G. (2006). Radiative transfer modeling of three-dimensional clumpy AGN tori and its application to NGC 1068. *A&A*, 452:459.

Hönig, S. F. and Kishimoto, M. (2010). The dusty heart of nearby active galaxies. II. From clumpy torus models to physical properties of dust around AGN. *A&A*, 523:A27.

Hoppe, P., Leitner, J., Gröner, E., Marhas, K. K., Meyer, B. S., and Amari, S. (2010). NanoSIMS Studies of Small Presolar SiC Grains: New Insights into Supernova Nucleosynthesis, Chemistry, and Dust Formation. *ApJ*, 719:1370.

Hunt, L. K., Pierini, D., and Giovanardi, C. (2004). Near-infrared observations of galaxies in Pisces-Perseus. V. On the origin of bulges. *A&A*, 414:905.

Indebetouw, R., Whitney, B. A., Johnson, K. E., and Wood, K. (2006). Three-dimensional Models of Embedded High-Mass Stars: Effects of a Clumpy Circumstellar Medium. *ApJ*, 636:362.

Inoue, S. and Saitoh, T. R. (2014). Properties of thick discs formed in clumpy galaxies. *MNRAS*, 441:243.

Jackins, C. L. and Tanimoto, S. L. (1980). Oct-trees and their use in representing three-dimensional objects. *Computer Graphics and Image Processing*, 14:249.

James, A., Dunne, L., Eales, S., and Edmunds, M. G. (2002). SCUBA observations of galaxies with metallicity measurements: a new method for determining the relation between submillimetre luminosity and dust mass. *MNRAS*, 335:753.

Jonsson, P. (2006). SUNRISE: polychromatic dust radiative transfer in arbitrary geometries. *MNRAS*, 372:2.

Jonsson, P., Groves, B. A., and Cox, T. J. (2010). High-resolution panchromatic spectral models of galaxies including photoionization and dust. *MNRAS*, 403:17.

Juvela, M. (2005). Efficient Monte Carlo methods for continuum radiative transfer. *A&A*, 440:531.

Kawata, D., Okamoto, T., Gibson, B. K., Barnes, D. J., and Cen, R. (2013). Calibrating an updated smoothed particle hydrodynamics scheme within gcd+. *MNRAS*, 428:1968.

Kennicutt, Jr., R. C., Hao, C.-N., Calzetti, D., Moustakas, J., Dale, D. A., Bendo, G., Engelbracht, C. W., Johnson, B. D., and Lee, J. C. (2009). Dust-corrected Star Formation Rates of Galaxies. I. Combinations of Hα and Infrared Tracers. *ApJ*, 703:1672.

Kramer, C., Buchbender, C., Xilouris, E. M., Boquien, M., Braine, J., Calzetti, D., Lord, S., Mookerjea, B., Quintana-Lacaci, G., Relaño, M., Stacey, G., Tabatabaei, F. S., Verley, S., Aalto, S., Akras, S., Albrecht, M., Anderl, S., Beck, R., Bertoldi, F., Combes, F., Dumke, M., Garcia-Burillo, S., Gonzalez, M., Gratier, P., Güsten, R., Henkel, C., Israel, F. P., Koribalski, B., Lundgren, A., Martin-Pintado, J., Röllig, M., Rosolowsky, E., Schuster, K. F., Sheth, K., Sievers, A., Stutzki, J., Tilanus, R. P. J., van der Tak, F., van der Werf, P., and Wiedner, M. C. (2010). PACS and SPIRE photometer maps of M 33: First results of the HERschel M 33 Extended Survey (HERM33ES). *A&A*, 518:L67.

Kregel, M., van der Kruit, P. C., and de Grijs, R. (2002). Flattening and truncation of stellar discs in edge-on spiral galaxies. *MNRAS*, 334:646.

Küppers, M., Bertini, I., Fornasier, S., Gutierrez, P. J., Hviid, S. F., Jorda, L., Keller, H. U., Knollenberg, J., Koschny, D., Kramm, R., Lara, L.-M., Sierks, H., Thomas, N., Barbieri, C., Lamy, P., Rickman, H., Rodrigo, R., A'Hearn, M. F., Angrilli, F., Bailey, M., Barthol, P., Barucci, M. A., Bertaux, J.-L., Burns, J. A., Cremonese, G., Curdt, W., De Cecco, M., Debei, S., Fulle, M., Gliem, F., Ip, W. H., Huhrt, E., Llebaria, A., Lopez Moreno, J. J., Marzari, F., Naletto, G., Sabau, L., Sanz Andres, A., Sivan, J. P., Tondello, G., and Wenzel, K.-P. (2005). A large dust/ice ratio in the nucleus of comet 9P/Tempel 1. *Nature*, 437:987.

Kurosawa, R. and Hillier, D. J. (2001). Tree-structured grid model of line and polarization variability from massive binaries. *A&A*, 379:336.

Kylafis, N. D. and Bahcall, J. N. (1987). Dust distribution in spiral galaxies. *ApJ*, 317:637.

Lagache, G., Puget, J.-L., and Dole, H. (2005). Dusty Infrared Galaxies: Sources of the Cosmic Infrared Background. *ARA&A*, 43:727.

Laursen, P., Razoumov, A. O., and Sommer-Larsen, J. (2009). Lyα Radiative Transfer in Cosmological Simulations Using Adaptive Mesh Refinement. *ApJ*, 696:853.

Li, Y., Calzetti, D., Kennicutt, R. C., Hong, S., Engelbracht, C. W., Dale, D. A., and Moustakas, J. (2010). Spitzer 70 μm Emission as a Star Formation Rate Indicator for Sub-galactic Regions. *ApJ*, 725:677.

Lucy, L. B. (1999). Computing radiative equilibria with Monte Carlo techniques. *A&A*, 344:282.

Lunttila, T. and Juvela, M. (2012). Radiative transfer on hierarchial grids. *A&A*, 544:A52.

MacDonald, D. J. and Booth, K. S. (1990). Heuristics for ray tracing using space subdivision. *Vis. Comput.*, 6:153.

MacLachlan, J. M., Matthews, L. D., Wood, K., and Gallagher, J. S. (2011). The Stability of Low Surface Brightness Disks Based on Multi-wavelength Modeling. *ApJ*, 741:6.

Marinacci, F., Pakmor, R., and Springel, V. (2014). The formation of disc galaxies in high-resolution moving-mesh cosmological simulations. *MNRAS*, 437:1750.

Matthews, L. D. and Wood, K. (2001). Modeling the Interstellar Medium of Low Surface Brightness Galaxies: Constraining Internal Extinction, Disk Color Gradients, and Intrinsic Rotation Curve Shapes. *ApJ*, 548:150.

Mattila, K. (1970). Interpretation of the surface brightness of dark nebulae. *A&A*, 9:53.

Mattsson, L. and Andersen, A. C. (2012). On the dust abundance gradients in late-type galaxies - II. Analytical models as evidence for massive interstellar dust growth in SINGS galaxies. *MNRAS*, 423:38.

Milkey, R. W., Shine, R. A., and Mihalas, D. (1975). Resonance-line transfer with partial redistribution. VII Angle-dependent redistribution. *ApJ*, 202:250.

Min, M., Dullemond, C. P., Dominik, C., de Koter, A., and Hovenier, J. W. (2009). Radiative transfer in very optically thick circumstellar disks. *A&A*, 497:155.

Misiriotis, A. and Bianchi, S. (2002). The influence of clumping on surface brightness fits of edge-on spiral galaxies. *A&A*, 384:866.

Misiriotis, A., Kylafis, N. D., Papamastorakis, J., and Xilouris, E. M. (2000). Is the exponential distribution a good approximation of dusty galactic disks? *A&A*, 353:117.

Misiriotis, A., Popescu, C. C., Tuffs, R., and Kylafis, N. D. (2001). Modeling the spectral energy distribution of galaxies. II. Disk opacity and star formation in 5 edge-on spirals. *A&A*, 372:775.

Monaghan, J. J. (1992). Smoothed particle hydrodynamics. *ARA&A*, 30:543.

Murante, G., Monaco, P., Borgani, S., Tornatore, L., Dolag, K., and Goz, D. (2015). Simulating realistic disc galaxies with a novel sub-resolution ISM model. *MNRAS*, 447:178.

Natale, G., Popescu, C. C., Tuffs, R. J., Debattista, V. P., Fischera, J., and Grootes, M. W. (2015). Predicting the stellar and non-equilibrium dust emission spectra of high-resolution simulated galaxies with DART-Ray. *A&A*, submitted.

Natale, G., Popescu, C. C., Tuffs, R. J., and Semionov, D. (2014). DART-RAY: a 3D ray-tracing radiative transfer code for calculating the propagation of light in dusty galaxies. *MNRAS*, 438:3137.

Natta, A. and Panagia, N. (1984). Extinction in inhomogeneous clouds. *ApJ*, 287:228.

Nenkova, M., Ivezić, Ž., and Elitzur, M. (2002). Dust Emission from Active Galactic Nuclei. *ApJL*, 570:L9.

Nenkova, M., Sirocky, M. M., Ivezić, Ž., and Elitzur, M. (2008). AGN Dusty Tori. I. Handling of Clumpy Media. *ApJ*, 685:147.

Niccolini, G. and Alcolea, J. (2006). 3D continuum radiative transfer. A new adaptive grid construction algorithm based on the Monte Carlo method. *A&A*, 456:1.

Niccolini, G., Woitke, P., and Lopez, B. (2003). High precision Monte Carlo radiative transfer in dusty media. *A&A*, 399:703.

Paardekooper, J.-P., Kruip, C. J. H., and Icke, V. (2010). SimpleX2: radiative transfer on an unstructured, dynamic grid. *A&A*, 515:A79.

Paradis, D., Dobashi, K., Shimoikura, T., Kawamura, A., Onishi, T., Fukui, Y., and Bernard, J.-P. (2012). Dark gas in the solar neighborhood from extinction data. *A&A*, 543:A103.

Pastrav, B. A., Popescu, C. C., Tuffs, R. J., and Sansom, A. E. (2013a). The effects of dust on the derived photometric parameters of disks and bulges in spiral galaxies. *A&A*, 553:A80.

Pastrav, B. A., Popescu, C. C., Tuffs, R. J., and Sansom, A. E. (2013b). The effects of dust on the photometric parameters of decomposed disks and bulges. *A&A*, 557:A137.

Peeters, E., Spoon, H. W. W., and Tielens, A. G. G. M. (2004). Polycyclic Aromatic Hydrocarbons as a Tracer of Star Formation? *ApJ*, 613:986.

Pier, E. A. and Krolik, J. H. (1992). Infrared spectra of obscuring dust tori around active galactic nuclei. I - Calculational method and basic trends. *ApJ*, 401:99.

Pierini, D., Gordon, K. D., Witt, A. N., and Madsen, G. J. (2004). Dust Attenuation in Late-Type Galaxies. I. Effects on Bulge and Disk Components. *ApJ*, 617:1022.

Pilbratt, G. L., Riedinger, J. R., Passvogel, T., Crone, G., Doyle, D., Gageur, U., Heras, A. M., Jewell, C., Metcalfe, L., Ott, S., and Schmidt, M. (2010). Herschel Space Observatory. An ESA facility for far-infrared and submillimetre astronomy. *A&A*, 518:L1.

Popescu, C. C., Misiriotis, A., Kylafis, N. D., Tuffs, R. J., and Fischera, J. (2000). Modelling the spectral energy distribution of galaxies. I. Radiation fields and grain heating in the edge-on spiral NGC 891. *A&A*, 362:138.

Popescu, C. C., Tuffs, R. J., Dopita, M. A., Fischera, J., Kylafis, N. D., and Madore, B. F. (2011). Modelling the spectral energy distribution of galaxies. V. The dust and PAH emission SEDs of disk galaxies. *A&A*, 527:A109.

Press, W. H., Teukolsky, S. A., Vetterling, W. T., and Flannery, B. P. (1992). *Numerical recipes in FORTRAN. The art of scientific computing*. Cambridge: University Press.

Rahimi, A. and Kawata, D. (2012). Towards a self-consistent numerical model of late-type galaxies: calibrating the effects of sub-grid physics on galactic models. *MNRAS*, 422:2609.

Rémy-Ruyer, A., Madden, S. C., Galliano, F., Galametz, M., Takeuchi, T. T., Asano, R. S., Zhukovska, S., Lebouteiller, V., Cormier, D., Jones, A., Bocchio, M., Baes, M., Bendo, G. J., Boquien, M., Boselli, A., DeLooze, I., Doublier-Pritchard, V., Hughes, T., Karczewski, O. ., and Spinoglio, L. (2014). Gas-to-dust mass ratios in local galaxies over a 2 dex metallicity range. *A&A*, 563:A31.

Renaud, F., Bournaud, F., Emsellem, E., Elmegreen, B., Teyssier, R., Alves, J., Chapon, D., Combes, F., Dekel, A., Gabor, J., Hennebelle, P., and Kraljic, K. (2013). A sub-parsec resolution simulation of the Milky Way: global structure of the interstellar medium and properties of molecular clouds. *MNRAS*, 436:1836.

Reshetov, A., Soupikov, A., and Hurley, J. (2005). Multi-level ray tracing algorithm. *ACM Trans. Graph.*, 24:1176.

Revelles, J., Ureña, C., and Lastra, M. (2000). An efficient parametric algorithm for octree traversal. In *Journal of WSCG*, page 212.

Roberge, W. G. (1983). The spherical harmonics solution for the radiation field in plane-parallel clouds with embedded sources. *ApJ*, 275:292.

Robitaille, T. P. (2011). HYPERION: an open-source parallelized three-dimensional dust continuum radiative transfer code. *A&A*, 536:A79.

Rycroft, C. H. (2009). Voro++: A three-dimensional voronoi cell library in c++. *Chaos: An Interdisciplinary Journal of Nonlinear Science*, 19:4.

Saftly, W., Baes, M., and Camps, P. (2014). Hierarchical octree and k-d tree grids for 3D radiative transfer simulations. *A&A*, 561:A77.

Saftly, W., Baes, M., De Geyter, G., Camps, P., Renaud, F., Guedes, J., and De Looze, I. (2015). Large and small-scale structures and the dust energy balance problem in spiral galaxies. *A&A*, 576:A31.

Saftly, W., Camps, P., Baes, M., Gordon, K. D., Vandewoude, S., Rahimi, A., and Stalevski, M. (2013). Using hierarchical octrees in Monte Carlo radiative transfer simulations. *A&A*, 554:A10.

Samet, H. (1989). Implementing ray tracing with octrees and neighbor finding. *Computers And Graphics*, 13:445.

Samet, H. (1990). *Applications of Spatial Data Structures: Computer Graphics, Image Processing, and GIS*. Addison-Wesley Longman Publishing Co.

Scannapieco, C., Wadepuhl, M., Parry, O. H., Navarro, J. F., Jenkins, A., Springel, V., Teyssier, R., Carlson, E., Couchman, H. M. P., Crain, R. A., Dalla Vecchia, C., Frenk, C. S., Kobayashi, C., Monaco, P., Murante, G., Okamoto, T., Quinn, T., Schaye, J., Stinson, G. S., Theuns, T., Wadsley, J., White, S. D. M., and Woods, R. (2012). The Aquila comparison project: the effects of feedback and numerical methods on simulations of galaxy formation. *MNRAS*, 423:1726.

Schartmann, M., Meisenheimer, K., Camenzind, M., Wolf, S., and Henning, T. (2005). Towards a physical model of dust tori in Active Galactic Nuclei. Radiative transfer calculations for a hydrostatic torus model. *A&A*, 437:861.

Schartmann, M., Meisenheimer, K., Camenzind, M., Wolf, S., Tristram, K. R. W., and Henning, T. (2008). Three-dimensional radiative transfer models of clumpy tori in Seyfert galaxies. *A&A*, 482:67.

Schartmann, M., Wada, K., Prieto, M. A., Burkert, A., and Tristram, K. R. W. (2014). Time-resolved infrared emission from radiation-driven central obscuring structures in active galactic nuclei. *MNRAS*, 445:3878.

Schaye, J., Crain, R. A., Bower, R. G., Furlong, M., Schaller, M., Theuns, T., Dalla Vecchia, C., Frenk, C. S., McCarthy, I. G., Helly, J. C., Jenkins, A., Rosas-Guevara, Y. M., White, S. D. M., Baes, M., Booth, C. M., Camps, P., Navarro, J. F., Qu, Y., Rahmati, A., Sawala, T., Thomas, P. A., and Trayford, J. (2015). The EAGLE project: simulating the evolution and assembly of galaxies and their environments. *MNRAS*, 446:521.

Schechtman-Rook, A. and Bershady, M. A. (2014). Near-infrared Structure of Fast and Slow-rotating Disk Galaxies. *ApJ*, 795:136.

Schechtman-Rook, A., Bershady, M. A., and Wood, K. (2012). The Three-dimensional Distribution of Dust in NGC 891. *ApJ*, 746:70.

Schumacker, R. A., Brand, B., Gilliland, M. G., and Sharp, W. H. (1969). *Study for Applying Computer-generated Images to Visual Simulation*. U.S. Air Force Human Resources Laboratory.

Shevtsov, M., Soupikov, A., and Kapustin, A. (2007). Highly parallel fast kd-tree construction for interactive ray tracing of dynamic scenes. *Comput. Graph. Forum*, 26:395.

Smith, D. J. B., Hardcastle, M. J., Jarvis, M. J., Maddox, S. J., Dunne, L., Bonfield, D. G., Eales, S., Serjeant, S., Thompson, M. A., Baes, M., Clements, D. L., Cooray, A., De Zotti, G., Gonzàlez-Nuevo, J., Werf, P. v. d., Virdee, J., Bourne, N., Dariush, A., Hopwood, R., Ibar, E., and Valiante, E. (2013). Isothermal dust models of Herschel-ATLAS galaxies. *MNRAS*, 436:2435.

Springel, V. (2005). The cosmological simulation code GADGET-2. *MNRAS*, 364:1105.

Springel, V. (2010). E pur si muove: Galilean-invariant cosmological hydrodynamical simulations on a moving mesh. *MNRAS*, 401:791.

Stalevski, M., Fritz, J., Baes, M., Nakos, T., and Popović, L. Č. (2012). 3D radiative transfer modelling of the dusty tori around active galactic nuclei as a clumpy two-phase medium. *MNRAS*, 420:2756.

Stamatellos, D. and Whitworth, A. P. (2005). Monte Carlo radiative transfer in SPH density fields. *A&A*, 439:153.

Steinacker, J., Bacmann, A., and Henning, T. (2002). Application of adaptive multi-frequency grids to three-dimensional astrophysical radiative transfer. *JQSRT*, 75:765.

Steinacker, J., Bacmann, A., and Henning, T. (2006). Ray Tracing for Complex Astrophysical High-opacity Structures. *ApJ*, 645:920.

Steinacker, J., Bacmann, A., Henning, T., Klessen, R., and Stickel, M. (2005). 3D continuum radiative transfer in complex dust configurations. II. 3D structure of the dense molecular cloud core ρ Oph D. *A&A*, 434:167.

Steinacker, J., Baes, M., and Gordon, K. D. (2013). Three-Dimensional Dust Radiative Transfer. *ARA&A*, 51:63.

Stenholm, L. G., Stoerzer, H., and Wehrse, R. (1991). An efficient method for the solution of 3-D radiative transfer problems. *JQSRT*, 45:47.

Stinson, G. S., Brook, C., Macciò, A. V., Wadsley, J., Quinn, T. R., and Couchman, H. M. P. (2013). Making Galaxies In a Cosmological Context: the need for early stellar feedback. *MNRAS*, 428:129.

Sundar, H., Sampath, R. S., and Biros, G. (2008). Bottom-Up Construction and 2:1 Balance Refinement of Linear Octrees in Parallel. *SIAM J. Sci. Comput.*, 30:2675.

Tasitsiomi, A. (2006). Lyα Radiative Transfer in Cosmological Simulations and Application to a $z = 8$ Lyα Emitter. *ApJ*, 645:792.

Teyssier, R. (2002). Cosmological hydrodynamics with adaptive mesh refinement. A new high resolution code called RAMSES. *A&A*, 385:337.

Tuffs, R. J., Popescu, C. C., Völk, H. J., Kylafis, N. D., and Dopita, M. A. (2004). Modelling the spectral energy distribution of galaxies. III. Attenuation of stellar light in spiral galaxies. *A&A*, 419:821.

Városi, F. and Dwek, E. (1999). Analytical Approximations for Calculating the Escape and Absorption of Radiation in Clumpy Dusty Environments. *ApJ*, 523:265.

Verhamme, A., Schaerer, D., and Maselli, A. (2006). 3D Lyα radiation transfer. I. Understanding Lyα line profile morphologies. *A&A*, 460:397.

Verstappen, J., Fritz, J., Baes, M., Smith, M. W. L., Allaert, F., Bianchi, S., Blommaert, J. A. D. L., De Geyter, G., De Looze, I., Gentile, G., Gordon, K. D., Holwerda, B. W., Viaene, S., and Xilouris, E. M. (2013). HERschel Observations of Edge-on Spirals (HEROES). I. Far-infrared morphology and dust mass determination. *A&A*, 556:A54.

Wada, K., Baba, J., and Saitoh, T. R. (2011). Interplay between Stellar Spirals and the Interstellar Medium in Galactic Disks. *ApJ*, 735:1.

Wadsley, J. W., Stadel, J., and Quinn, T. (2004). Gasoline: a flexible, parallel implementation of TreeSPH. *NewA*, 9:137.

Wald, I. and Havran, V. (2006). On building fast kd-Trees for Ray Tracing, and on doing that in O(N log N). In *IEEE Symposium on Interactive Ray Tracing*, page 61.

Wall, M. (1996). *GAlib: A C++ library of genetic algorithm components*. PhD thesis, Mechanical Engineering Department, Massachusetts Institute of Technology.

Whitney, B. A. (2011). Monte Carlo radiative transfer. *Bulletin of the Astronomical Society of India*, 39:101.

Whitney, B. A., Robitaille, T. P., Bjorkman, J. E., Dong, R., Wolff, M. J., Wood, K., and Honor, J. (2013). Three-dimensional Radiation Transfer in Young Stellar Objects. *ApJS*, 207:30.

Witt, A. N. (1977). Multiple scattering in reflection nebulae. I - A Monte Carlo approach. *ApJS*, 35:1.

Witt, A. N. and Gordon, K. D. (1996). Multiple Scattering in Clumpy Media. I. Escape of Stellar Radiation from a Clumpy Scattering Environment. *ApJ*, 463:681.

Witt, A. N. and Gordon, K. D. (2000). Multiple Scattering in Clumpy Media. II. Galactic Environments. *ApJ*, 528:799.

Wolf, S. (2003). MC3D-3D continuum radiative transfer, Version 2. *Computer Physics Communications*, 150:99.

Wolf, S., Fischer, O., and Pfau, W. (1998). Radiative transfer in the clumpy environment of young stellar objects. *A&A*, 340:103.

Wood, K., Mathis, J. S., and Ercolano, B. (2004). A three-dimensional Monte Carlo photoionization code for modelling diffuse ionized gas. *MNRAS*, 348:1337.

Xilouris, E. M., Alton, P. B., Davies, J. I., Kylafis, N. D., Papamastorakis, J., and Trewhella, M. (1998). Optical and NIR modelling of NGC 891. *A&A*, 331:894.

Xilouris, E. M., Byun, Y. I., Kylafis, N. D., Paleologou, E. V., and Papamastorakis, J. (1999). Are spiral galaxies optically thin or thick? *A&A*, 344:868.

Xilouris, E. M., Kylafis, N. D., Papamastorakis, J., Paleologou, E. V., and Haerendel, G. (1997). The distribution of stars and dust in spiral galaxies: the edge-on spiral UGC 2048. *A&A*, 325:135.

Xu, G. (1997). Hydrodynamic and N-body schemes on an unstructured, adaptive mesh with applications to cosmological simulations. *MNRAS*, 288:903.

Ysard, N., Juvela, M., Demyk, K., Guillet, V., Abergel, A., Bernard, J.-P., Malinen, J., Mény, C., Montier, L., Paradis, D., Ristorcelli, I., and Verstraete, L. (2012). Modelling the dust emission from dense interstellar clouds: disentangling the effects of radiative transfer and dust properties. *A&A*, 542:A21.

Yusef-Zadeh, F., Morris, M., and White, R. L. (1984). Bipolar reflection nebulae - Monte Carlo simulations. *ApJ*, 278:186.

Zafar, T. and Watson, D. (2013). The metals-to-dust ratio to very low metallicities using GRB and QSO absorbers; extremely rapid dust formation. *A&A*, 560:A26.

Zhou, K., Hou, Q., Wang, R., and Guo, B. (2008). Real-time kd-tree construction on graphics hardware. *ACM Trans. Graph.*, 27:126.

Zubko, V., Dwek, E., and Arendt, R. G. (2004). Interstellar Dust Models Consistent with Extinction, Emission, and Abundance Constraints. *ApJS*, 152:211.